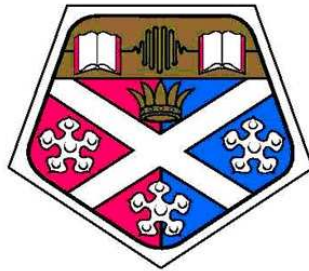


Trace Gas Spectrometry Using Quantum Cascade Lasers

David Wilson

University of Strathclyde
Department of Physics



**UNIVERSITY OF
STRATHCLYDE**

A Thesis in fulfillment of the requirements for
the degree of Doctor of Philosophy
2012

This thesis is the result of the author's original research. It has been composed by the author and has not been previously submitted for examination which has lead to the award of a degree.

©copyright 2012

The copyright of this thesis belongs to the author under the terms of the United Kingdom Copyright Acts, as qualified by University of Strathclyde Regulation 3.49. Due acknowledgment must always be made of the use of any material contained in, or derived from, this thesis.

University of Strathclyde Regulation 3.49:

"Where the author has not lodged with the Librarian a written objection to the copying of their thesis, the Librarian may give permission for single copies of that thesis, in whole or in part, to be made for the purposes of research or private study, or for deposit in the British Library."

Signed:

Date:

ACKNOWLEDGMENTS

Firstly I would like to thank my supervisors Prof. Geoffrey Duxbury and Dr. Nigel Langford who were kind enough to take me on after a rocky start to my postgraduate studies. I would recommend having an emeritus professor as a supervisor to every postgraduate student, the years of experience and knowledge and dedication that came with Prof. Duxbury has been a great resource I had the good fortune of having access to. A great deal of thanks also have to go to Dr. Langford for his enthusiasm and input through my studies. Thanks are also due to my predecessor Kenneth Hay whom I had the luck to overlap the end of his PhD at the start of my time with the group, without this time together I would have struggled a bit with some of the equipment and most importantly I would not have had the opportunity to visit the Glasgow Vintage Vehicle trust and help with experiments on the bus exhausts.

Thanks are due to Dr. Iain Burns of the Chemical and Process Engineering Department at Strathclyde Univ. and his students Jacqueline and Tiger for both opportunities to visit their lab and perform experiments. Also thanks to Dr. Grant Ritchie, Dr. J.P. Van Helden and Richard Walker of the Department of Chemistry at Oxford University for the opportunity to perform experiments that would not have been possible at Strathclyde.

I would like to thank everyone in the electronics workshop (Ged, John and Mark) for their expertise in repairing and checking out some of Geoff's 'older' equipment and Bob and Ewan in the Photonics group workshop for always having time to do the little jobs I needed done.

Most importantly I would like to thank my wife Lorna and kids Fiona and Sophie for support through both my undergraduate and PhD studies, I'm sure it'll all be worth it in the end.

CONTENTS

1. <i>Introduction</i>	7
2. <i>Background Theory</i>	11
2.1 Introduction	11
2.2 Quantum Cascade Lasers (<i>QCL</i>)	12
2.2.1 Inter-Pulse versus Intra-Pulse Tuning	16
2.2.2 Equipment	20
2.3 Absorption Spectroscopy	28
2.3.1 Rapid Passage	44
2.4 Pickett Spectral Simulation Programs	48
3. <i>Field Experiments</i>	51
3.1 Introduction	51
3.2 Bus Exhaust Fumes	53
3.3 Methane Flame Measurements	59
3.4 Ethylene Flame Measurements	66
3.5 Beam Reflection From Non-Mirrored Surface	77
3.6 Conclusion	81
4. <i>Collisional Damping of Rapid Passage Signals</i>	83
4.1 Introduction	83
4.2 Nitric Oxide Pump-Probe Experiment at Oxford University	85
4.2.1 White Cell Collisional Experiments	87
4.2.2 Pump-Probe	96
4.2.3 Repeat of White cell experiments	99
4.3 Collisional Damping Experiments	
Within Strathclyde Laboratory	108
4.3.1 Nitrous Oxide	109
4.3.2 Methane	113
4.3.3 Nitric Oxide, Repeat of Oxford University Experiments	117

4.4	Nitrogen Dioxide and its Dimer	128
4.5	Effect of New Power Supply on Line-Shape When Recording High Resolution $^{14}\text{NH}_3$ and $^{15}\text{NH}_3$ Spectra .	144
4.6	Conclusion	152
5.	<i>Set-up and Testing of a CW QCL For Use In A High Speed Spectrometer</i>	154
5.1	Initial Testing	155
5.2	Laser drive and detector tests	158
5.3	Long Path Tests	171
5.4	Conclusion	177
6.	<i>Conclusions and Future Work</i>	178

ABSTRACT

This project was initially the continuation of a previous PhD students work. This changed slightly to incorporate the initial steps of development of a new system. However the main underlying focus was the absorption of infrared light by molecular gases using a still relatively new light source.

This thesis will present the results of experimental work carried out during studies on the detection of gases and the nonlinear optical effects that arise from the absorption of light from a rapid frequency swept laser. A bench mounted two channel quantum cascade laser absorption spectrometer was used during experiments to observe and reduce nonlinear effects that arise from tuning the lasers during the absorption of light by several atmospherically important gases. These gases include the oxides of nitrogen (nitrous oxide, nitrogen dioxide and nitric oxide), methane and ammonia. The pulsed laser systems used as part of the spectrometer have also been put to use performing measurements on gaseous hydrocarbon combustion (methane and ethylene flames), to determine the feasibility of making measurements within the combustion zone of a jet engine and in conjunction with a continuous wave device during pump-probe experiments at the Chemistry Department of Oxford University. A portable four channel spectrometer was used at the beginning of the project to make measurements of the exhaust fumes of diesel powered vehicles.

It will also cover the initial steps and tests performed in the early stages of development of a continuous wave quantum cascade laser based spectrometer for high speed detection of trace gases.

1. INTRODUCTION

Approximately two thirds of the Sun's radiation is absorbed by the Earth's surface, the remaining third is reflected back into space. The absorbed radiation is re-radiated at infrared wavelengths, rather than the shorter wavelengths emitted by the Sun as it acts as a blackbody. The majority of this radiation escapes into space but enough is absorbed by naturally formed greenhouse gases such as water vapour, carbon dioxide and methane ensuring the stability of the planetary atmospheric systems. Changes in the concentrations of these gases in the atmosphere result in climate change.

Climate change is a process that the planet has undergone since the atmosphere first formed. Until recently in the Earth's history all of these processes have all been driven by natural events. Since the beginning of the industrial revolution average temperatures have been increasing, some believe this is a natural warming of the planet. However this increase has accelerated since the middle of the twentieth century resulting in the reduction in the size of the polar ice caps and the thawing of Arctic permafrost. This increase has been linked to the increased use of fossil fuels and various industrial processes. The burning of fossil fuels has greatly contributed to the concentrations of natural greenhouse gases as well as increasing levels of oxides of nitrogen (NO, NO₂ and N₂O) [1]. A consequence of the warming is the release of methane trapped in the land permafrost and in the ocean, in the form of methane clathrate [2] [3]. Methane is a powerful greenhouse gas resulting in a positive feedback i.e. the more Methane released contributes to warming thus furthering the melting and release of trapped Methane. It is therefore important to monitor the concentrations of these gases in the atmosphere and their interactions with other gases found in the atmosphere. Many of these pollutants have a long lifetime in the atmosphere before they are broken down through chemical reaction. The estimated lifetime (i.e. the time taken to decay to $\frac{1}{e}$ of the quantity added) of Nitrous Oxide is estimated at 114 years. Carbon Dioxide has an estimated lifetime of ≈ 100 years, while Methane has the shortest lifetime of 12 years [1]

Several methods are currently employed to accurately measure these gases in the atmosphere from ground bases to balloon, aircraft and satellite observations. These observations are pivotal in the theoretical modeling of the atmosphere and introduction of legislation intended to reduce emissions from motor vehicles and industry. This led to the development of devices that are capable of long-term unattended operation, such as the tunable diode laser absorption spectrometer (TDLAS) amongst others. Until recently the lasers of choice have been semi-conductor diodes operating in the near infrared region (roughly 800 nm to 3 μm). However most species of molecular gases have fundamental absorption transitions in the mid-infrared region (3 μm to 15 μm). With the development of the Quantum Cascade Laser (QCL) in the 1990's [4] we now have high sensitivity devices operating at room temperature in the mid-infrared region. More recent developments have improved the stability of these devices to the point that they are capable of continuous wave (CW) operation.

The group at Strathclyde University has played an important role in the research of Quantum Cascade Laser (QCL) based absorption spectrometers. This has ranged from a laboratory based spectrometer to the development of a portable spectrometer, utilizing the intra-pulse method to drive the laser, for atmospheric measurements [5]. The developments made by the group has led to a 'spin out' company, Cascade Technologies, manufacturing compact multi channel QCL based spectrometers.

These spectrometers have demonstrated potential for the measurement of concentrations of atmospheric Methane and Nitrous Oxide [5] [6]. Newer devices, such as those manufactured by Cascade Technologies, are now capable of measuring multiple species simultaneously. Previously the standard for these measurements was the Fourier Transform Spectroscopy (FTS). While FTS can achieve high resolution ($\approx 0.001\text{ cm}^{-1}$ as advertised for the Brooker IFS 125 HR) the equipment is bulky and the time involved in performing in scanning/recording an individual spectrum can be lengthy. With QCL spectrometers approaching similar resolutions they have the advantages of compact size and faster refresh rates (for example a QCL based spectrometer can typically record and average 8000 scans per second) over FTS.

This project was based on the use of QCLs as a light source to perform mid-infrared absorption spectroscopy. With the main focus being the reduction of the non-linear effects that arise from the rapid frequency sweep of the laser. This changed to include the use of QCLs in the detection of combustion products within a gas mixture flame, the detection of the dimerization of Nitrogen Dioxide in the 8 μm region and the initial stages of a Continuous Wave (CW) QCL based spectrometer. Although QCL based absorption spectrometers can record real-time data on gas concentration the pressure in the gas cell must be at a level that any non-linear effects due to the laser are minimized. Currently the average cell pressure used to pressure broaden the sample is around 100 Torr. If this can be reduced then the dwell time of gas in the cell can also be reduced, in effect increasing the detection speed of the spectrometer. It was during these experiments that it was noticed that a 'strange' effect was visible in the 8 μm region when Nitrogen Dioxide was introduced into the cell. A CW-QCL was acquired through Cascade Technologies with the remit of the development of a CW based spectrometer. The CW-QCL supplied was a current modulated Distributed Feedback (DFB) device whereas most other CW-QCLs are tuned by an external Piezo electrically (PZT) controlled grating (i.e. the Daylight Solutions CW-MHF series). Its other main difference between the devices was the wavelength, the Daylight Solutions device operates in the 5 μm region whereas the supplied device operated in the 8 μm region. The aim was to measure Methane and Nitrous Oxide in the atmosphere.

When used in the laboratory setting QCL based spectrometers offer a viable alternative to other methods for gas analysis. For example gas chromatography is a commonly used method for the identification of different species within a gas mixture. However it requires the sample to pass through a specially coated column. The coating causes target gases to exit the column at different times permitting their identification. Mass spectrometry is another method for identification of gases and is often used in conjunction with gas chromatography. This method requires a high vacuum as it entails the gas sample to be ionized often with a high energy electron beam. Although these methods give accurate concentration and identification of gases a QCL based spectrometer can give similar results. A QCL operated in pulsed mode has the advantages of measuring several species in a single scan (often a single scan covers 3.5 cm^{-1}), the beams from the laser are eye-safe due to an extremely small duty cycle (maximum 3%) and the low power nature of the device.

There is a down side to the rapid scan rate of the QCL, i.e. the rapid passage signals. Again to remove these signals it requires the pressure in the cell to be increased. However in the laboratory setting it is possible to use different collision partners and have a greater control of the pressure within the cell (often the gas sample is held within the cell and not a flow through the cell). Partial pressure and thus concentrations can then be determined when the line-shape approaches a Gaussian profile.

Other methods used for spectral analysis include Cavity Ring-Down Spectroscopy (CRDS) where a pulse of light is injected into resonant cavity. The intensity of the light radiation decays through losses at the mirrors. A gas mixture is introduced into the cavity causing an increase of the decay rate. The comparison of decay rates allows concentrations of target gas to be determined. This method has been used in the laboratory environment to record detailed spectra of Methane [7], in the field to measure NO_x in diesel exhaust gases [8] and CO_2 in diesel exhaust gases [9]. QCLs have also become a mid-infrared light source of choice for CRDS with the medical application of detecting Ammonia in breath [10].

CW lasers by their nature have a longer operating time with a lesser wavenumber spread in the laser linewidth. This can give a higher resolutions at the cost of slower scan times. When a lock-in amplifier is used instead of direct absorption then weaker signals can be detected. As a new addition to the QCL device list CW versions have also been used a light source in CRDS to make measurements of Methyl Bromide in the 8 μm region [11]. A portable spectrometer based on a CW-QCL would improve the current methods for the detection of explosives [12] by increasing the detectivity of the decomposition products.

2. BACKGROUND THEORY

2.1 *Introduction*

This section covers, for the first part, the equipment and computer programs used for experimental work and data processing covered in this thesis. The second part covers the theory behind the absorption spectroscopy and the non-linear features observed.

Section 2.2 covers the lasers used in the spectrometers and how they differ from other infrared sources, the detectors used and a brief description of the control software. It continues with the advantages and disadvantages of the different methods for driving the lasers.

Section 2.3 is concerned with absorption spectroscopy starting with linear absorption then goes on to introduce the non-linear behavior due to low pressure and fast frequency sweep (chirp).

Section 2.4 introduces the programs written by Herb Pickett to perform simulations of molecular spectra.

2.2 Quantum Cascade Lasers (QCL)

With the original concept of negative resistance, an increasing current resulting in a decreasing voltage, in superlattices (repeating layers of two or more materials) postulated by Esaki and Tsu in 1970 [13] Kazarinov and Suris [14] proposed the quantum cascade principle in 1971 where they predicted transitions between excited and ground states near quantum wells in superlattices could be accompanied by photon emission. Development of the devices was finally realised by Faist *et al.* [15] working at the Bell Laboratories USA in the early to mid 90's.

Unlike conventional laser diodes that use interband transitions QCLs rely on intersubband transitions to generate each photon. Interband transitions in diode lasers involve a current applied to cause electrons to populate the conduction band of the semiconductor, relaxation of the system has these electrons in the conduction band recombining with electron 'holes' in the valence band with the emission of a photon, see figure 2.1(a), the frequency of which depends on the band gap of the material. In intersubband transitions an applied current injects electrons into the conduction band, these electrons then relax from a higher energy level to a lower energy level in the same conduction band, see figure 2.1(b), emitting a photon with frequency dependent on the difference between the two levels (E_3-E_2 , this terminology is used as in the quantum wells of a QCL there is three energy levels). As the transitions are within the same band the levels involved in the optical transition are parallel and can be graphically described as parabolas [16], this means all intersubband transitions have the same wavelength unlike in a conventional diode laser where transitions away from band centre can have a different wavelength.

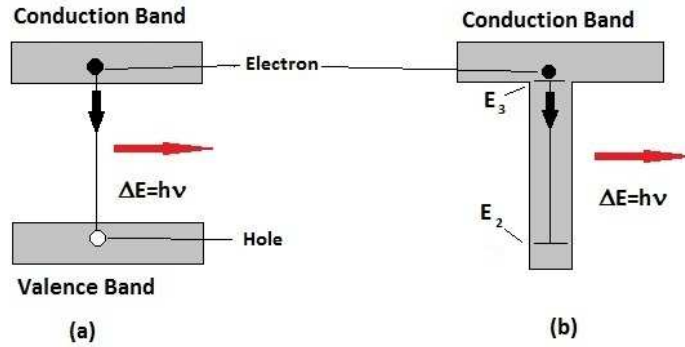


Fig. 2.1: Schematic of the (a) interband transition: photon emission due to electron-hole recombination in laser diodes and (b) intersubband transition: photon emission due to relaxation between energy levels in the quantum well.

Successive layers of quantum wells are deposited using molecular beam epitaxy [17], these form the active region where optical gain occurs. Between these are the layers of digitally graded alloy (usually a layer of $\text{Al}_x\text{Ga}_{1-x}\text{As}$) where electrons are injected into the medium. A schematic of the device operation is shown in figure 2.2. Electrons are injected into the uppermost layer, they relax from the upper energy level (E_3) down to lower energy level (E_2) within the well emitting a photon. They then relax down to energy level (E_1) without photon emission, the energy difference between levels 1 and 2 is related to the phonon energy of the material. Electrons then tunnel through the next injection region into another active region where the relaxation process within a quantum well repeats hence the use of the cascade term in their description.

The first of these devices grown by Faist *et al* [15] was based on $\text{Al}_{0.38}\text{In}_{0.52}\text{As}/\text{Ga}_{0.47}\text{In}_{0.53}\text{As}$ heterojunction material system matched to InP, i.e. the main structure of the device is $\text{Al}_{0.38}\text{In}_{0.52}\text{As}$ with the quantum wells being $\text{Ga}_{0.47}\text{In}_{0.53}\text{As}$.

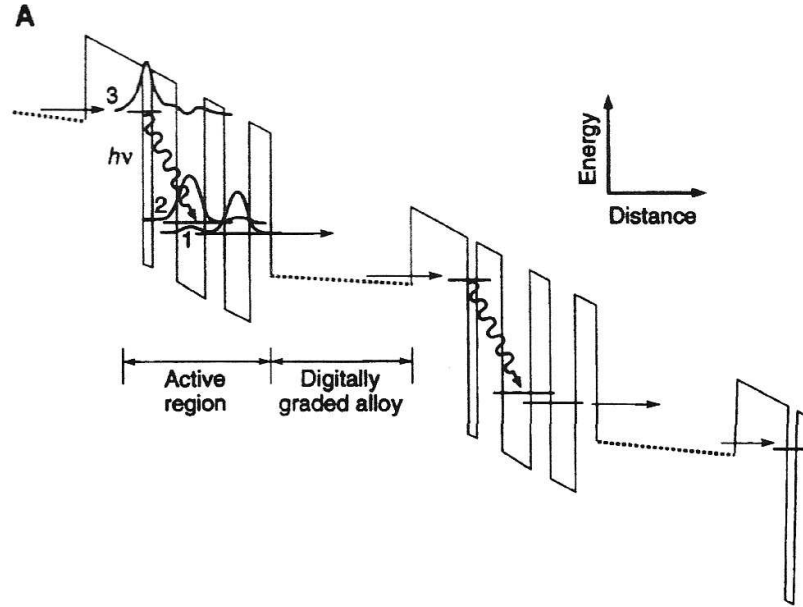


Fig. 2.2: Operational schematic of the quantum well structure within a quantum cascade laser (image taken from [15]).

The device was composed of 25 layers of undoped quantum well active regions alternating with layers of the digitally graded alloy (AlInAs/GaInAs) superlattice. The energy difference between levels E_3 and E_2 was calculated to be 295 meV, which equates to an operational wavelength of $4.26\mu\text{m}$, the energy difference between E_2 and E_1 was 30 meV. Operating in pulsed mode the device still required cryogenic temperatures to function with peak power in excess of 8 mW when cooled to 10 K, the maximum temperature the device operated at was 90 K.

Since this first device many improvements have been made in their construction from increasing the operational temperature such that they can operate at room temperature or at least with a Peltier cooling device to operating in continuous wave mode also at room temperature and higher. Peltier devices are named after Jean-Charles Peltier whom discovered the effect accidentally in 1834 when applying a current through a junction of two different metals. Recent developments by Fujita *et al.* working at the Hamamatsu research laboratory in Japan has realised a device with electro-

luminescence in the order of 600 cm^{-1} , nominal operational wavelength when coated (i.e. when the diffraction grating is incorporated onto the device) of $6.8 \text{ }\mu\text{m}$, with power $> 500 \text{ mW}$ at room temperature and continuous wave operation at 100°C [18]. High power devices are also being developed by Pranalytica Inc. in the USA that operate at $4 \text{ }\mu\text{m}$ and $4.6 \text{ }\mu\text{m}$ with output power in the order of 2 W [19], the most outstanding detail about these devices is that they are not actively cooled relying only on a heat sink and still giving power levels in excess of 1.2 W at 340 K .

This ability to operate at high temperature make them an ideal replacement for lead salt semi-conductor lasers that require liquid nitrogen cooling and with the development of high power devices they are becoming a good candidate to replace CO/CO₂ lasers which are bulky and rely on high current power supplies.

The wavelength of QC lasers is controlled using the distributed feedback method, this entails a distributed Bragg reflector/diffraction grating being grown onto the waveguide. The Bragg reflector prevents the device from emitting other than the desired wavelength. Heating and cooling of the device causes this grating to expand or contract changing the wavelength emitted. As the dimensions of the diffraction grating changes it permits specific wavelengths to pass through and all others to be reflected back into the device. When fast heating is caused by Joule heating as a result of a long current pulse applied to the device the change in wavelength can very quick. This fast heating as well as slow external heating by Peltier control are used to tune the laser frequency. Different methods of controlling the laser frequency will be discussed in section 2.2.1.

2.2.1 Inter-Pulse versus Intra-Pulse Tuning

Tuning of a QC laser operating in pulsed mode is primarily done by heating of the device in order to change the spacing of the Bragg reflector/diffraction grating. The commonly used method for tuning is the Inter-Pulse method, this involves short current pulses with a superimposed sub-threshold ramp. This method was pioneered by Namjou *et al.* and reported in their 1998 paper [20], where they utilized a 1 MHz train of 2.6 A amplitude current pulses each with a duration of 11 ns. A sub-threshold current ramp at a frequency of 4Hz was superimposed onto this pulse train, this ensured that each pulse was a slightly different wavelength from the previous one ($\approx 1\text{cm}^{-1}$).

A variation of this method was described by Namjou and used by Kosterev *et al.* [21], where they used a thermoelectric cooler to vary the laser temperature instead of the sub-threshold current ramp used by Namjou. In combination with short current pulses (5 ns Full Wave Half maximum(FWHM)) the slow continuous temperature change from -25°C to $+5^\circ\text{C}$ gave a spectral tuning of 2.5 cm^{-1} , however the slow scan through the temperature range meant that it took 510 pulses spread over 25.5 ms to record each spectrum. This slow scan was susceptible to low frequency noise from acoustic vibrations emanating from the optical table with magnitude corresponding to 1% of total absorption. To remove this a modification to the wavelength modulation technique was required, voltage step function was used such that each short pulse was matched to a step and the temperature sweep covered three successive voltage steps.

Although the Inter-Pulse methods give narrow laser line widths the short pulses, like that used by Kosterev *et al.*, result in a spectral window in the order of 0.22 cm^{-1} . Successive scans then need to be added in order to cover the 2.5 cm^{-1} , this has the disadvantage of introducing shot-to-shot noise between laser pulses which affects subsequent points in a recorded spectra. Also the laser is typically operated at currents just above threshold in order to minimize asymmetrical line broadening due to thermal chirp.

Another method of tuning the lasers is the Intra-Pulse method developed by Normand *et al.* [22] that uses a current pulse far greater than used in the variations of the Inter-Pulse method, initially the pulse length used was a maximum of 200 ns this has been increased recently to 2000 ns. When using a longer current pulse the sub-threshold ramp is not required as Joule heating occurs due to the extended duration of the current pulse. This type of heating causes a rapid temperature change in the device during its lasing, correspondingly there is a rapid change in frequency emitted by the device. The frequency of emitted light changes from high to low as a function of time as the device heats, This frequency down-chirp results in a spectral window ranging from 0.5 cm^{-1} to 3 cm^{-1} depending on the length of pulse applied and the properties of the device.

The large spectral window obtained by tuning with the Inter-Pulse method allows detection of several molecular species with a single laser. However as with the Intra-Pulse method there is distortion and poor resolution of any spectral feature close to the turn-on and turn-off of the laser pulse. Even though there are distorted signals at the transients the size of the spectral window ensures there is sufficient bandwidth to record all spectral features of interest with a single laser pulse. By changing the substrate temperature, from -30°C to $+45^{\circ}\text{C}$ with the control software currently in use, it is possible to obtain a spectral window covering up to 10 cm^{-1} by adding single shots during post analysis. Both methods for tuning the laser require averaging of spectra to reduce noise.

As well as the large spectral window this method also has the advantages of being high speed and high resolution. Pulse repetition rates up to 20kHz are regularly used and by averaging up to 10,000 single spectra very high quality averaged spectra can be recorded. The typical repetition rate used by the group is 10kHz with averaging of 8000 spectra giving an averaged spectra recorded every second. By varying the repetition rate and the number of spectra averaged it is possible to increase the rate at which spectra are recorded, however there is a trade off between high-speed acquisition and high signal-to-noise ratio that goes with the reduced number of averaged spectra.

The resolution of spectrometers utilizing the intra-pulse method is similar to those using the inter-pulse method. The main difference between the two is with the inter-pulse method the resolution limit is set by the transform limit (time-bandwidth product) of the pulse, Kosterev *et al.* [21] found that $\approx 75\%$ of the laser energy lies within the transform limited part of the spectrum of the pulsed output and by analysing their spectral line-shapes a resolution of Full Wave at Half Maximum (FWHM) of 0.0095 cm^{-1} could be achieved. Whereas with the intra-pulse method the resolution of the detector system is set by the time-bandwidth product of the detected signal [23] and the chirp-rate of the laser giving rise to a variable resolution across the pulse.

For both tuning methods the time-bandwidth product has been shown by Bracewell [24] to have minimum values of

$$\Delta t \Delta \nu \geq C = 0.441 \quad (2.1)$$

for a Gaussian window and

$$\Delta t \Delta \nu \geq C = 0.886 \quad (2.2)$$

for a rectangular window, where Δt is time and $\Delta \nu$ is the bandwidth. In these equations the constant C is derived from the uncertainty relation which cannot have a value of less than $C=(4\pi)^{-1}$. Work done by McCulloch *et al.* [23] has shown the resolution related to the chirp-rate is given by,

$$\Delta \nu = \sqrt{C \frac{d\nu}{dt}} \quad (2.3)$$

with $\frac{d\nu}{dt}$ being the chirp-rate. Using equation 2.3 with typical values of chirp-rates at the start and end of the pulse gives resolution ranging from 0.012 cm^{-1} for a chirp-rate of 150 MHz/ns typical for the start of the pulse, to 0.0044 cm^{-1} for a chirp-rate of 20 MHz/ns at the end of the pulse, similar to many Fourier Transform Spectrometers. These values are based on calculated chirp-rates from spectra recorded within the lab at Strathclyde University where a rectangular current pulse is used to power the lasers.

As a point of interest Grouiez *et al.* [25] used a variation of both methods in their 2009 paper. Here they used pulses longer than those typically used in the inter-pulse method but shorter than those used in the intra-pulse method, pulses ranging from 30 ns to 80 ns but typically 70 ns, as well as thermoelectrically heating the device. This helped reduce the broadening due to thermal chirp, the slightly longer pulse also reduces the shot-to-shot noise but this method has the disadvantages of being slow as a result of tuning by applying external heating and has only a spectral window of 0.5 cm^{-1} . The reason they used pulses of 70 ns as a 'mid' range pulse length was that at the time it was the common belief that a current pulse greater than 300 ns would damage the device. However Duxbury *et.al.* had shown that the devices were capable of pulses lasting 1500 ns, see for example references [26] [27] [28].

It is the Intra-Pulse method that is used to tune the lasers used for this thesis with pulse durations ranging from 100ns to 2000ns, with a typical pulse length of 1500ns.

2.2.2 Equipment

The laser system used for the majority of the experiments in this thesis were supplied through spin-out company Cascade Technologies, the main laser system being a LS-03-D system. This consists of a drive box that controls laser substrate temperature, voltage applied, pulse repetition rate and pulse length through a computer software based interface. Built into the software is safe guard to ensure the duty cycle of the laser does not exceed 3%, as part of the safe guards there is a fixed temperature range of -30°C to $+45^{\circ}\text{C}$, a maximum repetition rate of 20KHz and a maximum pulse length of $2\ \mu\text{s}$. The voltage has to be set according to the manufacturers specifications taking care not to exceed the maximum safe value given in the data-sheet for each device. Connected to the control box is the developer head where the laser is mounted. Figure 2.3 shows the laser mount within the developer head.

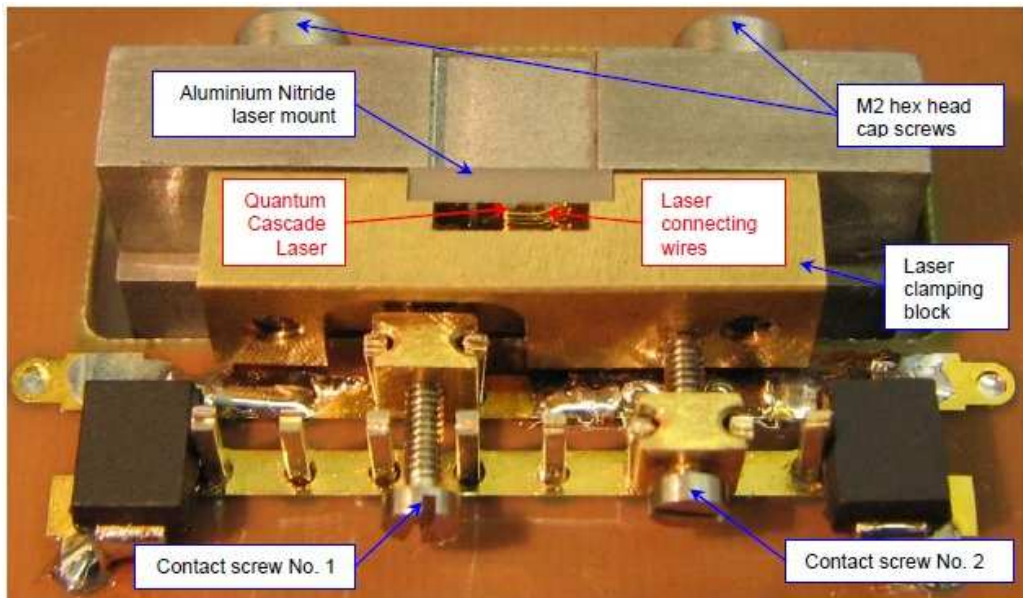


Fig. 2.3: Laser mount inside LS-03-D developer head with device in-situ, the aluminium base is directly connected to a Peltier thermoelectric device. Image reproduced from LS-03-D instruction manual and reproduced with permission of Cascade Technologies.

The modular nature of the LS-03-D system means that different laser devices can be swapped into the head depending on the wavenumber range required when working with specific molecular species. This requires the head to be evacuated and filled with dry nitrogen as any water vapor would form ice and potentially damage the laser. Different heads with different devices installed can be swapped about for use with the drive box, allowing increased versatility. Each developer head has a zinc selenide lens fitted into an adjustable mount allowing the laser beam to be collimated after being replaced and prior to use.

A total of eleven QC laser devices was available for use during this project, four of which still require characterization and have not been used, see table 2.1. The other seven were characterized by previous PhD student Kenneth Hay, details of this work features in his thesis [29]. Five of the seven in use were obtained through the Advanced Components Cooperation for Optoelectronics Research & Development program (ACCORD) and supplied through Cascade Technologies, the other two were bought by the group for specific experiments

Laser ID/ group name	Central Wavelength(μm)	Central Wavenumber	Maximum Voltage
CT-100060/laser 60	4.86	2057	12.5
CT-100061/laser 61	6.15	1626	9
CT-100062/laser 62	6.15	1626	8.5
CT-100063/laser 63	7.24	1382	13.5
CT-100064/laser 64	7.46	1340	13
CT-200051/laser 51	7.84	1275	16
sb1435 DN/ 5micron	5.25	1904	10
CT-100128 ^a	6.13	1630	8.5
CT-100133 ^a	10	993	13
CT-100145 ^a	4.48	2232	11.5
CT-100152 ^a	5.25	1904	11

Tab. 2.1: List of QC lasers owned by the group, ^a Lasers not yet characterized and not used

Within the Strathclyde lab a static spectrometer is mounted onto an optical table, this consists of two Cascade Technologies LS-03-D systems, a multi-pass cell based on the design described by Herriott and Schulte [30] and a mercury-cadmium-tellurium (MCT) thermoelectrically cooled detector.

A schematic of the layout is shown in figure 2.4.

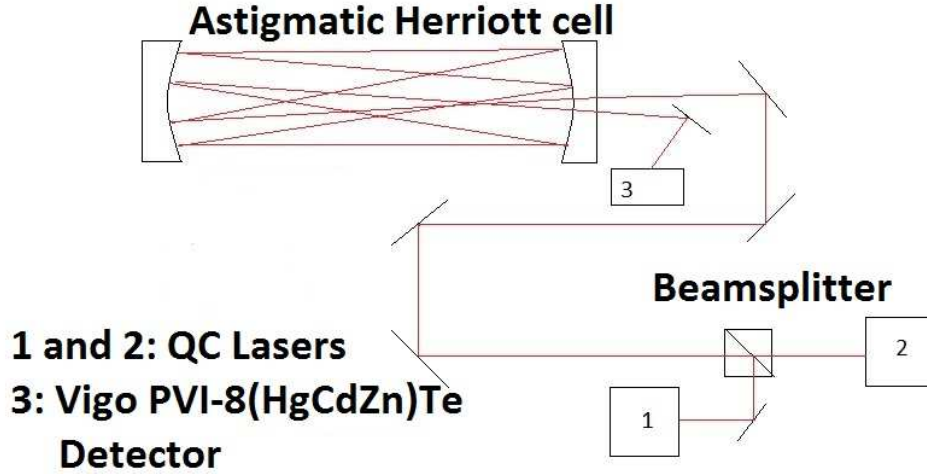


Fig. 2.4: Schematic of the optical bench mounted spectrometer in the Strathclyde lab.

The cell, shown in figure 2.5, is a variation of the long path length multi-pass cell described in [30] fitted with astigmatic mirrors, the spot pattern on the rear mirror differs from those described by Herriott and Schulte giving 232 passes and a path length of 102m. The spot pattern calculations and construction of the cell was performed by a previous student of the group, Michael McCulloch, and features in his PhD thesis [31].

To confirm the path length of the cell is simply a process of comparing the time difference between the current pulse being applied to the laser and that of the detector signal, the LS-03-D system drive box had a port that allows monitoring of the current pulse and when this and the detector signal is displayed on the same oscilloscope the delay can be determined. The path-length of the Herriott cell when used during the lab based experiments in this thesis was calculated to be 62m.

Various connections on the QVF branded borosilicate glass tubing allow for attachment of the vacuum system, an Edwards EXT70 turbo-molecular pump backed with an Edwards E2M8 rotary pump, mounts for three capacitance manometers (MKS Baratrons, 0.01→1 Torr, 0.1→10 Torr, 1→100 Torr) and gas inlets on each end plate. The laser beam enters and exits the same opening of the Herriott cell, fitted with a wedged salt window (CaF),

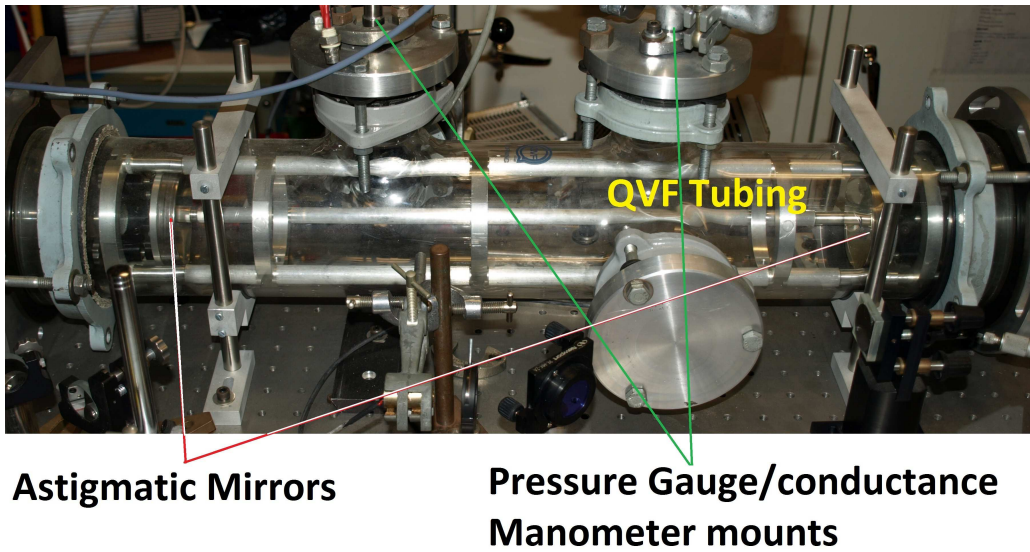


Fig. 2.5: Astigmatic Herriott cell in-situ at Strathclyde lab.

and passes through a central opening in the front mirror. It is this beam path that differs from the long path cell designed by White [32] where the beam enters one opening and exits through a second, in the original configuration described by White the beam traveled in the same plane however modifications to this design where the beam crosses between two, or more, parallel planes within the mirror cavity and then exit on the same plane it entered the cell have resulted in an increased path length. It is this configuration of White cell used by the Ritchie group at the Department of Chemistry, Oxford University for the nitric oxide collisional experiments described later in this thesis.

As the intra-pulse method for tuning the lasers causes a rapid frequency down-chirp a fast, high-bandwidth detector is required in order to resolve absorption lines. For this a thermoelectrically cooled (HgCdZn)Te, MCT, device manufactured by Vigo, model number PVI-2TE8, is used. This is a photovoltaic device grown and doped such that it has a variable band-gap [33], the detector element is mounted on a Peltier cooler and immersed to a high refractive index GaAs hyperhemispherical lens, which give a large acceptance angle of 36° . This replaced the Kolmar KV104 detector, this is also a photovoltaic MCT detector however it requires LN_2 cooling and

does not have the immersion lens present in the Vigo. The Vigo detectors are therefore easier to align and can operate for extended periods without human involvement in their operation.

Having a fast detector means a digitizer with a similar speed to the detector is needed to transfer data to a control computer. The analogue-to-digital card used for this is an ACQiris AP200 high-speed signal averaging PCI (Peripheral Component Interconnect) card mounted into a Amplicon Ventrix PC, the DAQ (Data Acquisition) card is a full length card and does not fit into a standard PC. With a temporal resolution of 0.5 ns (2Gs/s) and a bandwidth of 500MHz the AP200 DAQ card allows the averaging of 65,536 individual spectra with its on board processor, but this is restricted to a maximum of 10,000 to increase the rate at which data is recorded. Averaging and recording of data is controlled via a LabView 7.1 virtual instrument (VI), figure 2.6, based on software supplied by ACQiris the VI has been modified by previous group members. The current version permits the user to set the number of spectra to be averaged, the number of data points to record and the ability to record both averaged detector signal and a normalized transmission signal.

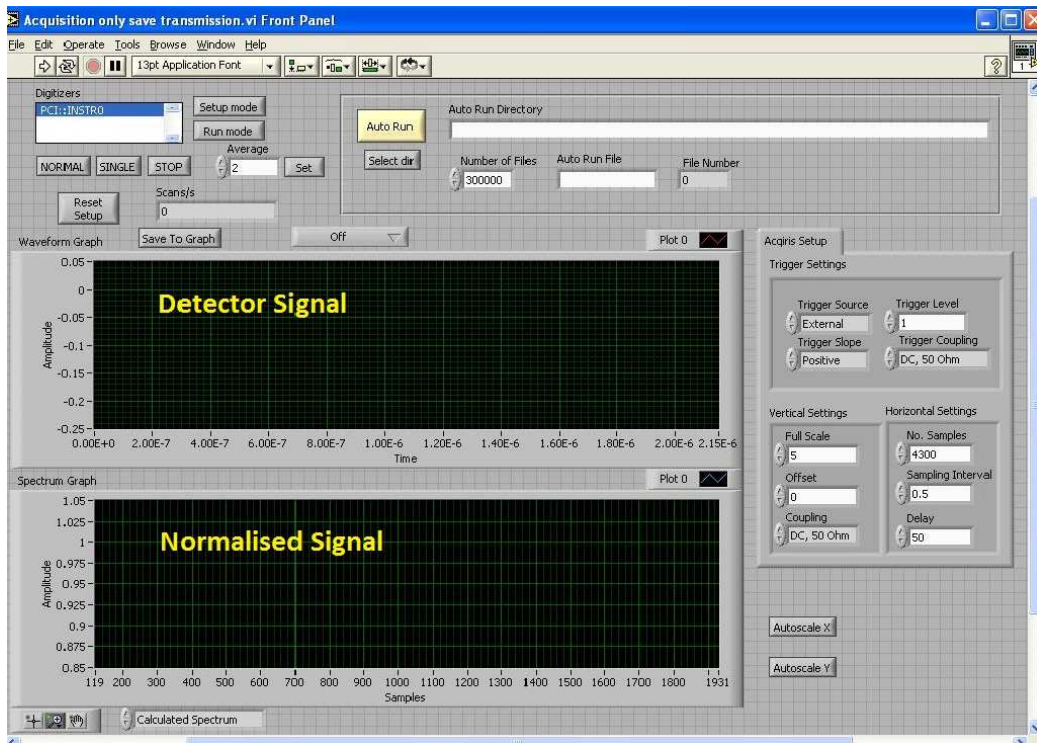


Fig. 2.6: Acquisition only VI. Top window displays the averaged detector signal, bottom window displays normalized transmission

Originally the bench mounted spectrometer only used a single laser. This was changed to include a second enabling the detection of different molecular species or the same molecule in different regions at the same time. In order to perform this the trigger signal from the drive box of one laser is passed through a Stanford Research Inc. DG535 to delay the signal, this delayed signal is then used to trigger the second laser pulse.

The modular nature of the LS-03-D system means it can be easily transported to and used in various locations, it has been used in laboratories [34] and engineering works [35] to perform direct measurements. However it requires lengthy set-up and several power supplies. If direct measurement is not required or is impractical then the portable Four Channel Pulsed Quantum Cascade Laser Absorption Spectrometer (4C-PQCLAS) is used. This is a CT-2400 supplied by Cascade Technologies and uses four QC laser each operating at different wavelengths. Each laser is chosen to detect a specific

gas and software on a control laptop gives on-the-fly concentration measurements of N_2O , NO , NO_2 and CO_2 . Other species are also detected by the spectrometer but require post analysis of data. This device only features for the bus exhaust measurements in this thesis, a more detailed description of the device and its use has previously featured in a thesis [29] and is only mentioned here for completeness.

The cell used in the Strathclyde University lab and in the CT-2400 4C-PQCLAS is an astigmatic Herriott cell. This only varies from the original design [30] in that the mirrors used are slightly elliptical. Both designs have the beam passing through a hole in the front mirror, undergoing several passes between the mirrors and exiting through the same hole, see figure 2.7. The use of the astigmatic mirrors allows a greater total optical path length over the original design.

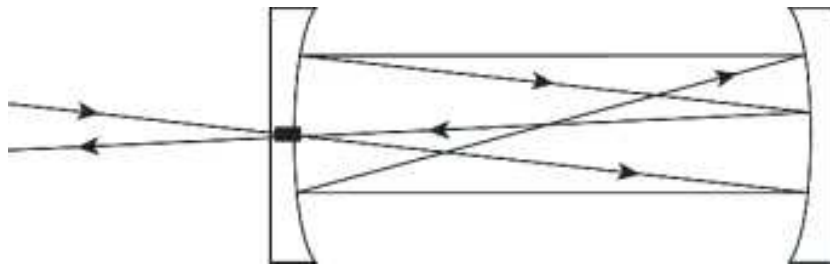


Fig. 2.7: Schematic of beam path in a Herriott cell, (Image taken from <http://cluin.org/programs/21m2/openpath/tdl/>)

The group at Oxford University use both single pass and a modified White cell. The original White cell [32] has the light beam entering one side of the front mirror, reflects between the rear mirror and the front mirror (the path of the beam remains in the same plane) and finally exits the other side of the front mirror, see figure 2.8.

Modifications to this design are used to increase the optical path length. These modifications include the front mirror having indents to allow the beam to enter and exit the cell. The rear mirror is split to form two curved reflective surfaces. Both of these modifications permit the beam to occupy two planes with sufficient separation so that a standing wave does not occur. This modified cell was first described in the 1948 paper by Bernstein and Herzberg [36] and is known as a Herzberg-Bernstein Cell, see figure 2.9.

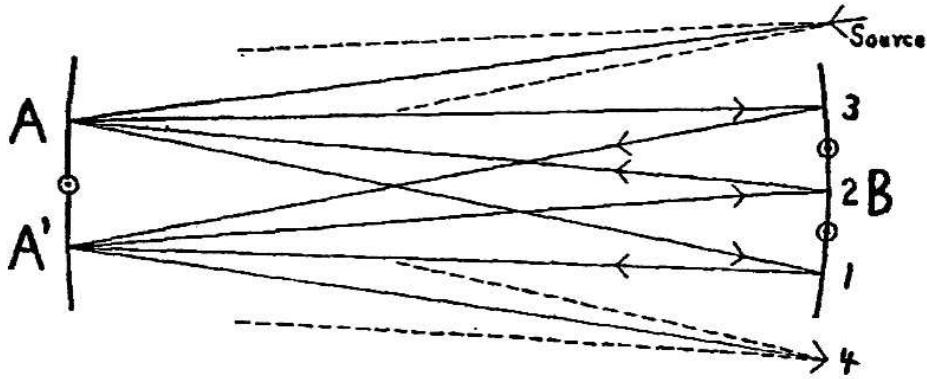


Fig. 2.8: Schematic of beam path in a White cell, (image taken from [32])

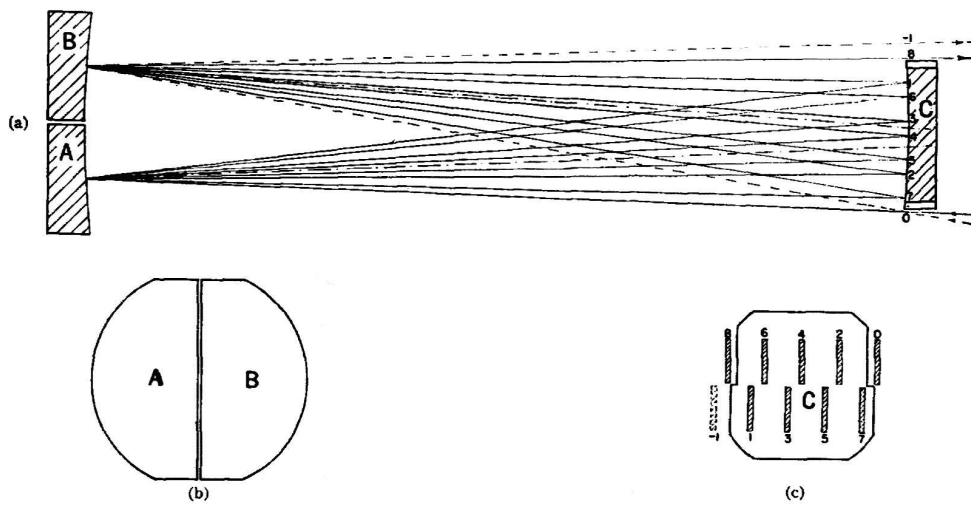


Fig. 2.9: Schematic of Herzberg-Bernstein Cell, modified White cell, (image taken from [36])

2.3 Absorption Spectroscopy

Although there are many different types of spectroscopy it is the absorption of light by molecular gases that forms the basis of this thesis. A basic understanding of the theory behind these processes is essential.

In the mid-infrared region ($3\mu\text{m}\rightarrow 15\mu\text{m}$) direct absorption can be used over the more complicated methods of frequency or amplitude modulation due to the strong absorption of molecular gases in this region. Absorption of light causes the molecule to change energy levels, it does this by changing the molecular vibration and rotation.

As in the quantum mechanical description of atoms, molecules also have an associated eigenfunction, also called the wavefunction, Ψ . They have a set of linearly independent eigenvalues that correspond to the energy levels. To calculate these energy eigenvalues requires a Hamiltonian, for molecular systems the Hamiltonian contains all the relevant degrees of freedom, i.e. electronic, vibrational and rotational. In the Born-Oppenheimer approximation and similar other approximations, this Hamiltonian can be expanded as

$$H_{evr} = H_e + H_v + H_r \quad (2.4)$$

and the wavefunction can be expanded

$$\Psi_{evr} = \psi_e \cdot \psi_v \cdot \psi_r \quad (2.5)$$

By using Hougén's notation [37] the Hamiltonian can be written in the form

$$H = H_{ev} + H_r \quad (2.6)$$

where H_{ev} is the vibrational-electronic part or non-rotational part of the Hamiltonian. The remainder, H_r , is the rotational part and involves the rotational variables, the total angular momentum and many of the coordinates and momenta occurring in H_{ev} . This permits the energy levels associated with the different types of motion to be calculated more easily. For the infrared region it is the vibration and rotation of molecule that form the energy transitions observed. For an electron to change energy level it requires light with far more energy than that of infrared light, usually visible or ultra-violet light is required.

The rotation of molecules is generally described in the molecular frame of reference with three principal axes of rotation, K_a , K_b and K_c . The K_a and K_c axes lie in the same plane with the K_b axis perpendicular to both the others. The moment of inertia possessed by the molecule as it rotates about these axes can be used to classify the molecules. The moment of inertia, I , of any molecule when rotating about any axis is given by

$$I = \sum_i m_i r_i^2 \quad (2.7)$$

Where m_i is the mass of atom i and r_i is the distance from the inertial axis of atom i . The inertial axis of largest momentum is by convention the K_c axis with K_b being next in magnitude and the K_a axis having the least momentum, such that

$$I_c \geq I_b \geq I_a \quad (2.8)$$

Rotational constants associated with these moments of inertia, A , B and C can be calculated via

$$A = \frac{\hbar}{4\pi I_a c}, \quad B = \frac{\hbar}{4\pi I_b c}, \quad C = \frac{\hbar}{4\pi I_c c} \quad (2.9)$$

Molecules can be grouped together into four distinct groups, Linear, Spherical Top, Symmetric Top and Asymmetric Top. Symmetric and Asymmetric tops can be further subdivided to Oblate and Prolate Symmetric Tops and to Near-oblate and Near-prolate Asymmetric Tops using their moments of inertia, table 2.2. The Ray asymmetry parameter, κ , given by equation 2.10. It determines how oblate or prolate a molecule is.

$$\kappa = \frac{2B - A - C}{A - C} \quad (2.10)$$

The value of κ ranges from -1 for the prolate limit to +1 for the oblate limit.

Moment of Inertia	Molecular Classification
$I_c=I_b>I_a=0$	Linear
$I_c=I_b=I_a$	Spherical Top
$I_c>I_b=I_a$	Oblate Symmetric Top
$I_c=I_b>I_a$	Prolate Symmetric Top
$I_c>I_b \approx I_a$	Near-Oblate Asymmetric Top
$I_c \approx I_b > I_a$	Near-Prolate Asymmetric Top

Tab. 2.2: Molecular classification depending on their moments of inertia.

Rotation of diatomic molecules can be modeled using the rigid rotor approximation. In this approximation it is assumed that the bond between the atoms is a massless rigid rod. Although a useful starting point the rigid rotor model should not be used when modeling real molecules. The moment of inertia equation reduces to

$$I = \mu r^2 \quad (2.11)$$

here μ is the reduced mass of the two atoms and r is the internuclear separation. Allowed rotational energy levels can be found using the Schrödinger equation and take the form [38]

$$E_j = \frac{\hbar}{4\pi I_c} J(J+1) = BJ(J+1) \quad (2.12)$$

J is the rotational quantum number and as J increases the separation of the energy levels also increases (except $J=0 \leftrightarrow J=0$). Selection rules for energy levels dictate that J varies as

$$\Delta J = \pm 1 \quad (2.13)$$

A $\Delta J = 0$ transition is also permitted for linear molecules with a change in the vibrational angular momentum, if present. J is usually an integer, $J \in \mathbb{Z} \geq 0$, but can also be half-integer for radicals with unpaired electron spin as in OH and NO.

When this is substituted into the energy level equation, eqn. 2.12, and obeying the selection rules it can be shown that the separation between spectral lines generated is $2B$. It is conventional to express the rotational (or vibration-rotation) energy levels of a molecule in either frequency (MHz), or in wavenumbers (cm^{-1}) [38]. An exception to this selection rule is the open

shell molecules like nitric oxide, these have an electronic angular momentum in the ground electronic state which results in selection rules [39]

$$\Delta J = 0, \pm 1 \quad (2.14)$$

Each rotational energy level can be described as being symmetry positive or negative with respect to inversion (parity), this depends on whether the rotation results in a reflection of all the particles (electrons and nuclei) in the molecule and this reflection changes the sign of the wavefunction or leaves it unchanged. The symmetry behavior of the molecule depends solely on the symmetry behavior of the rotational part of the wavefunction, ψ_r , the electronic and vibrational (ψ_e and ψ_v) are unaffected by inversion in the case of electronic ground states of most known linear molecules, O_2 is negative in Ψ_e . For diatomic molecules the even rotational levels are positive and the odd are negative [40]

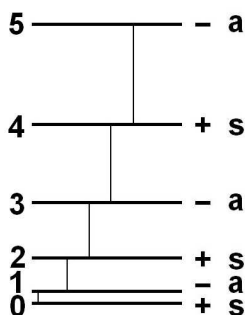


Fig. 2.10: Example of the rotational energy levels of a linear molecule. The symmetric and antisymmetric nature of the positive and negative levels of a molecule with point group $D_{\infty h}$.

Figure 2.10 gives an example of the positive and negative nature of the even and odd rotational energy levels of a linear molecule as J increases. In highly symmetric molecules, some atoms can be indistinguishable with respect to permutation, and then the Pauli principle applies. This can have the effect that different rotational levels have different statistical weights (nuclear spin statistics).

The addition of nuclear spin results in perturbations of the rotational energy levels where the molecule has a centre of symmetry. This can result in spectral lines being missing if the spins of all nuclei are zero, the antisym-

metric rotational levels are missing i.e. for Σ_g^+ electronic states of the odd rotational levels are absent [40].

As well as rotation the vibration of molecules has an effect on energy levels. When absorption of light causes the bond between the atoms of a diatomic molecule to change from equilibrium position there is a restoring force, similar to a spring, that can be approximated with Hooke's law. The resultant energy of the system is found by

$$E = \frac{1}{2}k(r - r_0)^2 \quad (2.15)$$

where k is the spring or force constant, r is the separation of the nuclei and r_0 is the average internuclear separation. This parabolic function, when applied to diatomic molecules, refers to vibrations that match the simple harmonic oscillator, frequency of oscillation of the system given by

$$\omega = \frac{1}{2\pi c} \sqrt{\frac{k}{\mu}} \quad (2.16)$$

Again solving the Schrödinger equation, this time for the simple harmonic oscillator using the energy potential shown in eqn. 2.15 has solutions given by

$$E_v = h\nu\left(v + \frac{1}{2}\right) = \omega\left(v + \frac{1}{2}\right) \quad : v \in \mathbb{Z}_{\geq 0} \quad (2.17)$$

Where v is the vibrational quantum number and have the selection rules

$$\Delta v = \pm 1 \quad (2.18)$$

For strong (fundamental transitions). In addition, $\Delta v = \pm 2, \pm 3$ etc is allowed for weaker overtone transitions.

Absorption can result in both rotational and vibrational transitions of the molecule simultaneously. These transitions must also adhere to the selection rules of $\Delta J = \pm 1$ and $\Delta v = \pm 1$ that govern the individual transitions. Energies of ro-vibrational transitions are the sum of the individual energies due to the Born-Oppenheimer and related approximations used earlier to separate the wavefunction into its component parts. Spectral lines associated to these transitions have a separation of $2B$ centered at frequency ω .

The approach so far has been of a simplistic harmonic oscillator, in reality vibrations in molecules do not follow the harmonic oscillator. When a diatomic molecule vibrates there is the chance that the bond can break, depending on the energy of the absorbed photon. A better approximation of the vibrational energy of the molecule is the Morse potential [41] given by

$$V(r) = D_e(1 - \exp^{-a_e(r-r_0)})^2 \quad (2.19)$$

where D_e is the dissociation energy, r and r_0 are as defined in eqn. 2.15 and a_e is found via

$$a_e = \sqrt{\frac{k_e}{2D_e}} \quad (2.20)$$

where k_e is the force constant analogous to the force/spring constant used in the simple harmonic oscillator. As the internuclear separation varies the energy of the system due to the Morse potential varies as

$$\begin{aligned} \text{at } r = r_0 \quad V(r) &\rightarrow 0 \\ \text{at } r \rightarrow \infty \quad V(r) &\rightarrow D_e \end{aligned}$$

Unlike the evenly spaced energy levels in the harmonic oscillator, spaced by \hbar , the Morse potential energy level separation decreases as the energy approaches the dissociation energy, figure 2.11. The dissociation energy, D_e , is greater than the actual energy required for dissociation, D_0 , due to the zero point energy of the lowest vibrational level ($v=0$).

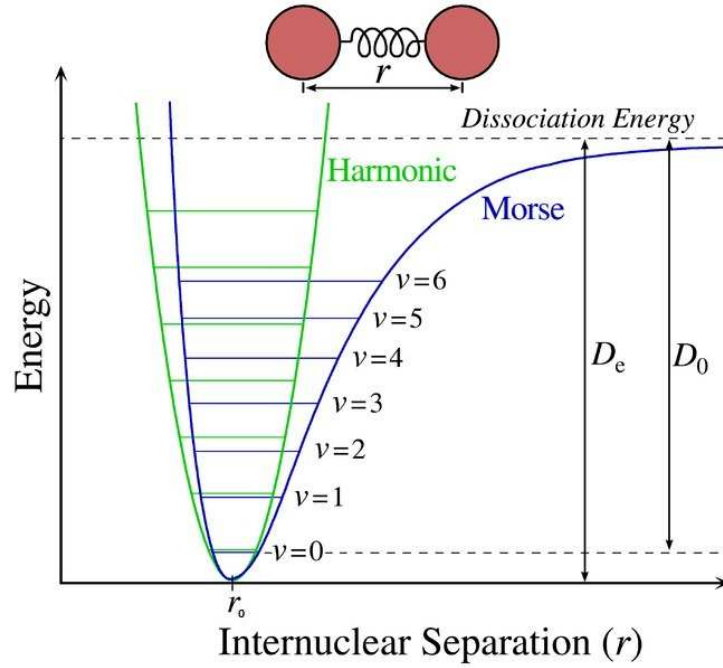


Fig. 2.11: Morse potential (blue) and the harmonic oscillator (green). (Taken from http://en.wikipedia.org/wiki/Morse_potential)

By solving the Schrödinger equation using the Morse potential the vibrational energy levels can be calculated via

$$E_v = \omega\left(v + \frac{1}{2}\right) - \omega\chi\left(v + \frac{1}{2}\right)^2 \quad (2.21)$$

where ω is the oscillation frequency and $\omega\chi$ is the anharmonicity constant given approximately by

$$\omega\chi = \frac{a_e^2 \hbar}{2\mu\omega} = \frac{\hbar\omega}{4D_e} \quad (2.22)$$

With μ being the reduced mass, the $\omega\chi\left(v + \frac{1}{2}\right)^2$ term gives rise to the decreasing energy level separation shown in figure 2.8. With the Morse potential the selection rules change to

$$\Delta v = \pm 1, \pm 2, \pm 3, \dots \quad (2.23)$$

This change in selection rule introduces overtones with transitions relating to the selection rules greater than $\Delta v = \pm 1$ being overtones, i.e. selection rules $\Delta v = \pm 2, \pm 3$ are the first and second overtones, also possible for harmonic oscillator. Transitions at these overtones typically occur at 2ω and 3ω respectively with transition strength decreasing by a factor of about one hundred for every overtone above the fundamental transition.

The rigid rotor model gives a good approximation for rotational energy transitions however real molecules are not confined in this manner. As the angular velocity of the molecular rotations increases the internuclear separation, previously defined as r in eqn. 2.11, also increases. The result of increasing r is an increase in the moment of inertia as per eqn. 2.11, in certain molecules this causes a break in symmetry and is called centrifugal distortion. The result of increased inertia is a decrease in the rotational constant. Solving the Schrödinger equation for a non-rigid rotor gives solutions via

$$E_j = BJ(J + 1) - DJ^2(J + 1) \quad (2.24)$$

where D is centrifugal distortion constant such that

$$D = \frac{\hbar^3}{4\pi r^2 I^2 k c} \quad (2.25)$$

This distortion manifests itself as the rotational energy levels are closer together with increasing J values. Selection rules are the same as for the rigid rotor model. Spacing of spectral lines given by

$$\tilde{\nu}_{J' \leftrightarrow J''} = 2B(J'' + 1) - 4D(J'' + 1)^3 \quad : J'' \in \mathbb{Z}_{\geq 0} \quad (2.26)$$

Up until now the focus has been on the rotations and vibrations of diatomic molecules and the next logical step is to consider polyatomic molecules. When dealing with polyatomic molecules the degrees of freedom are not as simple as with diatomics. Polyatomic molecules have $3N-5$ possible vibrations for linear molecules and $3N-6$ possible vibrations for non-linear molecules. This comes from a combination of each atom having three degrees of freedom, the molecule itself also having three degrees of freedom for translation and another three for rotation for a nonlinear molecule and the remaining factors relate to each atoms motion relative to each other (vibration). With a linear molecule the difference comes from their being no degree of freedom corresponding to rotation about the internuclear axis [39].

Due to the difference in the degrees of freedom the vibrations of polyatomic molecules differ, as previously discussed diatomic molecules undergo a simple symmetric stretching vibration whereas polyatomic molecules can have symmetric stretching vibration, antisymmetric stretching and various bending vibrations depending on the shape and composition of the molecule. If these vibrations cause a change in the molecular electric dipole moment they are described as being infrared active and can contribute to the vibrational absorption spectrum. Selection rules for polyatomic molecules are different than for diatomic molecules and are determined by the point group and allowed transitions, details for determining the point group of molecules can be found in many text books (for example [40], [39]) and are not covered in this thesis. The result of these vibrations and selection rules are combination bands, for example acetylene has a strong combination band in the $8\mu\text{m}$ ($\nu_4 + \nu_5$) figure 2.12 shows vibrational transitions of acetylene. In general combination bands are weaker than fundamental bands.

Rotations of linear polyatomic molecules is similar to rotations of diatomic molecules and the associated energy levels can be found using the same expressions as the diatomic molecules.






	Type	Band	Band centre/cm ⁻¹	IR Active
	Symmetric CH Stretch	ν_1	3374	no
	Symmetric CC Stretch	ν_2	1974	no
	Antisymmetric CH Stretch	ν_3	3287	yes
	Trans Bend	ν_4	612	no
	CIS Bend	ν_5	729	yes

Fig. 2.12: Vibrational modes of acetylene with band centres.

In the case of symmetric top molecules, such as ammonia (oblate) and chloromethane (prolate), the rotational energy levels are more complicated as the molecule can rotate about two axes. This means a second quantum number is required to calculate the energy levels as well as J , the total angular momentum. This takes the form of K and is the projection of the rotation onto the main axis of rotation. Thus the energy levels for a prolate symmetric top, non rigid rotor, can be found by

$$E_{J,K} = BJ(J+1) + (A-B)K^2 - D_J^2(J+1)^2 - D_{JK}J(J+1)K^2 - D_K K^4 + HOT \quad (2.27)$$

where D_J , D_{JK} and D_K are the centrifugal distortion constants, A and B are the rotational constants about the K_a and K_b axes respectively (defined in eqn. 2.9), J takes the value of any integer such that $J \in \mathbb{Z}_{\geq 0}$, HOT refers to Higher Order Terms and K takes the values

$$K = -J, -(J-1), -(J-2), \dots, 0, \dots, J-2, J-1, J \quad (2.28)$$

For an oblate top the A rotational constant is replaced by C , the rotational constant about the K_c axis. Selection rules for these molecules are

$$\Delta J = \pm 1 \quad \Delta K = 0 \quad (2.29)$$

This means the spacing of spectral lines is the same as a linear molecule with $J+1$ additional lines for each of the rotational transitions due to K .

The rotation vibration selection rules differ as the type of vibrations differ. For polyatomic molecules the vibrations can be parallel, on the same axis as the rotation, or perpendicular, as the name suggests vibrations are at 90° to the rotational axis. The selection rules differ such that for a parallel vibration

$$\Delta J = \pm 1 \quad \text{and} \quad \Delta v = \pm 1, \pm 2, \pm 3 \dots \quad (2.30)$$

and for perpendicular vibration

$$\Delta J = 0, \pm 1 \quad \text{and} \quad \Delta v = \pm 1, \pm 2, \pm 3 \dots \quad (2.31)$$

These perpendicular vibrations give rise to transitions between vibrational levels that preserve the rotation of the molecule, these are known as Q-branch transitions corresponding to the $\Delta J = 0$ selection rule. More complicated selection rules arise when dealing with symmetric tops, the selection rules of parallel vibrations are

$$\Delta J = 0, \pm 1, \quad \Delta v = \pm 1, \quad \Delta K = 0 \quad (2.32)$$

and for perpendicular vibrations

$$\Delta J = 0, \pm 1, \quad \Delta v = \pm 1, \quad \Delta K \pm 1 \quad (2.33)$$

These perpendicular bands give rise to complicated spectral patterns. For all molecules the rotational selection rules for ΔJ correspond to groups of spectral lines, branches, such that

$$\Delta J = -1 \text{ (} P \text{ - Branch)}, \quad \Delta J = 0 \text{ (} Q \text{ - Branch)}, \quad \Delta J = 1 \text{ (} R \text{ - Branch)} \quad (2.34)$$

Analysis of the rotations and vibrations of more complicated molecules can be found in textbooks such as Herzberg's "Infrared and Raman Spectra of Polyatomic Molecules" [40].

These transitions usually take place when light of an appropriate frequency is absorbed by the molecule. In most laboratories this is performed using lasers. When the intensity of the laser light does not perturb the population distribution of the energy levels in the system being studied two processes occur.

In general transitions can be described as a two level system, as absorption takes place the molecule goes into an excited/upper state. This tends to equalize the populations of upper and lower states. The lifetime of the molecule in the upper state is denoted as T_1 , the transverse relaxation time, the time taken for the population of upper state molecules to de-excite. As absorption depends on the population difference between the upper and lower states an equalization of the populations is the best that can be achieved.

The linear polarization of most lasers changes the polarization of the molecule by vibrational excitation. This can be selective depending on the orientation of the molecule and has quantum number M_J . M_J is the projection of the total angular momentum onto the fixed space Z-axis [42]. The dephasing of the transition dipole moment, denoted as T_2 , is called the longitudinal relaxation time.

As long as the interaction time of the laser light with the molecule is greater than T_1 and T_2 , providing no saturation occurs, then the change in light intensity as it passes through the medium per unit of thickness is

$$dI(\nu) = -k(\nu)I(\nu)dx \quad (2.35)$$

where $I(\nu)$ is the initial intensity and $k(\nu)$ is the absorption coefficient of the medium at frequency ν . By integrating with respect to x the Beer-Lambert relation is obtained

$$I(\nu) = I_0 \exp[-k(\nu)l] \quad (2.36)$$

where I_0 is the initial light intensity and l is the thickness of the medium, also referred to as the optical path length. Integrating over an absorption line gives the integrated absorption coefficient that relates the populations of upper and lower states to the frequency via

$$\int_{j \leftarrow i} k(\nu) d\nu = \frac{h\nu_{ji}}{c} B_{ji} (N_i - N_j) \quad (2.37)$$

where i and j are the lower and upper energy levels, respectively, of the transition associated with the absorption, correspondingly N_i and N_j are the populations of these levels and B_{ji} is the Einstein B coefficient for absorption.

A general version, for use with gas in long path absorption cells, of the Beer-Lambert relation takes the form

$$I = I_0 e^{-\alpha Pl} \quad (2.38)$$

Where I_0 is as defined previously, P is the partial pressure of the gas, l is the optical path length and α is the linear absorption coefficient given by

$$\alpha = N S_{line} f(\nu - \nu_0) \quad (2.39)$$

Where N is the number of absorbing molecules per atmosphere, $f(\nu - \nu_0)$ is the lineshape function for the absorption line centered at ν_0 and S_{line} is the line intensity. S_{line} relates to the absorption coefficient $k(\nu)$ by

$$S_{line} = \frac{8\pi^3}{3hc} \left(\frac{N_i}{g_i} - \frac{N_j}{g_j} \right) \nu_{ji} S_{ji} = \int_{j \rightarrow i} k(\nu) d\nu \quad (2.40)$$

This comes from substituting the expression for the Einstein B coefficient into eqn. 2.37, where g_i and g_j are the statistical weights of the lower and upper energy levels. The general expression for the line strength is [38]

$$S_{ji} = \sum_j \sum_i 3 |\langle j | \mu_F | i \rangle|^2 \quad (2.41)$$

where μ_F is the component of the electric dipole moment operator relative to one axis fixed in space.

The absorption coefficient becomes a linear relation between the lineshape function and the line intensity

$$k(\nu) = S_{line} f(\nu - \nu_0) \quad (2.42)$$

where $f(\nu - \nu_0)$ is a lineshape function normalized such that

$$\int_{-\infty}^{\infty} f(\nu - \nu_0) d\nu = 1 \quad (2.43)$$

The Beer-Lambert law is only valid as long as there is no saturation of the absorption line.

The lineshape of an absorption feature within the linear regime of the Beer-Lambert law can fall into three categories. These are the Doppler broadened lineshape, the pressure broadened lineshape and an intermediate which is a convolution of the two other lineshapes. There is another lineshape to be discussed in subsection 2.3.1 that arises due to the laser interaction time with the molecule being shorter than the relaxation times, T_1 and T_2 , usually when the gas is at low pressure, resulting in rapid passage and free induction decay signals.

The Doppler broadening dominates when the gas within the system is at low pressure, but not such that rapid passage effects occur, and as the term suggests the velocity components of the different molecules affect the lineshape, the wings at either side of the absorption wavelength are referred as the blue side for higher frequency and red side for lower frequency. The different velocity components can be modeled as a series of Lorentzian lines due to the natural linewidth that form a Gaussian envelope, see figure 2.13.

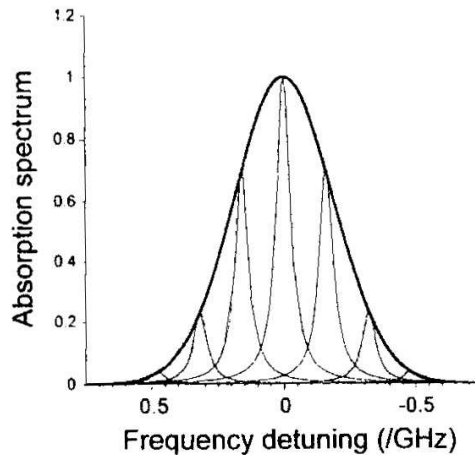


Fig. 2.13: Schematic of modeled Lorentzian lineshapes representing the different velocity components within the Gaussian envelope of a Doppler broadened line, for clarity only seven lines are shown in reality all possible velocity components would need to be considered.

The Gaussian lineshape associated with the Doppler broadening takes the form

$$f_G(\nu - \nu_0) = \frac{1}{\delta\sqrt{\pi}} \exp \left[- \left\{ \frac{\nu - \nu_0}{\delta} \right\}^2 \right] \quad (2.44)$$

where

$$\delta = \frac{\nu}{c} \sqrt{\frac{2kT}{M}} \quad (2.45)$$

where k is Boltzmann's constant, T is the temperature in Kelvin, and M is the mass of the molecule. The half-width at half-maximum (HWHM) of the Gaussian is given by $\delta\sqrt{\ln 2}$

Pressure broadening, as the name suggests, is due to the pressure in the system due to either the pressure of the gas under discussion being increased or the introduction of a buffer gas, normally a gas that does not absorb in the same region. The lineshape takes the form of a Lorentzian, i.e.

$$f_L(\nu - \nu_0) = \frac{1/\gamma_L}{(\nu - \nu_0)^2 + \gamma_L^2} \quad (2.46)$$

where γ_L is the HWHM and is given by

$$\gamma_L = (\gamma_s P_s + \gamma_f P_f) \sqrt{\frac{T_0}{T}} \quad (2.47)$$

where γ_s and γ_f are the self-broadening and foreign gas broadening coefficients respectively, P_s and P_f are the partial pressures of the subject gas and the foreign gas respectively, T is the temperature and T_0 is a reference temperature (usually 296K).

At intermediate pressures both the Doppler broadening and pressure broadening affects the lineshape and a convolution of the two must be used, this is known as the Voigt profile and takes the form

$$f_V(\nu - \nu_0) = \frac{Bx}{\pi} \int_{-\infty}^{\infty} \frac{e^{y^2}}{x^2 + (z - y)^2} dy \quad (2.48)$$

where

$$B = \frac{1}{\gamma_D} \sqrt{\frac{\ln 2}{\pi}} \quad (2.49)$$

$$x = \frac{\gamma_L}{\gamma_D} \sqrt{\ln 2} \quad (2.50)$$

and

$$z = \frac{(\nu - \nu_0)}{\gamma_D} \sqrt{\ln 2} \quad (2.51)$$

The integral in eqn. 2.48 can be approximated using different techniques, however these will not be explored in this thesis. Work done by Whitting [43] and Olivero and Longbothum [44] has resulted in an approximation of the width of the Voigt function to be 0.02% accurate, given by

$$\gamma_V \approx 0.5346 \gamma_L \sqrt{0.2166 \gamma_L^2 + \gamma_D^2} \quad (2.52)$$

2.3.1 Rapid Passage

Rapid passage (RP) and free induction decay (FID) occur due to a combination of factors. When the pressure of the gas of interest is below that at which a Gaussian profile can be used to describe its lineshapes and the laser interaction time over the absorptive transition is less than the relaxation time of the molecule, i.e. the laser frequency undergoes a fast chirp, then the lineshape develops an asymmetry.

The effect was first seen during experimental work in nuclear magnetic resonance (NMR), and has been described in great detail by Ernst [45] and Abragam [46]. In these texts adiabatic rapid passage is being studied and to achieve the effect it required two passes of the system, the first to invert the population of the system and the second to monitor the population difference at a later time. This allowed the system to oscillate from the ground to excited state at the Rabi frequency. Following these methods Loy [47] applied them to the optical regime utilizing a line-tunable carbon dioxide laser, he used the R(6) line of CO₂ at 10.35 μm , and in doing so he observed an emission signal on the Q(5,5)_s→_a line of the ν_2 band of ammonia permitting him to plot a pressure dependence of T₁.

As near infrared diode lasers became prevalent experiments were being performed where the laser frequency was being rapidly swept by modulating the laser current, during which RP and FID signals were observed. These ranged from the laser cooling of ⁸⁵Rb atoms [48], to gas phase spectra of iodine [49] and solid state spectra of ions [50]. These experiments focused on the FID effects and how they could be used to explore dipole dephasing times in gases and solids.

Although originally utilized for modeling FID in NMR, modification of the Bloch vector approach [51] into the Maxwell-Bloch equations [52] still provides a useful tool for simulating the FID effect under different conditions, see for example refs [53] [54] and [55].

During laser absorption spectroscopy of molecules the spectra also display both RP and FID if specific conditions occur. These conditions are that the gas pressure is low and the sweep rate of the laser frequency should result in the time taken for the laser to scan through the Doppler width of the absorption line to be less than the relaxation time. The low gas pressure means that the time between collisions is greater than the laser radiation interaction time with the molecule, this is of the order of 2 to 6 ns depending on chirp-rate of the laser. The other condition is that the laser radiation interaction time with the molecule should be less than the longitudinal (population) and transverse (polarization), relaxation times T_1 and T_2 as defined in section 2.3.

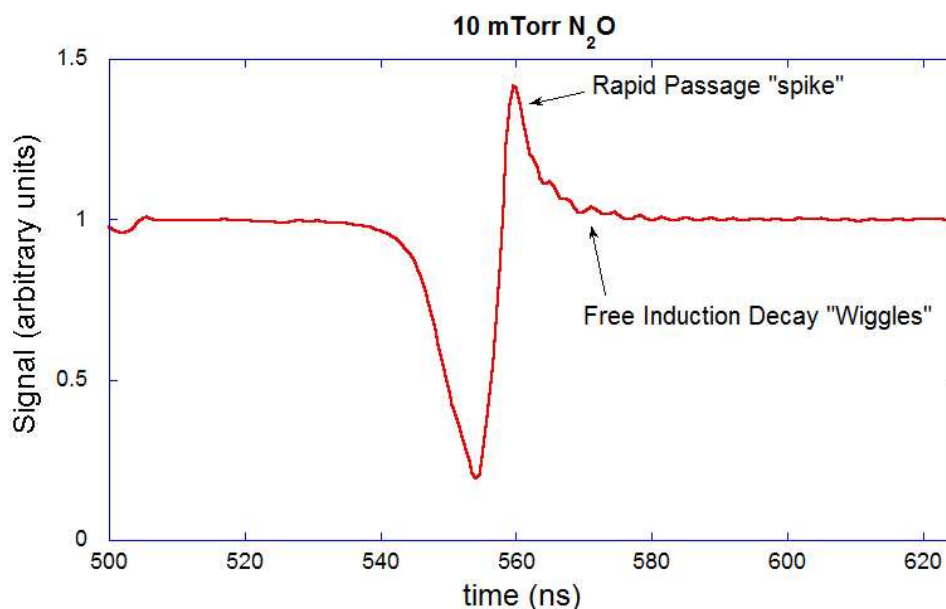


Fig. 2.14: Characteristic Rapid Passage "Spike" and Free Induction Decay "Wiggles" on the $P(10)_e$, ν_1 singlet of nitrous oxide at a pressure of 10mTorr. Laser settings were such that the corresponding chirp-rate was 40MHz/ns.

Figure 2.14 shows nitrous oxide at a pressure of 10 mTorr, recorded within a 62m path length astigmatic Herriott cell in the lab at Strathclyde University. Clearly visible is the rapid passage "spike" followed by free induction decay "wiggles", with laser settings chosen such that the chirp-rate was minimized and laser power reduced in order to avoid saturation of the absorption lines of the ν_1 fundamental antisymmetric stretch. At this pressure the longitudinal relaxation time, T_1 , is in the microsecond scale.

Although the effects seen using the pulse-modulated chirped QC lasers displays similar effects seen during the NMR and the early near-infrared diode laser work it is not Adiabatic Rapid Passage (ARP). For ARP the lasers used need to have greater power than that produced by the pulsed QC lasers used throughout this thesis. This is the adiabatic condition and requires sufficient laser power to cause a population inversion from lower to upper energy levels and for the system to oscillate at the Rabi frequency [56]. The on resonance Rabi frequency is given by

$$\Omega = \frac{\mu E}{\hbar} \quad (2.53)$$

where μ is the dipole moment and E is the field strength. For the adiabatic condition to be met requires

$$\Omega^2 \gg \frac{d\nu}{dt} \quad (2.54)$$

For the 7.84 μm laser used which has an average power of 45mW and a mode waist in the order of 2mm the calculated Rabi frequency for the nitrous oxide transition would be approximately 12 MHz. So even though the laser was set in order to minimize the chirp rate, done by cooling the laser to -24°C , slowing the repetition rate to 2.5 KHz and a voltage of 13 V which results in driving the laser just above threshold, the Rabi frequency is less than the chirp rate of 40 MHz/ns. Thus the rapid passage observed cannot be adiabatic rapid passage and is due to the polarized laser beam aligning the dipole moments of the molecules with respect to the beam. It is the relaxation from alignment that gives the emission "spike", the rapidly changing laser frequency then interacts with the molecule as the polarization alignment relaxes resulting in the beat frequency being set up between the two levels resulting in the free induction decay "wiggles".

Although the theory behind the function of the QC lasers is well understood and although they are widely used as a replacement for lead salt and

CO/CO₂ lasers within spectrometers where size and temperature are a concern in the spectrometer design, care must be taken when driving the QC laser. Fast tuning of the QC lasers result in asymmetric line-shapes and non-linear optical effects, rapid passage and free induction decay signals. However these effects can be minimized by careful choice of the pressure within the spectrometer absorption cell, this will be discussed in Chapter 4.

Although the theory behind the function of the QC lasers is well understood. As is their use as a replacement for lead salt and CO/CO₂ lasers within spectrometers where size and temperature are a concern in the spectrometer design. However care must be taken when driving the QC laser. Fast tuning of the QC lasers result in asymmetric line-shapes and non-linear optical effects, such as rapid passage and free induction decay signals. These can be minimized by the introduction of molecular species that do not absorb in same the spectral region of the target gas or for atmospheric testing the pressure within the test cell to be chosen such that it performs the same effect as adding a buffer gas.

2.4 Pickett Spectral Simulation Programs

These are a series of computer programs written by Herb Pickett [57] designed to calculate line positions and intensities for molecular gases. This is done through the input files that contain parameters and variables as well as commands for the programs to perform specific tasks. The current versions of two main programs used in the course of the $\text{NO}_2/\text{N}_2\text{O}_4$ analysis, SPFIT and SPCAT, can be found, already compiled, free to use for the spectroscopy society on the NASA Jet Propulsion Laboratory website [58]. Other programs are also included in the download pack but were not used in this thesis.

The first step is to use SPFIT (the fitting program), this requires two input files, a .par file and a .lin file. The .par file contains the values of constants as well as control flags and declarations that are used in the program, along with the .lin file which contains a list of the transitions and the associated frequency of the transition, to generate a .var file that it is used by SPCAT (the predictive program), as well as a backup (.bak file) of the original input .par file, a modified version of the .par file, a .bin file (containing parameters that can be used by SPCAT and a .fit file that is the main out-put file from SPFIT.

The majority of the simulated spectra generated during the analysis was performed using SPCAT. This program also requires two input files, a .var file that contains constants, errors and matrix elements, this is usually generated by SPFIT. The other, .int, contains information for the intensity calculation.

As there is limited data on the NO_2 dimer it was not possible to generate a .lin file, however the download package contains a document that gives the information needed to format input files for each program. This was used to generate a .var and .int file for use with SPFIT, this newest version of the program no longer requires the .bin file.

The .var file contains most of the required information for the predictive program to generate the various output files. Within this file there are the band centres in wavenumbers for the absorption bands being simulated, i.e. the vibrational energies of the band as well as rotational constants and coupling terms depending on whether there is more than one band to be simulated. Figure 2.15 shows a typical .var file, the first three lines contain information that allows SPCAT to read the data such as the number of variables, the statistical weights and the Marquardt-Levenberg parameter.


```

N2O4 null/dark
 33 4248 20 0 1.7600E-012 6.0000E+002 1.0000E+
000 1.00000000000
a 1 3 0 49 0 1 1 0 0 0 0
10000 2.17908440E-01 1.00000000E-017 /A(0)
20000 1.22221002E-01 1.00000000E-017 /B(0)
30000 0.78340481E-01 1.00000000E-017 /C(0)
200 -6.15410000E-08 1.00000000E-017 /-DJ(0)
1100 7.70770000E-08 1.00000000E-017 /-DJK(0)
2000 -6.98430000E-08 1.00000000E-017 /-DK(0)
40100 -5.35590000E-08 1.00000000E-017 /delJ(0)
41000 -2.34090000E-08 1.00000000E-017 /delk(0)
300 7.48800000e-13 1.00000000E-017 /hj(0)
11 1.26255790E+03 1.00000000E+017 /E(1)
10011 2.17964600E-01 1.00000000E+017 /Del(A)
20011 1.19948100E-01 1.00000000E+017 /Del(B)
30011 0.77120800E-01 1.00000000E+017 /Del(C)
211 -6.15410000E-08 1.00000000E-017 /-DJ(0)
1111 7.70770000E-08 1.00000000E-017 /-DJK(0)
2011 -6.98430000E-08 1.00000000E-017 /-DK(0)
40111 -5.35590000E-08 1.00000000E-017 /delJ(0)
41011 -2.34090000E-08 1.00000000E-017 /delk(0)
311 7.48800000e-13 1.00000000E-017 /hj(0)
22 1.26355440E+03 1.00000000E+017 /E(2x6)
10022 2.17362900E-01 1.00000000E+017 /Del(A)
20022 1.21967500E-01 1.00000000E+017 /Del(B)
30022 0.78094800E-01 1.00000000E+017 /Del(C)
222 -6.15410000E-08 1.00000000E-017 /-DJ(0)
1122 7.70770000E-08 1.00000000E-017 /-DJK(0)
2022 -6.98430000E-08 1.00000000E-017 /-DK(0)
40122 -5.35590000E-08 1.00000000E-017 /delJ(0)
41022 -2.34090000E-08 1.00000000E-017 /delk(0)
322 7.48800000e-13 1.00000000E-017 /hj(0)
12 1.9121900E+00 1.00000000E-019 /Fermi
10012 7.0358000E-04 1.00000000E-019 /Fermi
112 -4.9921000E-04 1.00000000E-019 /Fermi
40012 -1.7459000E-04 1.00000000E-019 /Fermi

```

Fig. 2.15: Example of a .var file used in simulating a spectrum using the Pickett programs. Data for this file was taken from work done by Hepp *et.al* [59]

The other input file required by SPCAT is the .int file, although a simpler file it also contains essential information for the program to function. It only contains three lines but these contain flags that tell the program whether the calculations are in wavenumber or megahertz, the numerical value of the partition function, the corresponding temperature at which the partition function is calculated and the beginning and finishing \mathbf{F} quantum number, where $\mathbf{F} = \mathbf{J} + \mathbf{I}$, the sum of the rotational quantum number and the nuclear spin quantum number.

Output files from SPCAT are the .out file, this is the main output file containing the energies and transition frequencies, the .cat file, a catalogue file containing the calculated transitions only, the .str file, the transition dipoles and the .egy file that lists the energy levels, derivatives and eigenvectors.

The default setting for the temperature and partition function, for use in the .int file, is 300K. The partition function can be calculated, depending on the molecular classification, using equations found in many text books but equations for the more common molecular types have been listed on a web page by Kisiel [60] which provides a useful tool for the use of SPCAT and SPFIT. Part of the output of SPCAT is a list of different partition functions with corresponding temperatures, these can be noted and used to perform simulations at these temperatures.

Through programs written or modified in-house by Prof. Duxbury and previous group member Michael McCulloch the output files can be used, along with specific parameter files, to generate a plot of spectral lines fitted to line-shape profiles. The first step is to sort lines from the .cat file by using a program named sort2003, this program reads the .cat file and selects lines that fall within a specific wavenumber range. These are rewritten to a file than can be read by the broadening program. A parameter file, .prm file, is used as well as the .cat file for sort2003 to generate the ASCII format file required by the broadening program. This ASCII file contains the line positions, intensities, and half-width at half-maximum in wavenumbers. Other data introduced into the simulation, at this point, is the path length and pressure which the spectrum would have been recorded if done experimentally, these factors can have a dramatic effect on the number of lines visible with many more of the weaker transitions being visible.

The final step is to use the broadening program. This program fits line-shapes to the stick spectrum (the data in the other files are only the line position and intensity without any line-shape) depending on the parameters within the .prm file (which instructs the program to fit to Gaussian, Lorentz or Voigt profiles). The output of this program are graph files of an absorption spectrum, transmission spectrum or both. These files can be read by the majority of graphing software.

3. FIELD EXPERIMENTS

3.1 *Introduction*

This chapter is mainly concerned with experimental work carried out away from our laboratory. This experimental work consisted, mainly, of visits to the laboratory of Dr Iain Burns in the Department of Chemical and Process Engineering, University of Strathclyde. The group also had the opportunity to visit The Glasgow Vintage Vehicle Trust and participate in measurements of exhaust fumes of several vehicles from different decades. The diesel exhaust measurements were carried out in collaboration with previous group member Kenneth Hay during a short cross-over period between the end of K. Hays PhD and the start of the authors PhD. Experimental work on the flames at the Department of Chemical and Process Engineering were in collaboration with Dr Iain Burns and his students Jacqueline and Tiger for the methane measurements and with Jacqueline only for the ethylene flame.

Section 3.2 covers the visit to The Glasgow Vintage Vehicle Trust where the 4C-PQCLAS was used to, primarily, sample bus exhaust fumes from vehicles dating from the 1930's to the 1990's. Secondary to this was it would allow a comparison of the Cascade Technologies CT2400 with equipment currently used during the MOT testing of vehicles. Exhaust gas analyzers used for emission testing during MOT's are required to check the concentrations of CO, CO₂, O₂ and unburnt hydrocarbons. Some newer devices have the option of measuring NO, for example the Bosch BEA series which can detect NO at 1ppm. However they do not give any information of which hydrocarbon is being detected, whereas post analysis of spectra recorded by the CT-2400 can give this information. Other methods have been used to measure concentrations of various NO_x's [8] and of CO₂ [9]. This will be the first time a commercially available 4-channel spectrometer has been used to perform this type of measurements.

Section 3.3 covers the first visit to the Chemical and Process Engineering laboratory of Dr Iain Burns where methane as the fuel for combustion experiments is studied. Both the $4.86\mu\text{m}$ and the $7.84\mu\text{m}$ laser were used to perform measurements of combustion products. It is hoped that the high pressures and short path length through the plume of the flame will not have too much of a detrimental effect on the recorded spectra. As well as identifying combustion products the aim is to map how the flame develops through its plume.

Section 3.4 covers the return visit to Chemical and Process Engineering after alterations had been made to the flame conditions and the fuel was changed to ethylene. Again the $4.86\mu\text{m}$ and the $7.84\mu\text{m}$ laser were used to perform these measurements. The main aim is to detect if acetylene is being formed as a combustion product. Acetylene forming in gas flames is a precursor to soot formation in flames.

Section 3.5 shows the results of experiments to find out if it is possible to detect a beam reflected off a non-mirrored surface. If the reflected beam is of sufficient power then it may give rise to measurement being made when mirrors are not available or cannot be mounted in situ. It was hoped that if sufficient reflected radiation is detected then it may be possible to perform measurements of the combustion zone of a turbojet engine. These experiments were performed by the author and supervisor Professor Geoff Duxbury.

3.2 Bus Exhaust Fumes

The measurements in this section were carried out in collaboration with previous group member Kenneth Hay. The results have been previously included in the thesis of Kenneth Hay [29], so only a brief description of the experimental work and results are given here.

Buses are a major contributor of air pollution in most cities as they travel in set routes often completing the route several times daily as well as time stationary at traffic lights and bus stops with their engines regularly running all day. This adds up to a lot of exhaust fumes so a way to monitor them and determine their composition would aid in the development of cleaner, more efficient engines.

As a way to test what the spectrometer could detect in the exhaust fumes it was taken to the Glasgow Vintage Vehicle Trust. Dr Hay is a member of the trust and wanted to use the spectrometer to examine the exhaust gases of some of the vintage buses there as experiments had been performed previously on car exhausts fumes [61] using a single laser. Buses from different decades from the 1930's through to the 1990's were chosen in comparison. This would allow us to see what difference the age of a vehicles engine plays on the gases produced during combustion.

Year New	Chassis Type	Engine Type
1938	AEC Regent O661	AEC
1949	Albion Venturer CX37S	Albion
1959	Leyland Titan PD3	Leyland O.600
1967	Leyland Titan PD3A	Leyland O.600
1977	Leyland Atlantean AN68A/1R	Leyland O.680
1985	MCW Metrobus DR132/6	Cummins L10
1993	Leyland Olympian ON2R50C13V3	Cummins L10

Tab. 3.1: Buses studied for exhaust fume measurements.

For each bus tested the inlet pipe of the spectrometer was positioned in the place where the centre of the plume would be at a distance of 70cm from the end of the exhaust pipe.

This ensured that any reactive combustion products had time to react with atmospheric oxygen giving a more realistic measurement of pollutants.



Fig. 3.1: Sample pipe in exhaust plume.

Each bus was started from cold and allowed to run until the engines had warmed. From the concentrations extracted it was obvious that the main combustion products were carbon monoxide and carbon dioxide. CO_2 was measured in parts per million whereas the other gases were measured in parts per billion. There was surprising levels of formaldehyde (CH_2O) present for each bus except for the 1993 Leyland Olympian where the levels dropped significantly. It was suggested that this bus may have a more efficient engine however it had the same engine type as the 1985 MCW Metrobus, a Cummins L10. The most likely reason for the drop would be the introduction of catalytic converters as part of manufacturers meeting requirements under the clean air act 1993. As this bus had the most up to date engine/exhaust system its exhaust gases would be the closest match to modern buses. It was decided to see what difference revving the engine would make to the combustion products.

As the engine in the Leyland Olympian was already hot from the previous test, a test starting from hot, idling, revving and then idling was carried out, see figure 3.6. During the revving period the concentrations of CO and NO_2 drop dramatically. From these results it appears that the engines become more efficient during revving, this confirms the general consensus that stationary vehicles do produce greater amounts of pollution. To combat this Glasgow City Council have introduced legislation enabling officials to fine drivers who allow their vehicles to idle unnecessarily [62].

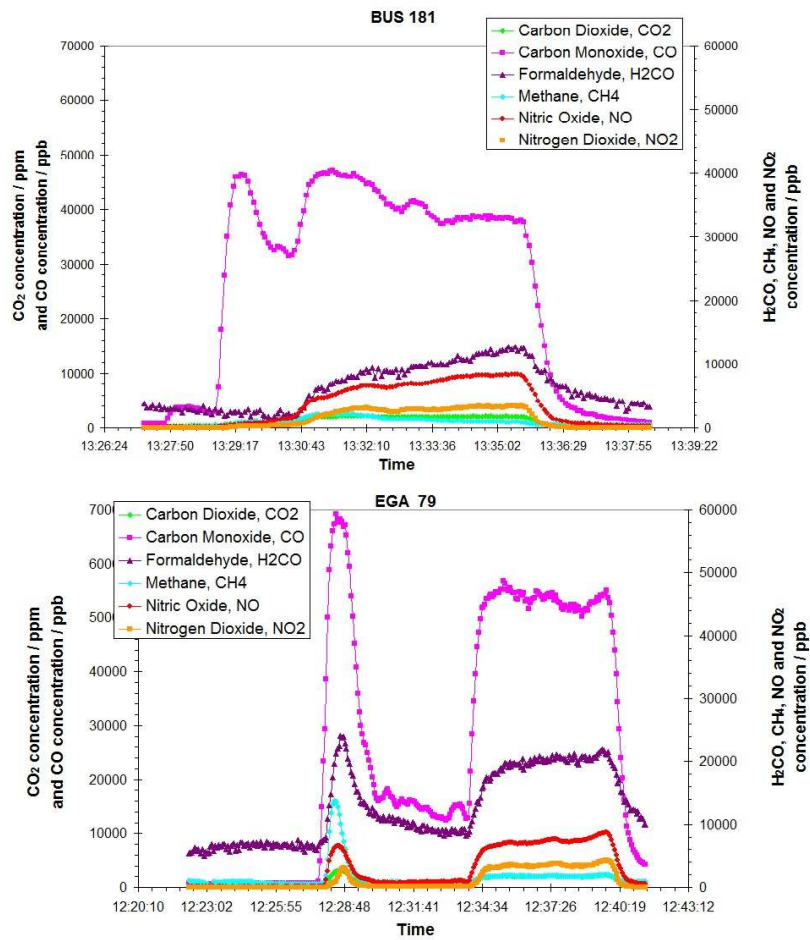


Fig. 3.2: Gas concentrations of a 1930's vehicle, top, and a 1940's vehicle, bottom.

There is however another reason that could have played a part in the drop in concentrations in figure 3.6, i.e. the increased pressure of exhaust gases traveling through the exhaust system resulted the gases having increased velocity when leaving the exhaust pipe and the inlet pipe not having the time to draw them into the spectrometer. This may have played a small role in the reduction so it needs to be mentioned, however it seems an unlikely cause for such a large drop. Concentrations of gases are extracted via software installed by Cascade Technologies on the control laptop.

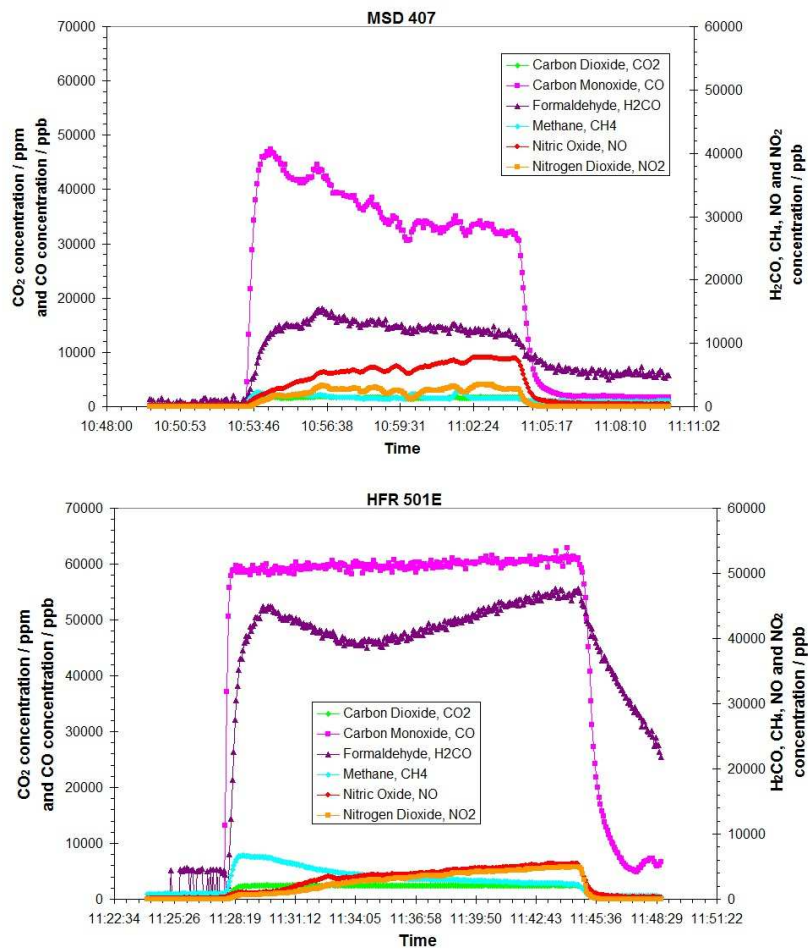


Fig. 3.3: Gas concentrations of a 1950's vehicle, top, and a 1960's vehicle, bottom.

The measurements on the exhaust fumes were carried out in collaboration with K. Hay. The data analysis done to generate the graphs in figures 3.2 to, and including, 3.6 was done by and reproduced with kind permission of K. Hay.

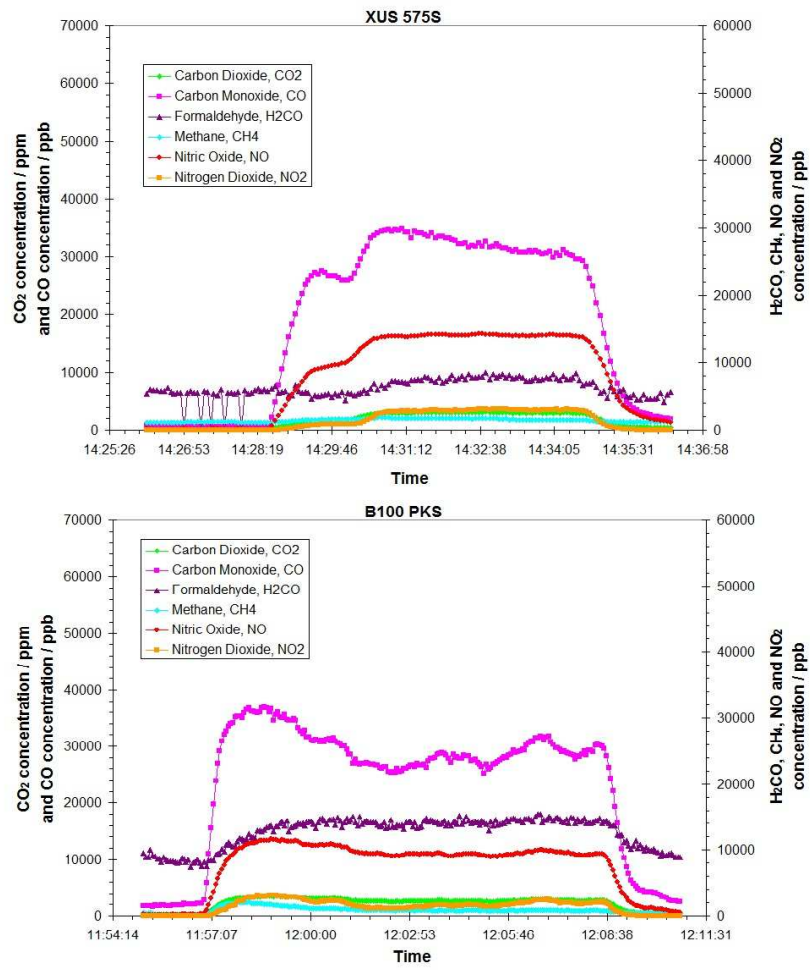


Fig. 3.4: Gas concentrations of a 1970's vehicle, top, and a 1980's vehicle, bottom.

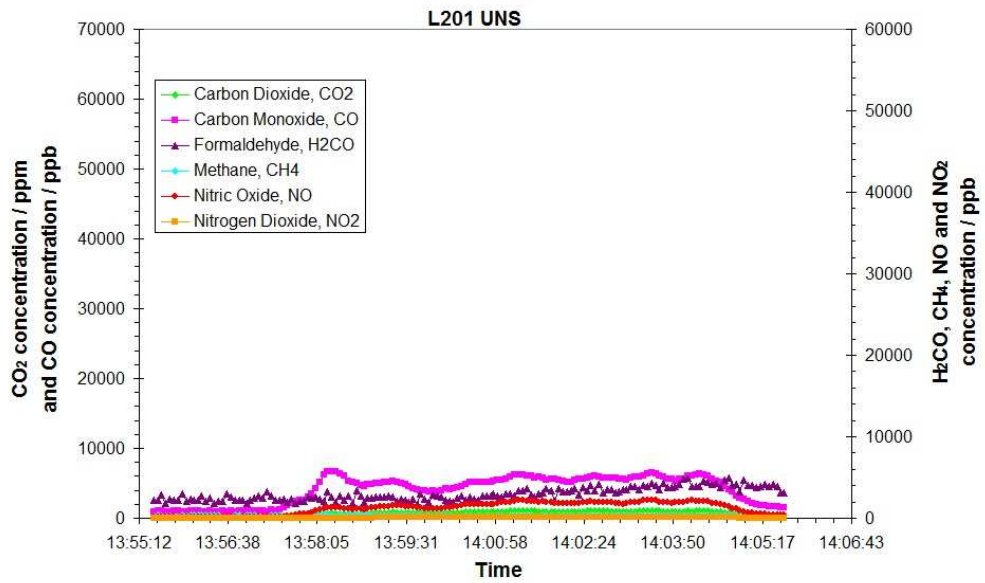


Fig. 3.5: Gas concentration of a 1990's vehicle.

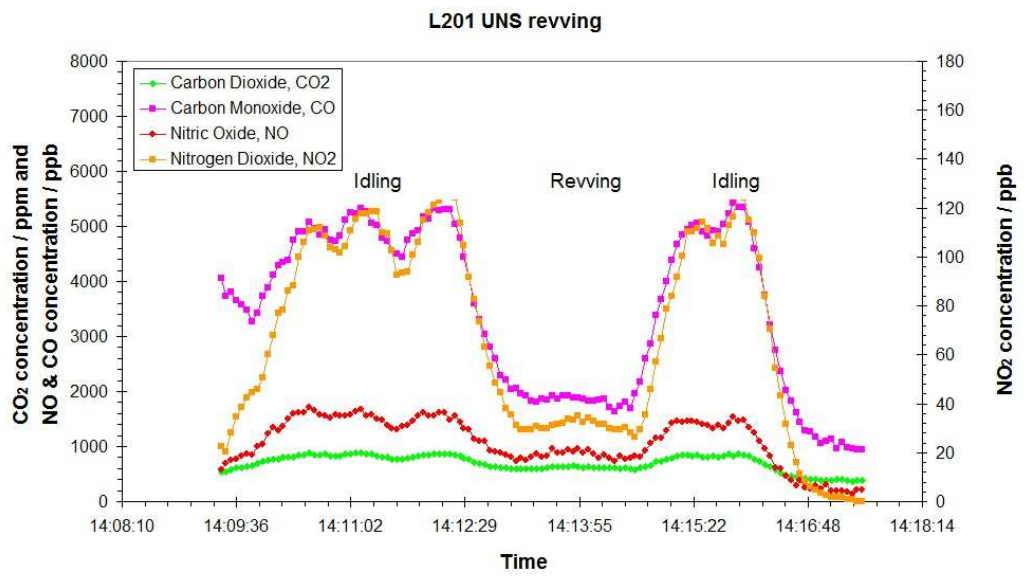


Fig. 3.6: Leyland Olympian engine emissions differences while idling and revving.

3.3 Methane Flame Measurements

In April 2010 the group was invited to perform some measurements of a flame burning various mixtures of methane/oxygen at the laboratory of Dr Iain Burns in the Chemical and Process Engineering Department of the University. The group there are involved in flame imaging using a Nd:YAG-pumped narrow-band dye laser and a ICCD camera researching the chemical mechanisms of combustion from accurate temperature determination to radical formation, previously they used diode lasers as their light source [63], [64]. The intention was to explore the combustion products, as the beam passed vertically through the plume, when the flame is forming soot. To achieve a sooting flame a fuel ratio high in methane was used and a steel block was placed at a height of $20mm$ above the burner so that it would disturb the plume causing carbon to form deposits.

Initial tests were performed using the $6.15\mu m$ laser (Laser 62). The detector was connected to a Cascade Technologies AV1500 averager before being connected to the control laptop. The setup is shown in Figure 3.7. The laser was set to operate at $0^\circ C$ with a voltage of 8V, repetition rate of 2.5KHz and a pulse length of 1300ns. These settings allowed us to tune the laser to the $R(7)_A$ methane line at 1626.53 cm^{-1} . This was to ensure we could actually obtain a spectrum with such a short path-length, in the order of $3cm$, with the gas pressure at atmospheric and the temperature of the gas in the order of $2000K$ or higher.

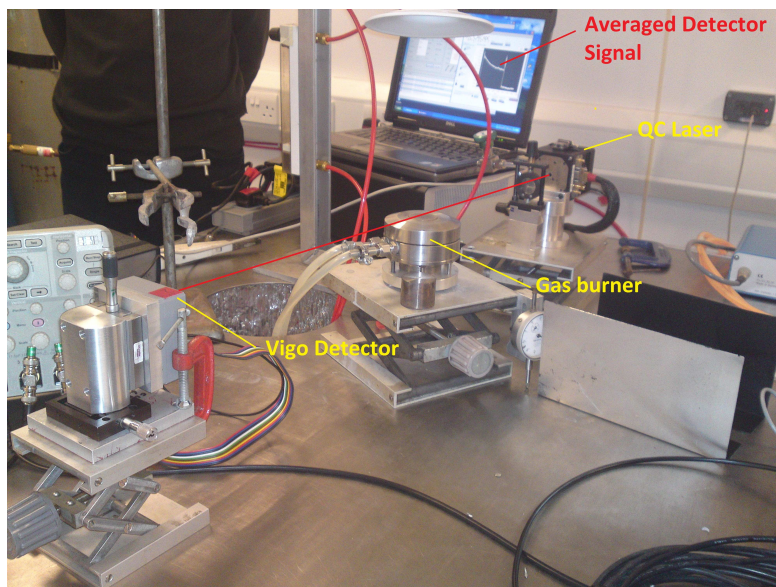


Fig. 3.7: Gas burner arrangement in relation to QC-Laser and detector, (the output of the AV1500 can be seen on the laptop screen in the background).

As shown in Figure 3.8 the methane line observed appeared very weak. The operational temperature of the laser was then changed to -15°C tuning to a higher frequency in an attempt to detect a stronger line. A stronger absorption line was found, unfortunately the line found was a strong water line, R(4) at 1626.06 cm^{-1} rendering the use of Laser 62 unsuitable.

Knowing the $4.86\text{ }\mu\text{m}$ laser, Laser 60, would detect carbon monoxide and carbon dioxide we switched lasers. Parameters were set to temperature of -10°C , applied voltage of 11.2V , repetition rate of 2.5KHz and pulse length of 1300ns . Even with the short path length through the plume the results were encouraging. Figure 3.9 clearly shows two strong carbon monoxide lines and a weaker carbon dioxide line.

As this proved the concept it was decided to continue with the main objective, i.e. to probe the sooting flame with the steel block in place to look for more exotic combustion product in particular acetylene. To assist in the analysis the laptop and AV1500 digitizer was replaced with the ACQIRIS AP200 digitizer card installed in a Ventrax PC. This also made it easier to operate both the laser and digitizer. The AV1500 relies on the attached laptop to perform the averaging of spectra, reducing processor and memory

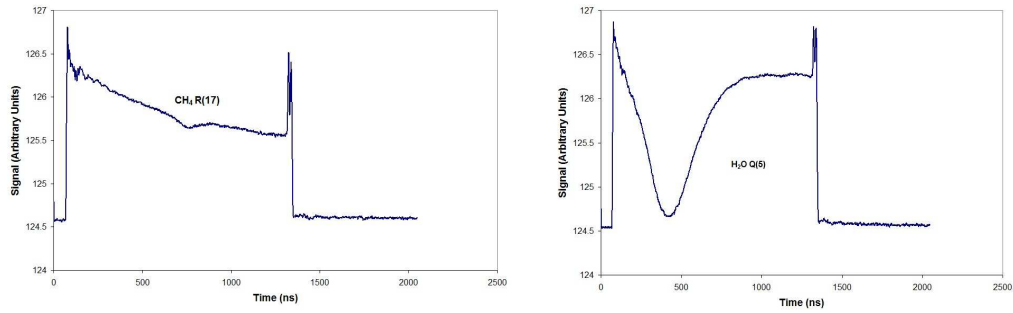


Fig. 3.8: Recorded output files from AV1500, CH_4 (left) and H_2O (right) lines observed by Laser 62. The units on y-axis are arbitrary and do not start at zero purely as a result of the software supplied to display the averager output.

resources for other applications, whereas the AP200 does all the averaging on board and displays the output as a normalized absorption spectra. The $7.84\mu m$ laser replaced the $6.15\mu m$ laser as it operates in a region with very few water absorption lines.

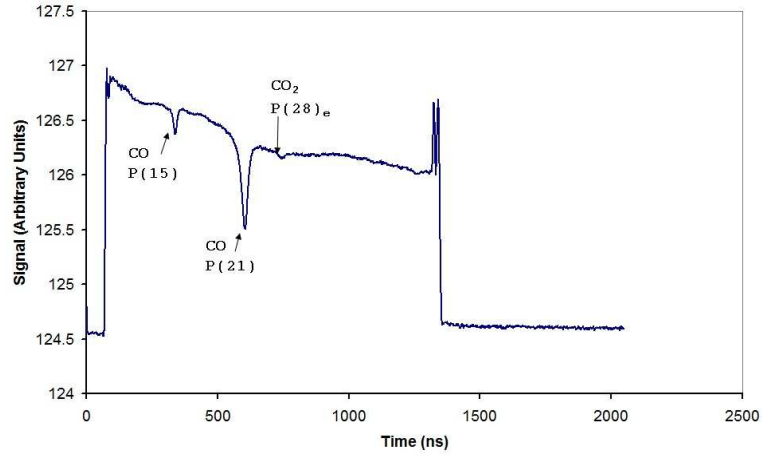


Fig. 3.9: CO and CO_2 lines observed with $4.86\mu m$ laser.

Laser 51 was set to $-18^\circ C$, voltage of 15.5V, repetition rate of 10KHz and a pulse length of 1500ns allowing a 2.5 wavenumber scan starting at $1277cm^{-1}$. With the beam passing through the centre line of the plume the steel block was held in place with standard lab clamps with the aim of recording spectra at measured steps. As the beam was effectively raised through the plume, the burner was mounted on an adjustable platform which allowed it to be raised and lowered. Unfortunately the lab clamps were made of aluminium and the flame temperature was greater than their melting point, melting point of aluminium is $993K/660^\circ C$, resulting in the steel block dropping from its position. It was decided to carry out the measurements without the block in place. Although this was not going to give a sooting flame it should give an idea of different combustion zones.

Characteristic ratios are the equivalence ratios of the fuel to oxidizer and are calculated using equation 3.1,

$$\phi = \frac{\text{fuel} - \text{to} - \text{oxidizer ratio}}{(\text{fuel} - \text{to} - \text{oxidizer ratio})_{st}} = \frac{m_{fuel}/m_{ox}}{(m_{fuel}/m_{ox})_{st}} = \frac{n_{fuel}/n_{ox}}{(n_{fuel}/n_{ox})_{st}} \quad (3.1)$$

where m is the mass, n is the number of moles and st refers to stoichiometric conditions, the condition where the reaction is complete i.e. balanced. These conditions are dependent on the fuel used.

Any ratio of less than 1, regardless of fuel used, is referred to being a lean flame and any ratio greater than 1 is a rich flame.

The equivalence ratios of $\phi = 0.9$, lean flame, and $\phi = 1.2$, sooting/rich flame, were used in the experiments. The results of which are plotted in figures 3.10, for $\phi = 0.9$, and 3.11, for $\phi = 1.2$. In order to make each spectrum clearly visible they have been adjusted so that the lowest spectrum corresponds to the beam just passing over the burner, height of 0mm. It follows that the uppermost spectrum is the maximum height above the burner.

From the graphs unburnt methane is visible as well as a strong water line. The methane lines are three of the $P(5)$ components at 1275.04cm^{-1} $P(5)_{f_1}$, 1275.39cm^{-1} $P(5)_{e_1}$ and 1276.84cm^{-1} $P(5)_{f_2}$. The water line is 1276.63cm^{-1} $P(16)$, all line identifications were done using the HITRAN database [65].

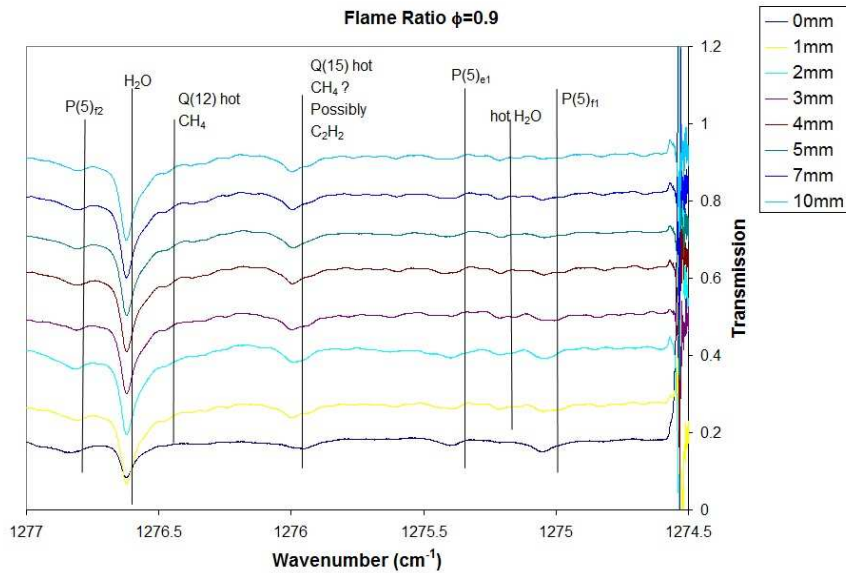


Fig. 3.10: Flame ratio $\phi = 0.9$ adjusted for clarity

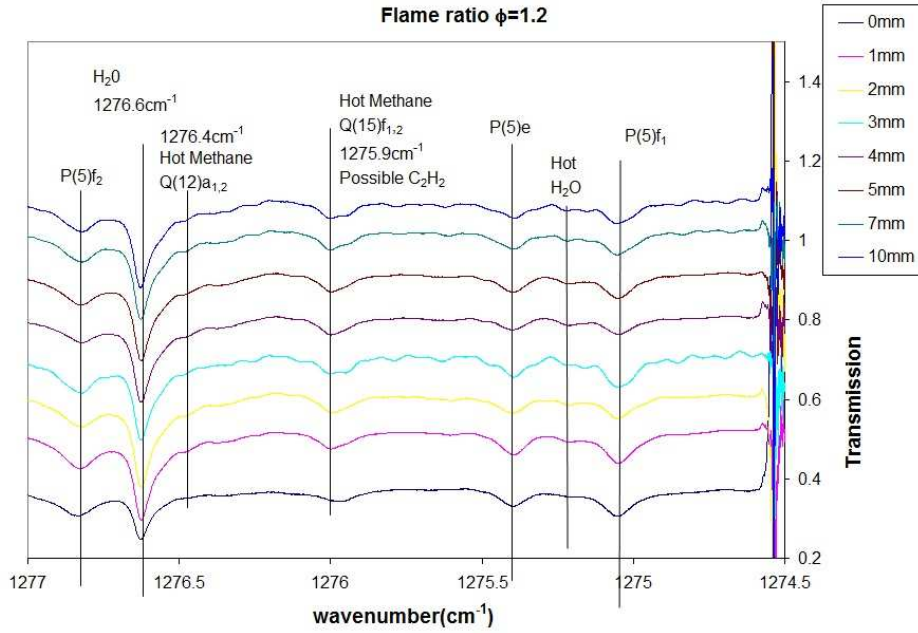


Fig. 3.11: Flame ratio $\phi = 1.2$ adjusted for clarity

As the laser scans up through the plume what would normally be weak transition lines become more prominent indicating an increase in temperature, a graphic example of the Boltzmann distribution changing as the population of states changes. This is visible with the increasing line strength of the CH_4 $Q(15)_f$ line at 1275.95 cm^{-1} . The increasing strength of this line also caused a problem with the possible identification of any C_2H_2 that may have formed as it lies close to the C_2H_2 $4_0^1 5_1^2(\Pi_g - \Pi_u)$ $P(15, e)$ line at 1275.96 cm^{-1} . Acetylene line identification was previously performed by supervisor G. Duxbury and taken from table 2 of [34]. However the lack of a line in the 1275.5 cm^{-1} region lead to the conclusion there is no or very little C_2H_2 forming as the C_2H_2 $4_0^1 5_0^1(\Sigma_u^+ - \Sigma_g^+)$ $P(23)$ at 1275.51 cm^{-1} is a strong transition.

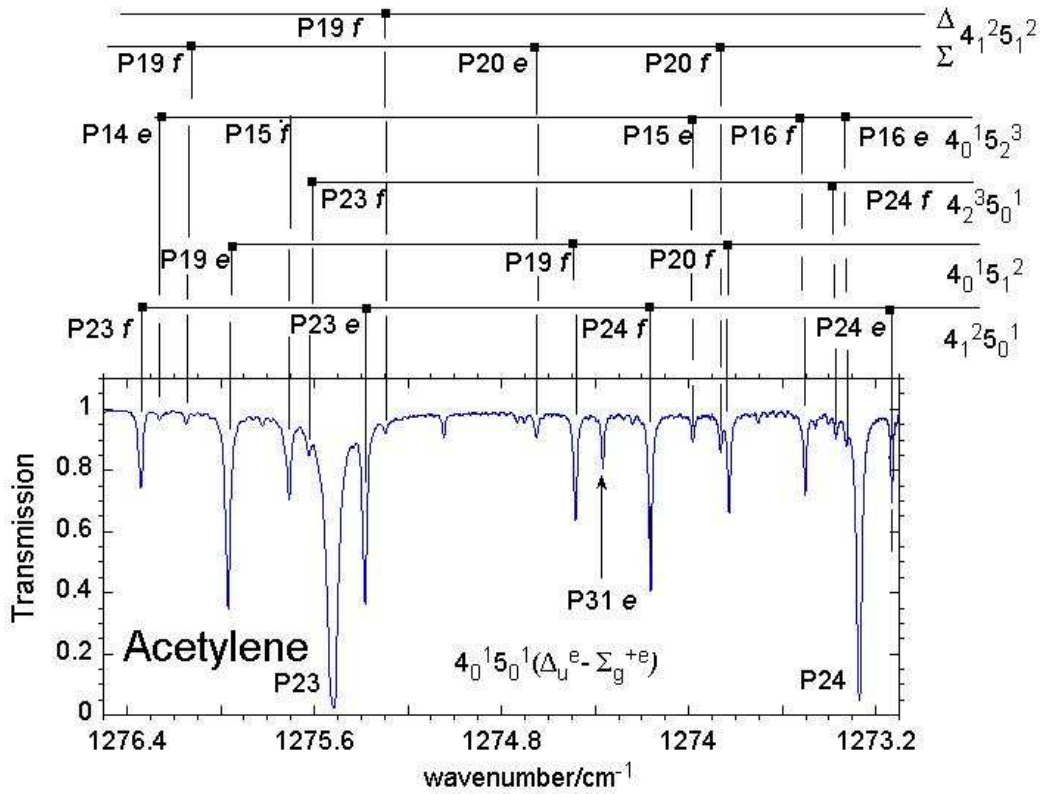


Fig. 3.12: Acetylene spectra, taken from [66](Fig 3a) with permission of G. Duxbury.

With these ambiguous results a return visit was planned, this would allow us to use different parameters settings for the laser, see section 3.4. The $1273 \text{ cm}^{-1} \rightarrow 1274.8 \text{ cm}^{-1}$ region has only weak CH_4 transitions, the strongest being a $^{13}\text{CH}_4$ line at 1274.02 cm^{-1} whereas C_2H_2 has several easily identifiable lines, figure 3.12.

3.4 Ethylene Flame Measurements

The return visit to the Chemical and Process Engineering finally took place in December 2011. This time the fuel gas had been changed to ethylene, C_2H_4 , and a new mounting system for the steel block had been devised. These changes were devised by Dr Burns' group to ensure soot formation. It was originally planned to utilize a retro-reflector in order to have a double pass through the plume, but it was decided that a single pass would give a better indication to the topography of the plume, figure 3.13.

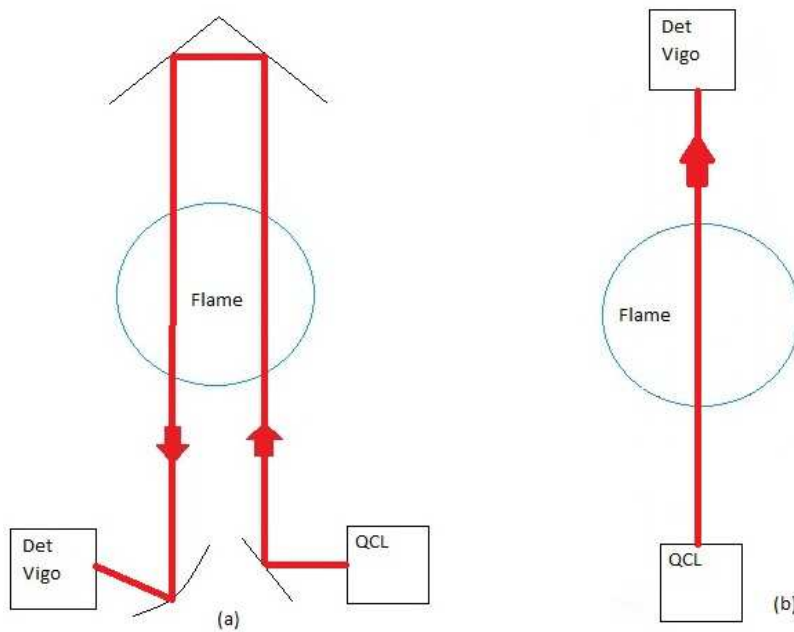
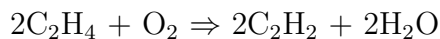


Fig. 3.13: (a) Schematic of beam path using retro reflector. (b) Single pass configuration.

The change in fuel gas turned out to be beneficial for recording the combustion products as ethylene does not have any infrared active fundamental bands in the regions in which the two laser operate [67]. To ensure this was the case some fuel gas was passed through the burner without igniting it, there was no absorption lines visible with either of the lasers used. Therefore any lines visible when the gas was ignited had to be combustion products.

Ethylene can be oxidized to yield acetylene and water,



As the main goal was to look for acetylene the 7.84 μm laser was the first choice, the temperature set to $+15^\circ\text{C}$, voltage of 15.5 V, repetition rate of 10 KHz and pulse length of 1500 ns. These settings had been formulated after the first visit using the long path length Herriott cell within the group laboratory.

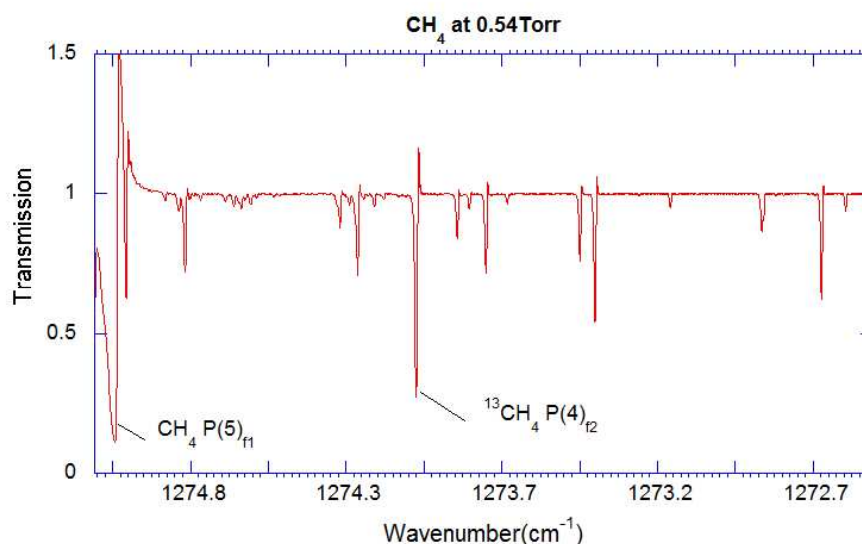


Fig. 3.14: Methane spectra recorded during settings test

Figure 3.14 shows methane recorded during the tests the settings were devised, the only strong methane line is the CH_4 P(5)_{f1} at 1275.04 cm^{-1} at the start of the scan, the next strongest line is the $^{13}\text{CH}_4$ P(4)_{f2} line at 1274.01 cm^{-1} . The ^{13}C isotope line is a factor of 100 weaker than the ^{12}C line at the start of the scan and is only visible in the laboratory experiments due to the 62m path length of the Herriott cell. Importantly the region around 1273.3 cm^{-1} , where the C_2H_2 P(24) $4_0^1 5_0^1 (\Sigma_u^+ - \Sigma_g^+)$ line is has only very weak hot-band/isotope methane lines, so with the laser tuned to this region acetylene would be easily distinguished.

During the experimental runs several lines were clearly distinguishable from baseline fluctuations caused by the refractive index changes in the air near the flame. Unfortunately problems with the $4.86\mu\text{m}$ laser, laser 60, became visible. The baseline developed large oscillations that made it difficult to see any small features, we did however have strong carbon monoxide lines visible and a weaker carbon dioxide line, the same lines visible in figure 3.9.

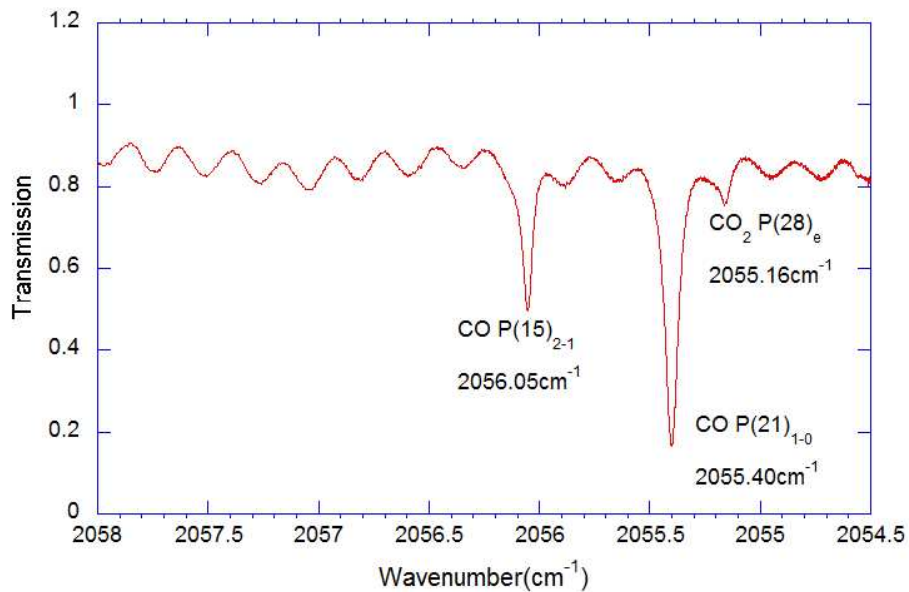


Fig. 3.15: Calibrated spectra of $4.86\mu\text{m}$ laser with the problematic baseline clearly visible

Figure 3.15 shows a calibrated spectrum recorded using laser 60, it shows the baseline oscillations that made it difficult to spot any small features. Fortunately the oscillations did not distort the scan or hinder the line identification. The two strongest lines are Carbon Monoxide with a weaker Carbon Dioxide line visible but distorted due to the baseline oscillations. The strongest CO line is the $\text{P}(21)_{1\rightarrow 0}$ line at 2055.40 cm^{-1} the other is the $\text{P}(15)_{2\rightarrow 1}$ hot-band line at 2056.05 cm^{-1} . Lastly the CO_2 line is the $\text{P}(28)_e$ $1, 1, 1 \rightarrow 0, 0, 0$ at 2055.16 cm^{-1} .

As the laser was giving a distorted baseline the length of time it was in operation was restricted. This meant only three different fuel-oxidizer ratios were used, $\phi = 0.7$ lean flame and $\phi = 1.7, \phi = 2.1$, both rich flames. Figure 3.16 shows the CO P(21) line and the CO₂ P(28)_e for each ratio. It appears that concentration of CO is higher for the lean flame but it may be more likely that the temperature of the leaner flame was higher. The lean flame has higher levels of Oxygen than fuel so it is more likely that there is more CO₂ being formed. The CO₂ line does appear stronger in the lean spectra when compared to the two other ratios. This makes sense as the absorption cross-section for CO₂ gets weaker in this region as the temperature of the gas increases and for CO it gets stronger.

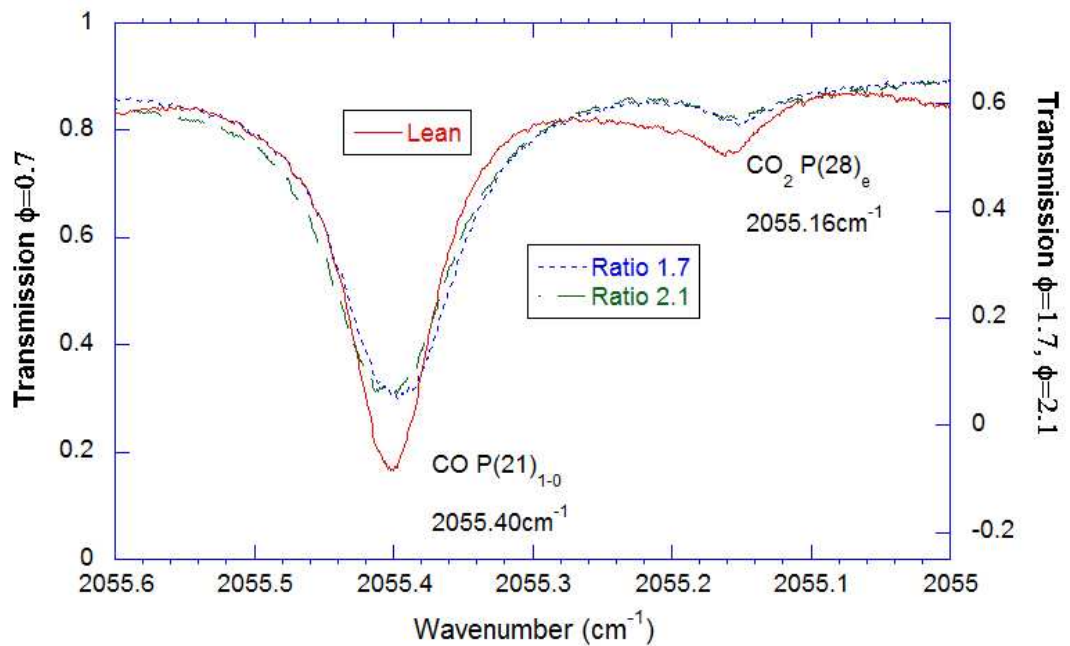


Fig. 3.16: Carbon Monoxide P(21) and Carbon Dioxide P(28)_e lines at three fuel-oxidizer ratios

The cause of the problems with the laser were not immediately apparent and further investigation will be required before it can be used again. This is essential as it is possible that the mounting of the laser in the developer head may need adjustment. Successive heating and cooling of the device can cause the mounting to become loosened and improper electrical connection occur. This can result in the device failing, so for the prolonged use of the device some maintenance is required.

As it was hoped that acetylene would be found the focus was on the use of laser 51 with the setting previously mentioned. When performing the experiments three lines were clearly visible at the end of the chirp. This was encouraging, as this is the region of the scan that had been chosen for the acetylene lines to be apparent. It also showed that no methane was being formed in the combustion process as there was no absorption line at the beginning of the chirp as in figure 3.14.

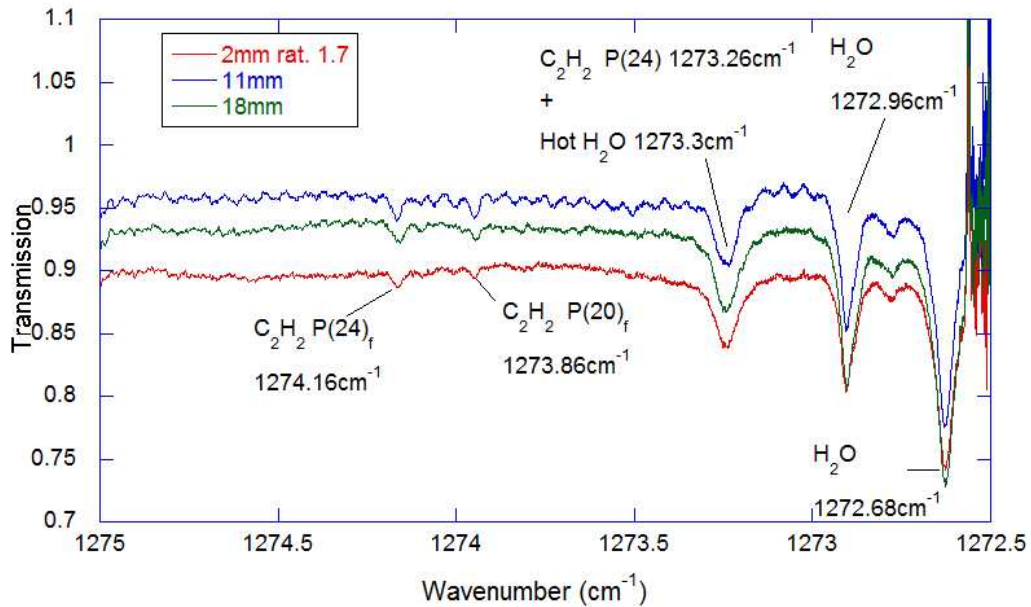


Fig. 3.17: Calibrated spectra, flame ratio $\phi = 1.7$, using predetermined laser settings

Figure 3.17 show the calibrated spectrum recorded using the $+15^{\circ}\text{C}$ temperature settings, these tuned the laser to chirp from 1275cm^{-1} to 1272.5cm^{-1} , with the equivalence ratio of $\phi = 1.7$. Only three heights above the burner are shown (2mm, 11mm and 18mm). This is for clarity as spectra were recorded for each millimeter above the burner. In this region it was expected that the acetylene P(24) $4_0^1 5_0^1(\Sigma_u^+ - \Sigma_g^+)$ line at 1273.26 cm^{-1} would be the dominant feature, however there were two other strong features visible as the run was performed. It wasn't until analyzing the spectra that it was realized that these were actually water absorption lines. Although there is a window in the water absorption lines at room temperature in the scan range of the laser this changes as the temperature increases. Figure 3.18 shows the difference of water absorption lines at room temperature and at 1000K, this figure was constructed using data from the HITRAN database for the room temperature lines [65] and the HITEMP database for the 1000K lines [68]. This turned out to be fortunate for the calibration of the spectra as these gave points to base the calibrations on. The calibration of the spectra from the time domain they are recorded in to the spectral domain relies on the ability to identify specific absorption lines of known species within the chirp range of the laser used, the chirp range for various laser temperature setting having been predetermined by using a Fourier Transform Infrared Spectrometer (FTIR) to characterize the laser.

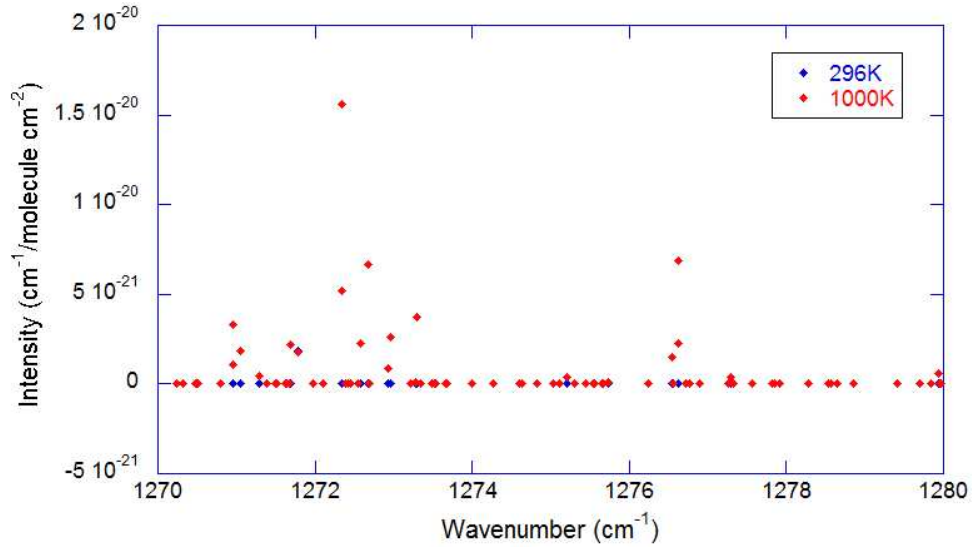


Fig. 3.18: Plotted HITRAN/ HITEMP data for water covering the region where the $7.84\mu\text{m}$ laser operates, blue points refer to room temperature, red points to temperature of 1000K

It was during the initial analysis that it became apparent that the acetylene wavenumber assignments done by G. Duxbury for the work on the plasma reactor [66] did not cover the regions the laser was tuned to for the experimental runs. Table 3.2 is a reproduction of table II in [66], it covers the region 1273.1cm^{-1} to 1276.5cm^{-1} , whereas the laser was tuned between 1272.6cm^{-1} to 1277.9cm^{-1} . The lower wavenumber range did not cause any problem as the chirp of the laser started at 1275cm^{-1} and any lines in this region were listed. It was as the laser was tuned to chirp from 1277.9cm^{-1} to 1275.8cm^{-1} where only weaker acetylene lines were at the end of the chirp. It was decided to use the lab Herriott cell to record a spectrum in this region, see figure 3.19 (a full analysis of the lines in the 1276.5cm^{-1} to 1277.9cm^{-1} region has still to be performed).

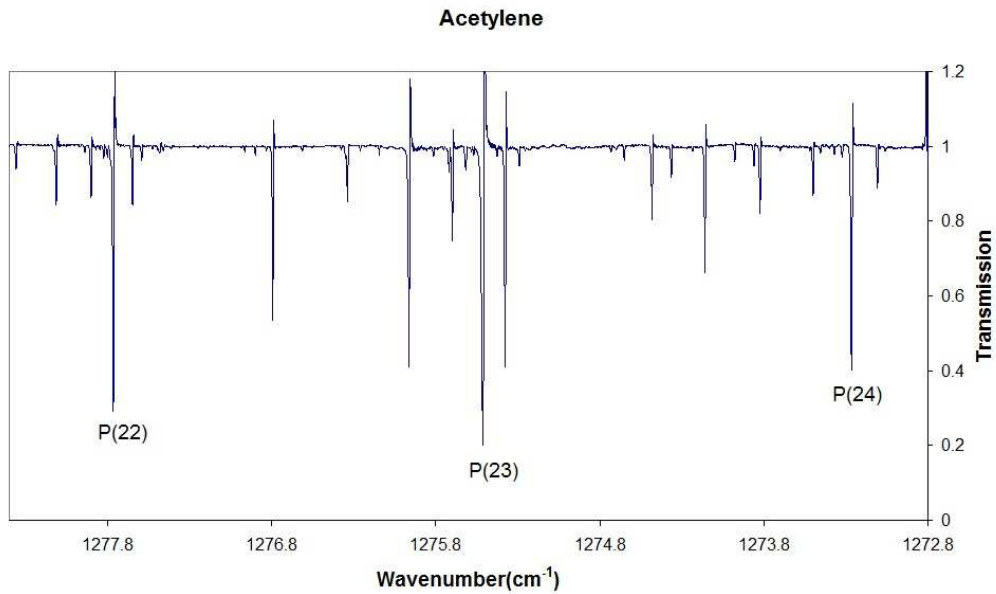
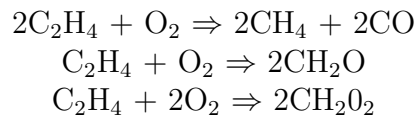


Fig. 3.19: Spectra of acetylene recorded in the lab at Strathclyde University.

It soon became apparent after calibrating the spectra in the 1274.5 cm^{-1} to 1278 cm^{-1} region, laser temperatures of -15°C to -25°C , that many of the observable features did not match acetylene absorption lines. The $P(16)$ water line at 1276.63 cm^{-1} was clearly visible and gave a good starting point for calibration of the spectra and for identification of other features. With the fuel gas being ethylene there are several possible combustion products. Among these are methane (CH_4), formaldehyde (CH_2O) and formic acid (CH_2O_2), these can form by oxidation of ethylene, e.g.



Further oxidation of these products give rise to the water, carbon monoxide and carbon dioxide found by both lasers used.

Figure 3.20 shows an absorption spectrum of the start of one of the flame measurements overlaid with data for C_2H_2 at 500K taken from the HITRAN 'on the web' resource [71].

Wavenumber (cm^{-1}) ^{a,b}	E''^a (cm^{-1})	Vibrational transition	spin weighting	Rotational transition ^b
1276.33663	1262	$4_1^2 5_0^1(\Pi_u - \Pi_g)$	1	P(23,f)
1276.25806	1708	$4_0^1 5_2^3(\Sigma_u - \Sigma_g)$	1	P(14,e)
1276.14079	1775	$4_1^2 5_1^2(\Sigma_g - \Sigma_u)$	1	P(19,f)
1275.95859	1177	$4_0^1 5_1^2(\Pi_g - \Pi_u)$	3	P(19,e)
1275.71661	1743	$4_0^1 5_2^3(\Delta_u - \Delta_g)$	1	P(15,f)
1275.61495	1881	$4_2^3 5_0^1(\Delta_u - \Delta_g)$	1	P(23,f)
1275.58094	1881	$4_2^3 5_0^1(\Delta_u - \Delta_g)$	3	P(23,e)
1275.56659	1743	$4_0^1 5_2^3(\Delta_u - \Delta_g)$	3	P(15,e)
1275.51222	649	$4_0^1 5_0^1(\Sigma_u^+ - \Sigma_g^+)$	3	P(23)
1275.42325	1792	$4_1^2 5_1^2(\Delta_g - \Delta_u)$	3	P(19,e)
1275.37466	1262	$4_1^2 5_0^1(\Pi_u - \Pi_g)$	3	P(23,e)
1275.28862	1792	$4_1^2 5_1^2(\Delta_g - \Delta_u)$	1	P(19,f)
1274.64740	1822	$4_1^2 5_1^2(\Sigma_g - \Sigma_u)$	3	P(20,f)
1274.47950	1177	$4_0^1 5_1^2(\Pi_g - \Pi_u)$	1	P(19,f)
1274.36203	1167	$4_0^1 5_0^1(\Delta_u^e - \Sigma_g^{+e})$	3	P(31,e) ^c
1274.15639	1318	$4_1^2 5_0^1(\Pi_u - \Pi_g)$	3	P(24,f)
1273.97456	1732	$4_0^1 5_2^3(\Sigma_u - \Sigma_g)$	3	P(15,e)
1273.85701	1822	$4_1^2 5_1^2(\Sigma_g - \Sigma_u)$	3	P(20,f)
1273.81972	1225	$4_0^1 5_1^2(\Pi_g - \Pi_u)$	1	P(20,f)
1273.51679	1781	$4_0^1 5_2^3(\Delta_u - \Delta_g)$	3	P(16,f)
1273.45272	1995	$4_2^3 5_0^1(\Sigma_u^+ - \Sigma_g^+)$	3	P(25,e)
1273.36660	1937	$4_2^3 5_0^1(\Delta_u - \Delta_g)$	3	P(24,f)
1273.31971	1781	$4_0^1 5_2^3(\Delta_u - \Delta_g)$	1	P(16,e)
1273.26195	706	$4_0^1 5_0^1(\Sigma_u^+ - \Sigma_g^+)$	1	P(24)
1273.10387	1319	$4_1^2 5_0^1(\Pi_u - \Pi_g)$	1	P(24,e)

^aApproximated using values of rotational constants and band origins in [69]

^be and f indicate the l -doubling components of the Π and Δ vibrational states.

^cTransition is due to rotational l -resonances between Δ_u^e and Σ_u^{+e} sub levels of the same J value, see [70]

Tab. 3.2: Acetylene wavenumber, assignments and ground state term values for figure 3.6 taken from [66] with permission of G. Duxbury.

The spectrum was recorded with the beam passing through the centre of

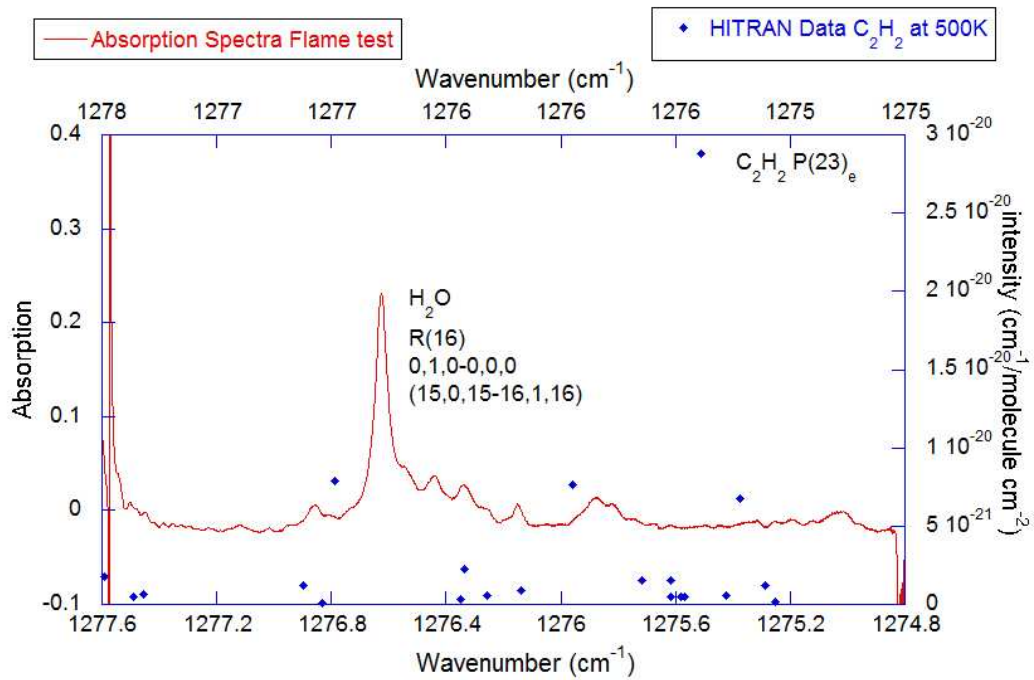


Fig. 3.20: Absorption spectra recorded at the beginning of flame test, red trace, with overlay of HITRAN data for C₂H₂ at 500K.

the flame at a height of 10mm above the burner. In this test it was hoped to see how the the topography of the flame changes as the beam 'moved' horizontally through the flame. In reality the burner was moved so that the alignment of the beam was not disturbed. The water line is clearly visible however when comparing the C₂H₂ data with the recorded spectrum it is obvious that there is no match. It may be that the temperature of flame was in the order of 2000K and the C₂H₂ data was for gas at 500K but this is unlikely as the strong P(23)_e would still be visible. J=23 is sufficiently far from the band centre such that changes in the Boltzmann distribution would not affect the intensity of the absorption. It is possible that there are low levels of C₂H₂ present but the combination of pressure, atmospheric pressure, and temperature are masking any absorption features.

The availability of data for molecular gases at high temperature is only now becoming more common with the introduction of the HITEMP database and the HITRAN 'on the web' database. Whilst these provide a useful ser-

vice the gases sampled and the temperature ranges covered are still limited. It is possible that the features observed in the flame spectra may be associated with the various possible combustion products but there is also the chance that some of the features may be due to absorbers in the lab atmosphere. The best course of action would be to repeat some of the experiments using the $7.84\mu\text{m}$ laser with a beam-splitter in situ in order to have a reference beam recording the atmosphere away from the flame, this would ensure differentiation of features.

Although only some of the spectral lines have been identified work continues in an attempt to identify the other features.

3.5 Beam Reflection From Non-Mirrored Surface

The group had previously done work in collaboration with the aerospace division of Rolls Royce making measurements on the exhausts of a turbo-jet engine at their test facility in Ansty [35] [29]. In September 2011 Dr John Black from Rolls Royce contacted the group again with the question 'Can a QC laser be used to make measurements of the combustion processes inside a jet engine, i.e. a flight sensor for combustion processes as part of the control system.'. To answer this it was required to find out how the beam would be reflected back out from inside the engine as it would not be possible to have the beam passing through the engine.

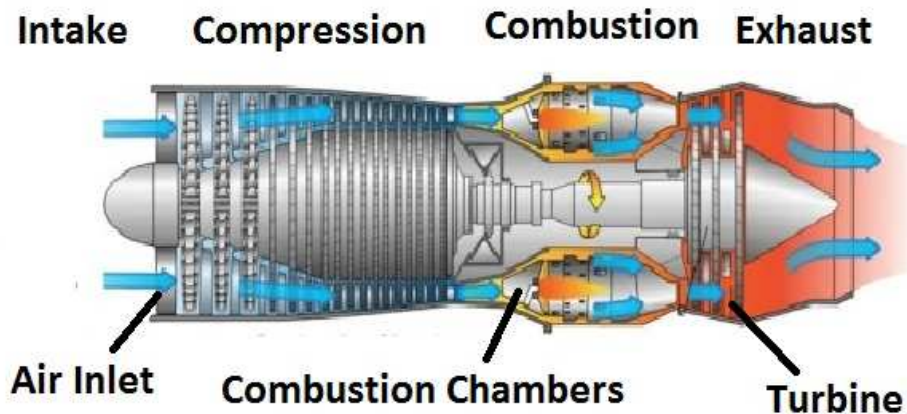


Fig. 3.21: Schematic of a typical turbojet engine for illustration purpose only (taken from http://gtae6343.wikia.com/wiki/File:Turbojet_engine.jpg).

The area within the engine the measurements were to be made would be the equivalent of the turbine zone shown in figure 3.21. The only way to have the beam return from this zone would be if it could be reflected off the turbine blades and if the reflected beam has sufficient power to give a spectrum.

For this we received a section of turbine blade, a high pressure nozzle guide made of a nickel alloy, from an engine that had been previously run at full power. This would give a more realistic surface to test its reflectivity as a new part would not have been exposed to the heat and pressure of combustion. The surface of the individual blades appeared to have a different coating on each side. One side had a smooth white coating that seemed to be the best bet on having the beam reflect back. Unfortunately the curvature on this side, it had the form of a mathematical saddle-point, meant the direction of the reflected beam was difficult to determine and the beam too dispersive to be of a usable power. The other side had a rough coating with the appearance of an anti corrosion phosphor coating. The coating was a thermal barrier coating, and after some discussion it was realized that this would be the surface facing the outer shell of the engine and therefore would be the surface tested.

The engine part was mounted at the end of the optical table that holds the two laser spectrometer in the lab. With the temporary addition of two extra mirrors and a second detector we were able to redirect the QC laser beam and the red alignment laser to fall onto the test surface, as the infrared beam is set to co-propagate with the red beam it indicated where it was incident on the surface, see Figure 3.22.

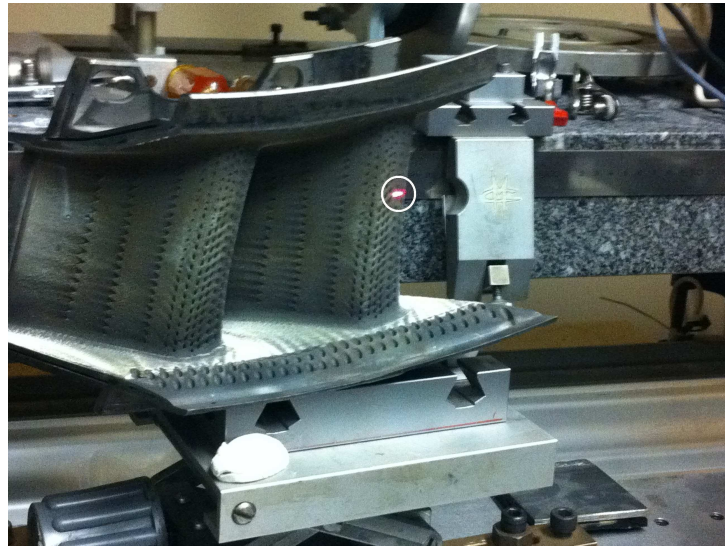


Fig. 3.22: Jet engine component. The red spot (circled) marks the point where the infrared beam is striking.

At first the signal detected was too weak for it to give any real information but even though it was weak it was encouraging to get any sort of signal returned. In order to improve the signal a zinc selenide lens was placed in front of the detector. This greatly improved the detected signal to the extent that, although noisy, it was possible to determine two water absorption lines from atmospheric water vapour in the lab. The laser used was the 7.46 μm laser (laser 64) set to a temperature of 10°C, repetition rate of 10 kHz, pulse length of 1500 ns and a voltage of 11 V.

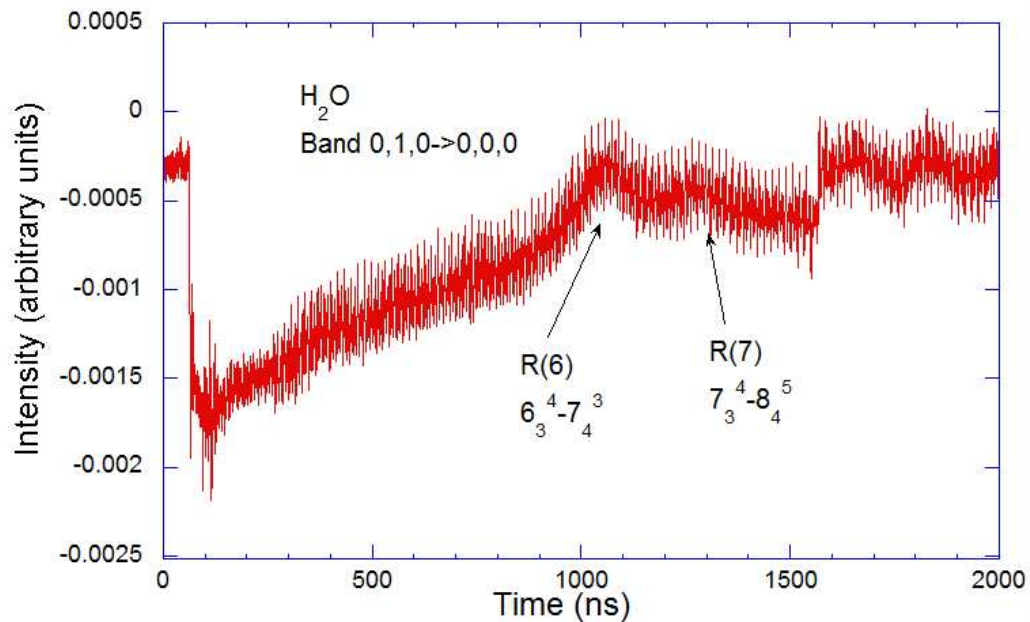


Fig. 3.23: Spectra of atmospheric water after reflection off jet engine component.

Although we were able to obtain a detectable signal and see atmospheric water vapour, figure 3.23, the practicalities of making measurements in this region of the engine ruled out the use of QC lasers. In the combustion and turbine zones of jet engines the pressure ranges from 190 Torr up to $\approx 25,500$ Torr, the lower pressure when the engine is starting and the higher when running.

As the aim was for measurements when running pressure broadening alone would cause any absorption feature to lose all structure, also the rotational speed of the turbine, in order of 30,000 revolutions per minute, would reduce to signal reflected.

Even though no further work came from these tests it was an interesting exercise in determining what kind of surface can reflect a QC laser with enough return power that usable spectra can be obtained.

3.6 Conclusion

As a portable device the 4C-PQCLAS has proven itself as a reliable way to monitor both trace gases in the atmosphere and exhaust gases from combustion in real time. However the choice of laser wavelengths fitted into the spectrometer limits the gases detected, for example to monitor Sulfur Dioxide would require one of the existing lasers to be swapped over. The newer spectrometers made by Cascade Technologies can be supplied with a choice of lasers depending of the customers requirements. Regardless of the laser used the control software can only focus on a single species meaning some post analysis of the data is needed as other gases can be detected, for example the N₂O laser has a central wavelength of 7.84 μm and also detects H₂CO and CH₄ if present.

When used to measure the exhaust gases of motor vehicles, in this case buses, the 4C-QCLAS has displayed a greater level of detection than current equipment used for MOT emission testing. As previously mentioned the Bosch BEA series has detection limits typical to most equipment used for emission testing with a detection limit of parts per million, whereas the 4C-PQCLAS has detection a limit in the order of parts per billion. Other benefits of the QCL based system is the high speed detection of changes in concentration and the ability to identify, through post analysis, which hydrocarbon is present in the exhaust gases. Accurate calibration of the 4C-PQCLAS would be required if it was to used in a comparison test with currently available MOT emission testing equipment to verify instrument performance. However the cost of a multi-species laser absorption spectrometer far exceeds that of garage base testing equipment, in the order of 10 times as much.

Although the developer head system is designed for laboratory use its modular nature means it can be transported easily and quickly set up to measure gaseous species in a variety of locations. The system used for the flame measurements and the Oxford experiments has previously been used for in-flight measurements [6] and jet engine exhaust measurements [35] as well as the acetylene measurements done in Bristol university [66]. The Developer head itself provides the true flexibility in the system as different laser devices can be fitted depending on the gas being experimented upon.

The pressures inside a modern turbojet engine would make it impossible to obtain a spectrum of the combustion processes as they happen. The results from the experimental work using the non-mirrored surface could become an interesting prospect. It may become possible to make direct measurements of either combustion processes or products (exhaust plumes) without highly polished mirrored surfaces being required to reflect beams.

This ease of set-up made it the perfect option for the flame measurements. Even though the path length through the flame was only 3 cm a difference in CO concentrations between gas mix ratios was clear when using the 4.86 μm laser (laser 60). The unambiguous results of possible combustion products in the 8 μm region was due to the absorption lines being pressure broadened to such an extent they were indistinguishable from the fluctuating baseline. This and the lack of availability of high temperature absorption data of these species made identification of spectral lines difficult. However it may still be possible to map the plume as high temperature data on water, carbon monoxide and carbon dioxide has recently become available. Unfortunately it was found that the 4.86 μm laser was in the first stages of failing. It was hoped that the oscillations on the baseline was due to a loose connection within the developer head. However after swapping into a different head the device gave the same oscillations on the baseline. Any further experiments on CO would require a new device operating in the same optical region.

4. COLLISIONAL DAMPING OF RAPID PASSAGE SIGNALS

4.1 *Introduction*

In this chapter all experiments performed at Oxford University were carried out in collaboration with J.P. Van Helden. Experiments performed within Strathclyde University were done by the author of this thesis with supervisor Professor Geoff Duxbury.

Section 4.2 covers a trip to Oxford University's Physical and Theoretical Chemistry Department where the 5.25 μm laser was used in conjunction with a tunable CW laser operating in the same region to perform a pump-probe experiment on the open shell molecule nitric oxide. The aim of the visit was to use the pulsed QCL to excite the system into an upper state then use the CW-QCL to excite the overtones. When this is done the spin of the uncoupled electron Λ -doubling causes the hyperfine components to become visible on the detector signal of the CW laser. Collisional damping experiments on nitric oxide mixing with helium and then with krypton were also performed using the pulsed laser.

Section 4.3 covers experiments carried out in the laboratory at the University of Strathclyde on species responsible for changes in Earth's atmospheric conditions, for example Global Warming and Ozone Depletion. It also covers repeats of collisional damping of nitric oxide performed at Oxford University. All experiments were performed using the twin laser spectrometer described in subsection 2.2.2. The process of adding either inert gases or gases that absorb at different wavelengths to the gas being studied reduces the non-linear effects caused by the rapid frequency sweep of the laser.

By removing the rapid passage spikes the absorption line-shapes adopt a more Gaussian profile and can then be used to calculate concentrations using the Beer-Lambert Law, equation 2.36. It may be possible to use these rapid passage signal to gain information about the processes involved in the excitation and relaxation of the system. The rapid passage signals are indicative of stimulated emission. While the free induction decay signals could be studied to determine how the system relaxes as the rapidly changing laser frequency interacts with this relaxation. Although this would be an interesting project it does not fall into the remit of this thesis.

Section 4.4 covers dimerization of nitrogen dioxide and the detection of the dimer in the 8 μm region. The detection of the dimerization of NO_2 was an unexpected find whilst exploring collision partners on other species. Also included is evidence of the continued existence of the dimer when the sample is buffered with dry nitrogen, this give evidence that detection of NO_2 by commercial spectrometers may give incorrect concentrations.

Section 4.5 covers the effect on line-shape on $^{14}\text{NH}_3$ and $^{15}\text{NH}_3$ when using a new power supply in conjunction with a QC laser with a slower chirp rate. The slow chirp rate gives a more symmetric line-shape and the new power supply electronics have a more stable output current should result in better spectra. There is also very little data on the line positions of $^{15}\text{NH}_3$ in the 6.15 μm region. By temperature tuning the laser from -30°C through to $+45^\circ\text{C}$, this should give a combined spectral window $\Delta\nu \approx 6 \text{ cm}^{-1}$ where the identification on previously unidentified absorption lines can be done.

4.2 Nitric Oxide Pump-Probe Experiment at Oxford University

In September 2010 the group invited to the Chemistry Department at Oxford University by the group headed by Dr Grant Ritchie. The purpose of the visit was to explore the hyperfine features that arise from the open shell nature of Nitric Oxide (NO), there is an unpaired electron which give rise to the sub-Doppler features as well as a large dipole moment. In order to observe this the gas has to be aligned, i.e. the molecules have their dipole moments pointing in the same direction. To do this the sample has to be either in a Stark field where the dipole moments of the molecules are aligned with the electric field between 2 metal plates or by using a continuous wave (CW) laser ramping through the frequency of the absorption line of interest, here the dipole moments align with the polarization of the laser. By using a pump the fundamentals are excited into their upper level, then the probe is used to excite hot bands or split hyper-fine components. This is normally done by splitting the beam into two with a beam splitter, one beam goes into the gas cell the other is delayed before passing through the cell before hitting the detector.

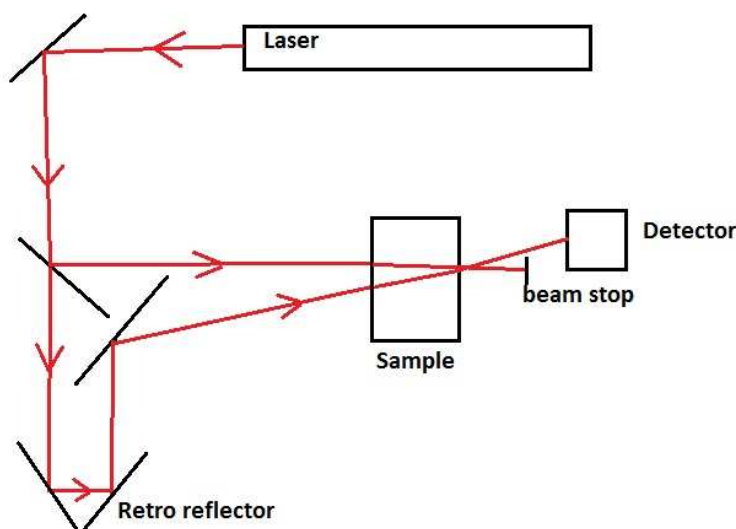


Fig. 4.1: Schematic of pump-probe spectroscopy

The Oxford group have used an external cavity tuned CW-QCL, a Daylight Solutions CW-MHF centered at $5.35\mu\text{m}$, to make sub-Doppler Lamb-dip measurements [72] on nitric oxide namely the Λ doublets of $v=0$, $J=13.5$ of the ${}^2\Pi_{\frac{1}{2}}$ state on the R(13.5) transition. With the success of these experiments the idea was formulated to use a pulsed QC laser to pump the gas and use a ramped CW laser to probe the gas. For this they required a pulsed laser that could scan through the same doublet. One of the lasers owned by the group has a wavelength centered at $5.25\mu\text{m}$ and can be tuned from 1900 cm^{-1} to 1907 cm^{-1} allowing the detection of 3 sets of Λ doublets and the associated singlets. The Daylight system has a reported scan range of 60cm^{-1} .

The Λ doubling in the ${}^2\Pi$ state occurs due to its rotational levels being perturbed by the rotational levels of a ${}^2\Sigma$ state. Λ -type doubling is similar to l -type doubling, in that the double degeneracy of the perpendicular vibrations of polyatomic molecules (l -type) is comparable to the double degeneracy of the electronic states of diatomic molecules, however the uncoupled electrons' angular momentum has to be taken into account. The hyperfine components are a manifestation of the interaction of the electron spin, the electron orbital angular momentum and the molecular angular momentum. The double degeneracy of the Π state is removed with increasing rotations of the molecule due to the interactions of the rotation and electronic motion [73].

Throughout sections 4.2, 4.3 and parts of 4.4 where nitric oxide is discussed the convention is to use the terms singlet and doublets when describing the absorption features. It should be noted that absorption features associated with transitions are all doublets due to l -type doubling. It is the case that the ${}^2\Pi_{\frac{3}{2}}$ transitions are not resolved as the separation of the lines is less than the Doppler limit. Conversely the separation of the ${}^2\Pi_{\frac{1}{2}}$ features is resolved at the Doppler limit. The result of this is that the ${}^2\Pi_{\frac{3}{2}}$ transitions appear to be a single line and thus described as a singlet.

4.2.1 White Cell Collisional Experiments

To make full use of the limited time the $5.25\mu\text{m}$ pulsed laser would be available to the Oxford group the initial plan was to perform some collisional dampening experiments with Nitric Oxide using Helium and Krypton as buffer gases that had previously been performed using their CW laser. A modified White cell [32] was used for these experimental runs, instead of the reflected beams lying in the same plane they cross over and result in a longer path length. The White cell used had a path length of 20m.

As little work had been done using the laser at Strathclyde, some test runs were performed, prior to the visit, to ensure that the lines tuned to were properly identified. The laser tuning range allowed the detection of 3 sets of doublets and singlets, see figure 4.2.

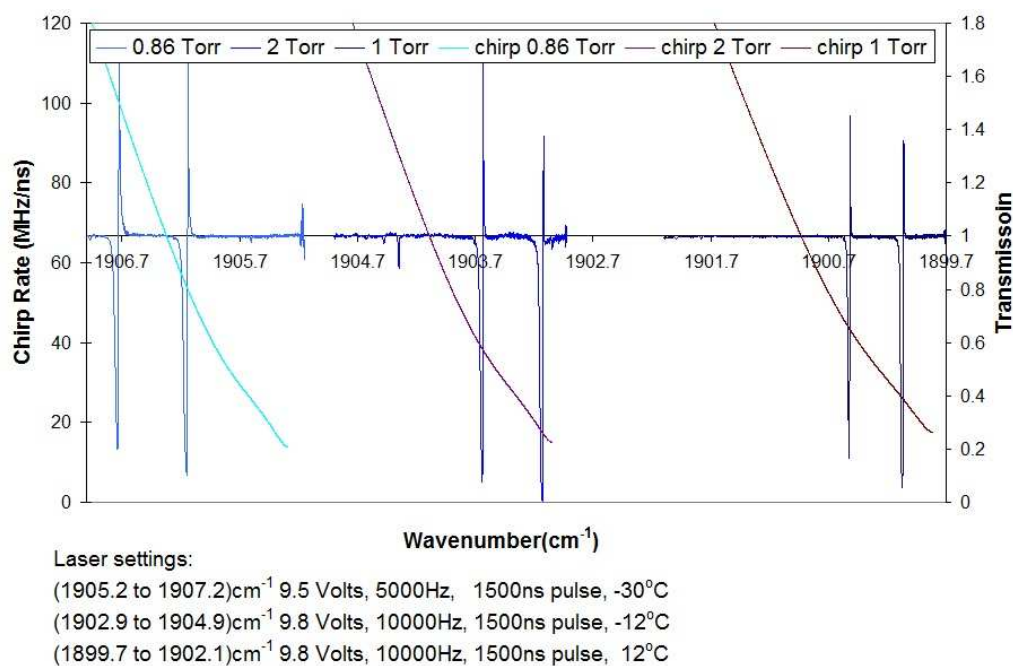


Fig. 4.2: Laser tuning tests, NO recorded with $5\mu\text{m}$ laser

In figure 4.2, the calculated chirp rates are indicated. This is the rate at which the laser frequency is changing as the applied pulse progresses in time. As the chirp rate has an effect on the shape of the absorption line and resolution of the recorded spectra [74] [75], the resolution increases with slower chirp rates. With this in mind, fine tuning of the scan range can be done by slightly adjusting the laser temperature settings.

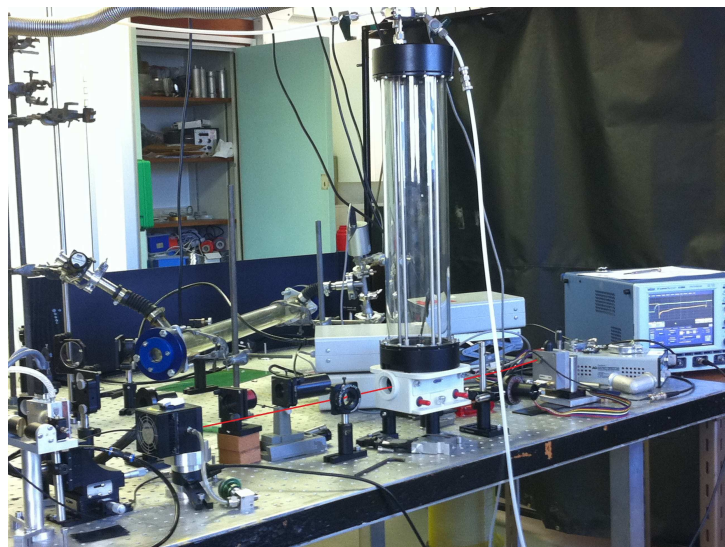


Fig. 4.3: White cell in Oxford University lab, laser path into cell and out to detector indicated in red.

As the cell was vertically mounted some problems were encountered attaching the gas fill, vacuum line and manometer. There were only two narrow connectors, each a $\frac{1}{4}$ inch Swagelok connection, restricting to only one manometer. For initial tests a 0 to 1 Torr manometer was chosen, unfortunately pressures below 20 mTorr could not be accurately recorded due to meter limits. In these tests a small amount of gas was let into the cell and the pressure reduced in steps in order to observe when the rapid passage signal was negligible. The absorption features became sharper and the rapid passage signals were minimized. It was during these test runs that there appeared to be a second prominent rapid passage spike (Figure 4.4).

The Baseline noise was attributed to the oscilloscope used, a LeCroy WaveRunner 6100A, to record the spectra only 1000 individual scans were averaged whereas the ACQiris digitizer performs 8000 averages.

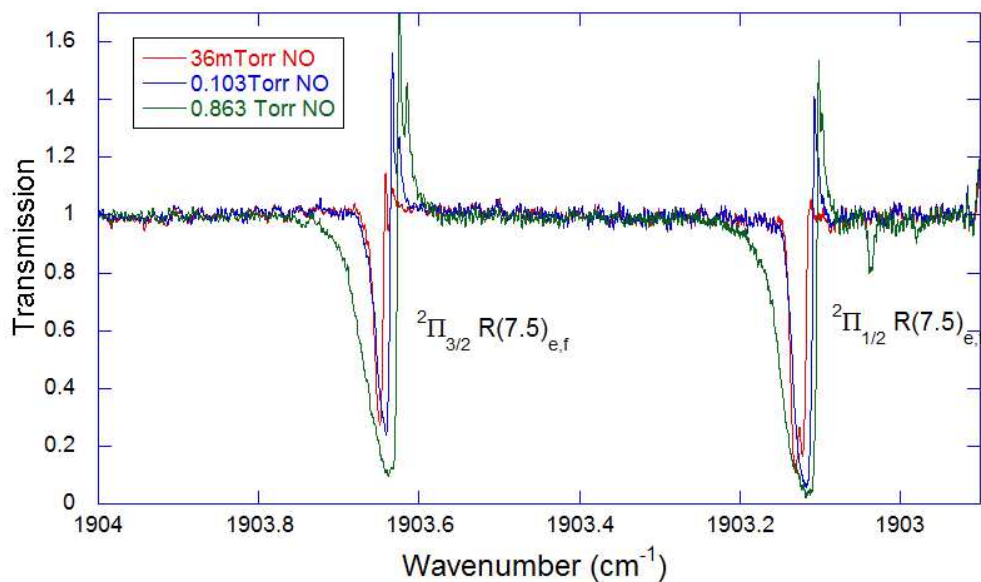


Fig. 4.4: Nitric Oxide R(7.5) singlet and doublet lines.

Figures 4.4, 4.5 and 4.6 were recorded with the laser operating at -13.5°C . This temperature setting positioned the absorption lines near the end of the chirp, the singlets chirp rate being 39.4 MHz/ns and the doublets chirp rate being 18.3 MHz/ns . With the laser frequency changing at these rates the resolution of the singlet would be *ca.* $\Delta\nu = 0.0066\text{ cm}^{-1}$ and of the doublet *ca.* $\Delta\nu = 0.0045\text{ cm}^{-1}$

For comparison figures 4.7 and 4.8 show the same lines featured in figures 4.5 and 4.6 with the laser tuned so they are mid-chirp. At this point the resolution of the singlet is *ca.* $\Delta\nu = 0.0090\text{ cm}^{-1}$ and the doublet is approximately at the same position of the chirp as the singlet when the laser temperature was set to -13.4°C with the resolution *ca.* $\Delta\nu = 0.0067\text{ cm}^{-1}$. It is clear to see that even a small change in the laser temperature can result in noticeable changes in the resolution of the system. This variation of chirp rate also has a visible effect on the rapid passage spikes with the spike more pronounced on lines where the chirp rate is fastest.

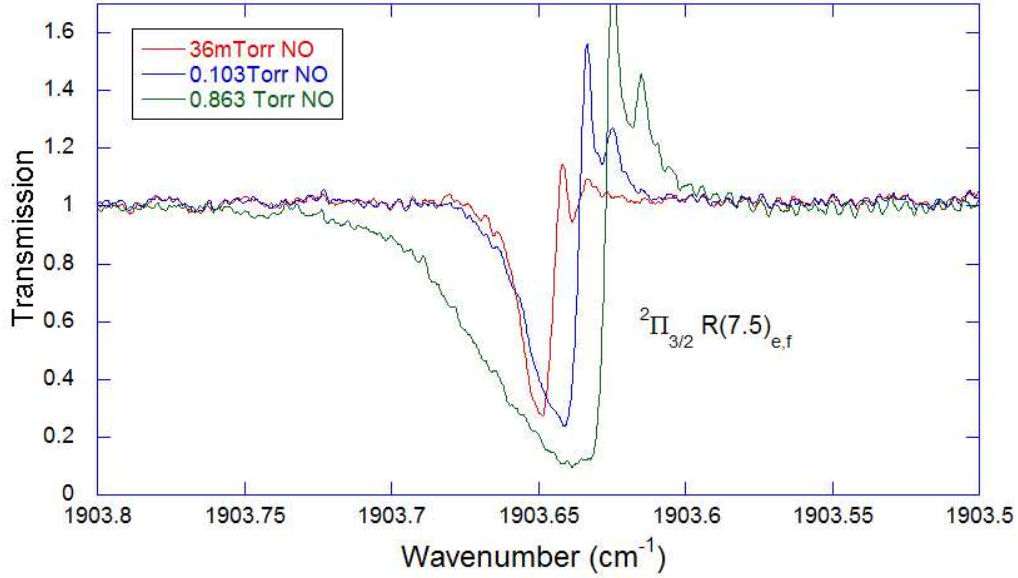


Fig. 4.5: NO R(7.5) $^2\Pi_{3/2}$ singlet

At first the splitting in the rapid passage signals was believed to be connected to the doublet nature of the absorption lines, the singlet lines are actually unresolved doublets, the R(7.5) $^2\Pi_{3/2}$ 'singlet' has a maximum separation of 0.0014cm^{-1} between its component lines, where both the HITRAN database and the NIST Wavenumber Calibration Tables [76] give this approximation. Normally the system would not be able to achieve this resolution, even with the singlet at the slowest chirp rate of 16MHz/ns ($\Delta\nu=0.00417\text{cm}^{-1}$). However the asymmetry and distortion of the line shapes due fast frequency chirp seemed a plausible explanation to why double rapid passage spikes were visible. In addition the oscilloscope used had a faster sample rate, 5 Giga samples per second (0.2 nanoseconds per data point) and bandwidth of 1GHz where the ACQiris card samples at 2 giga samples per second (0.5 nanoseconds per data point) with bandwidth of 500MHz.

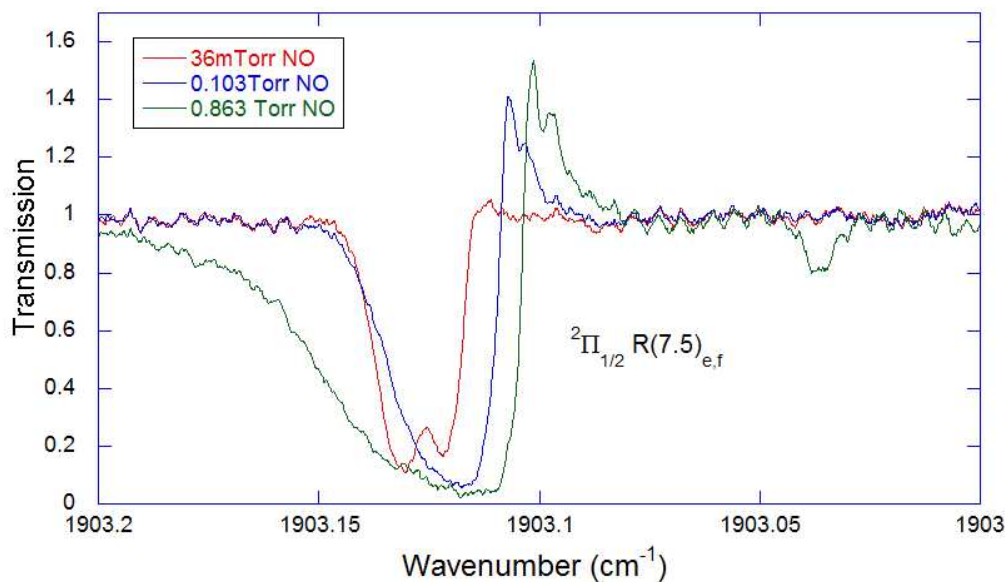


Fig. 4.6: NO R(7.5) ${}^2\Pi_{1/2}$ doublet

The polarization of the pulsed laser was also checked to see if this gave a reason for the strange behavior of the rapid passage signals. A polarizer placed in front of the laser confirmed that the beam entering the White cell had the horizontal polarization as expected. Then the polarizer was placed between the cell and the detector. This only resulted in a reduction of laser power reaching the detector. After some testing it was concluded that the cell was partially de-polarizing the beam so the beam had circular polarization.

It was decided to carry on with the collisional experiments with the cell as it was. As helium is the lightest mono-atomic element it is often used for leak detection, its small size and unreactive nature also makes it ideal for collisional damping experiments. Krypton being larger than helium, helium has a Bohr radius of 31pm and krypton has a Bohr radius of 88pm, has a different effect as a collision partner but as it is also a noble gas interactions are purely kinetic in nature.

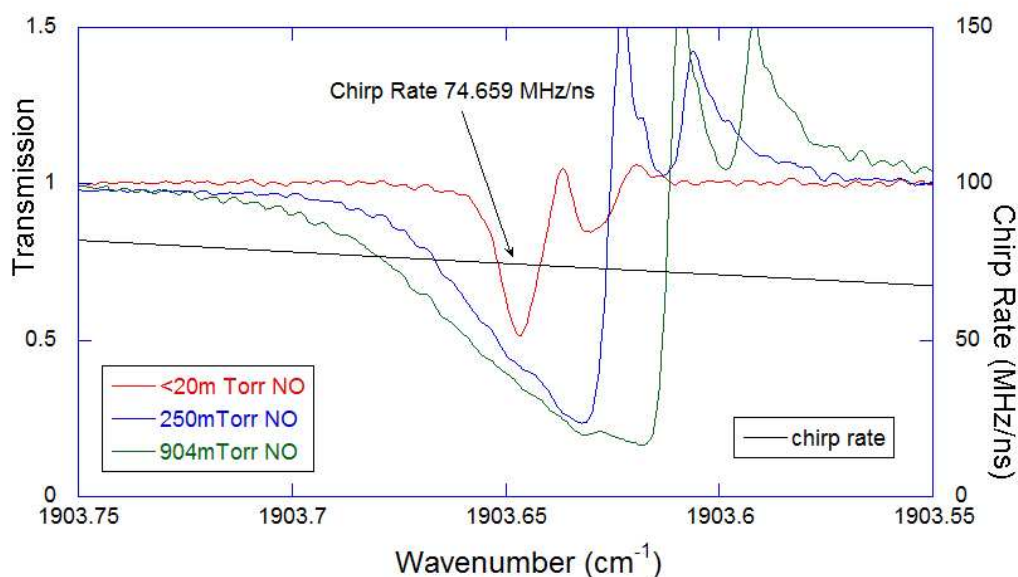


Fig. 4.7: NO R(7.5) $^2\Pi_{3/2}$ singlet mid-chirp

This type of inert collision partner is important for use with nitric oxide as there is a possibility chemical reaction between the nitric oxide and the collision partner due to the reactive nature of nitric oxide.

The laser was set such that the line was near the end of the chirp, with a substrate temperature of -14°C , along with the amount of nitric oxide in the cell reduced to give a transmission of roughly 50% on the doublet. This greatly reduced the rapid passage signals on both the singlet and doublet lines giving a line shape with a less asymmetric nature.

It was noticed early on that the LeCroy oscilloscope took a long time to record spectra when performing 1000 averages. In order to reduce the time taken the averaging had to be reduced to 100 spectra, the downside of this is the added noise on the base-line. The doublet appeared to have the expected behavior in that as the buffer gas pressure was increased the absorption reduced, each of the doublets lines broadened until they took on the appearance of a single broad line.

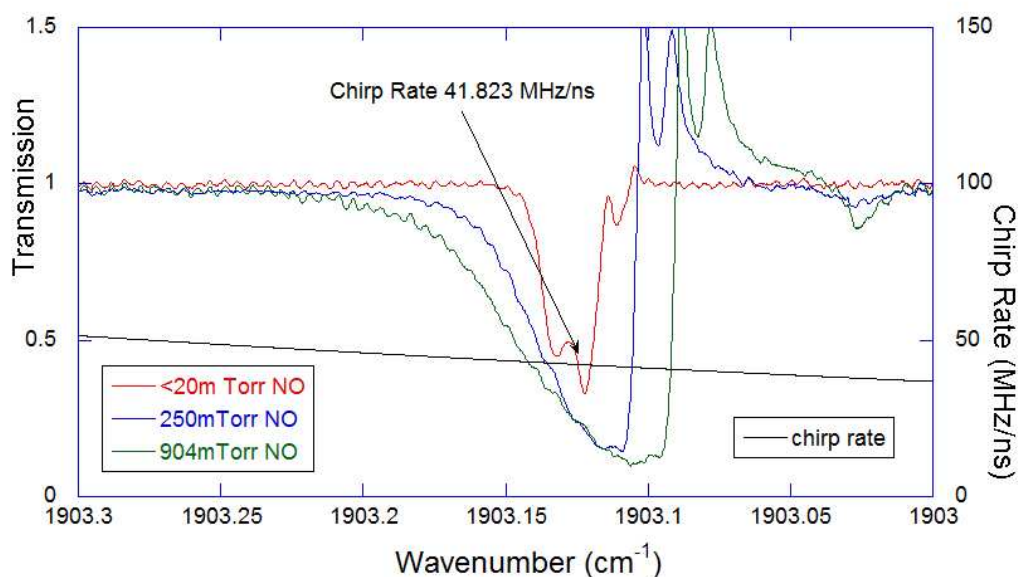


Fig. 4.8: NO R(7.5) $^2\Pi_{\frac{1}{2}}$ doublet mid-chirp

However the singlet line still had the secondary line adjacent that did not behave in the same way as the doublet. Instead as the helium pressure was increased it behaved as if it were two separate lines. This was even more pronounced when the laser temperature was changed to -9°C tuning the laser so the lines were midway through the chirp, which proved to have an even stranger effect.

Figure 4.10 has both the singlet and doublet at mid chirp. On the singlet the separation was even more pronounced than in figure 4.9 (slow chirp), this led us to believe that there was a chirp dependent phenomenon connected to the rapid passage signals. The doublet had a structure that was totally unexpected. When the doublet was at the slow end of the chirp it had the characteristic structure of a partially resolved doublet, however as the feature was 'moved' to the middle of the chirp it developed a third line.

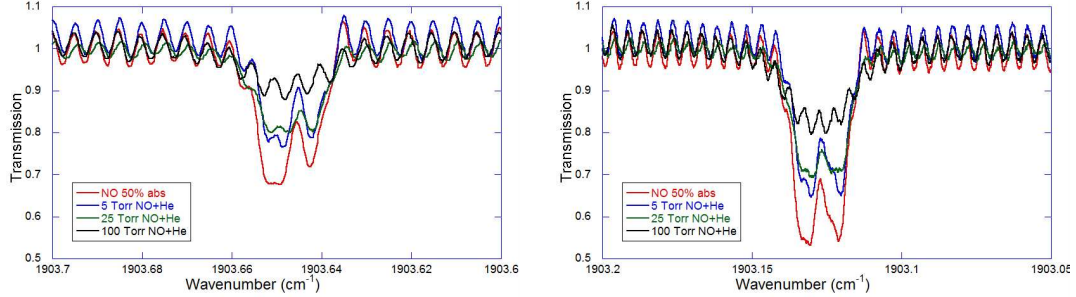


Fig. 4.9: Singlet and doublet R(7.5) lines buffered with helium. The doublet absorption was reduced to 50% and helium added to the cell in steps up to 100 Torr.

The two outer features responded to the buffer gas in the usual manner, on the other hand the central feature was still visible even at the highest pressure of 100 Torr. This in conjunction with the disparity between the expected line structure and the observed structure of the singlet led to the postulate that a form of interference was being induced. Normally the spike associated with the rapid passage is due to the relaxation of the system as the frequency of the laser sweeps through the frequency of the absorption line such that the faster the laser chirps the more pronounced the rapid passage. As the system relaxes there is an associated interference pattern between the emission frequency and the chirping laser frequency. This is the associated free induction decay (FID) which is often visible as a series of 'wiggles' behind the rapid passage spike. This was first observed during nuclear magnetic resonance experiments [77] [78] [46] and has been discussed in associated literature on several occasions [74] [79]. Due to the Λ doubling of the absorption lines it was reasoned that as there was a combination of line doubling and fine structure components, the singlet is made up of four separate lines and the doublet is made from a total of six lines (according to [76] [65] spectral data for NO), that each of these lines would have an emission spike and FID as the laser swept through the feature and what we were observing was a form of constructive interference due to the close proximity of each separate line. The relationship between the chirp rate and rapid passage gave credence to our hypothesis.

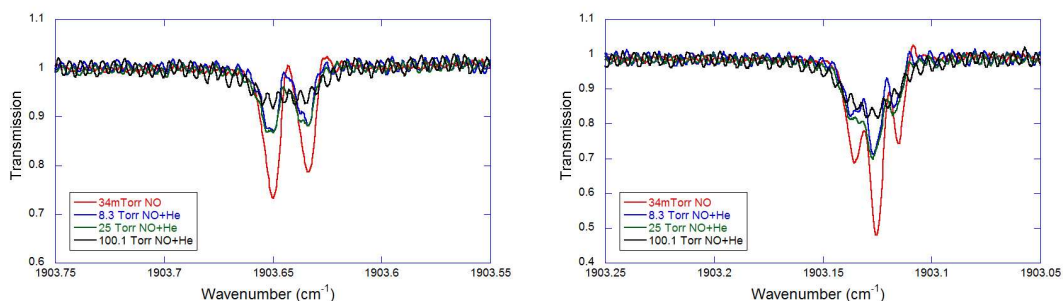


Fig. 4.10: Singlet, left, and doublet, right. Again helium was added in similar steps of pressure for comparison with slow chirp data.

For the collisional experimental runs using Krypton the laser was re-tuned so the absorption lines were again at the slow end of the chirp to reduce any chirp related features. It soon became apparent that the cylinder containing the Krypton had been contaminated with an unknown species.

As the buffer gas was added the new feature became stronger with each pressure step. It was not until the data was analyzed that the new feature was identified as water, the line in question was the R(4) of the $0, 1, 0 \rightarrow 0, 0, 0$ band at 1904.35 cm^{-1} , figure 4.11. Unfortunately this meant that damping of the absorption lines could not be purely attributed to krypton interactions with the nitric oxide.

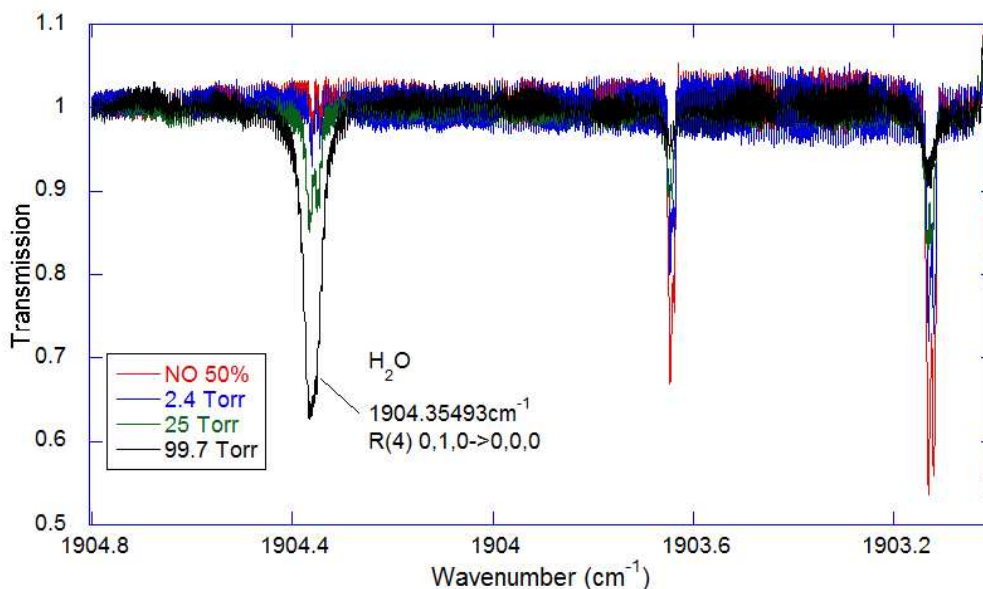


Fig. 4.11: Nitric Oxide buffered with Krypton, a water line clearly increases in strength with buffer gas added confirming a contaminated cylinder.

4.2.2 Pump-Probe

After completing the collisional dampening experiments the White cell was removed in order to set up for the pump-probe experiment. Originally it was hoped to have both the CW and the pulsed beams co-propagating through the cell. For the input beams a beam-splitter would be used to combine the beams however it was soon realized that it would not be possible to separate the beams as they exited the cell. Unlike the system within our lab at Strathclyde University which uses this technique for combining the beams the set-up at Oxford required the use of two separate detectors, a Vigo PVI-2TE8 with an AC coupled pre-amp for the pulsed laser and a Vigo PVI-2TE6 with a DC coupled pre-amp for the CW laser, whereas the Strathclyde system uses the same detector for both pulse trains with a Stanford Research Systems DG535 time delay to separate the pulse trains.

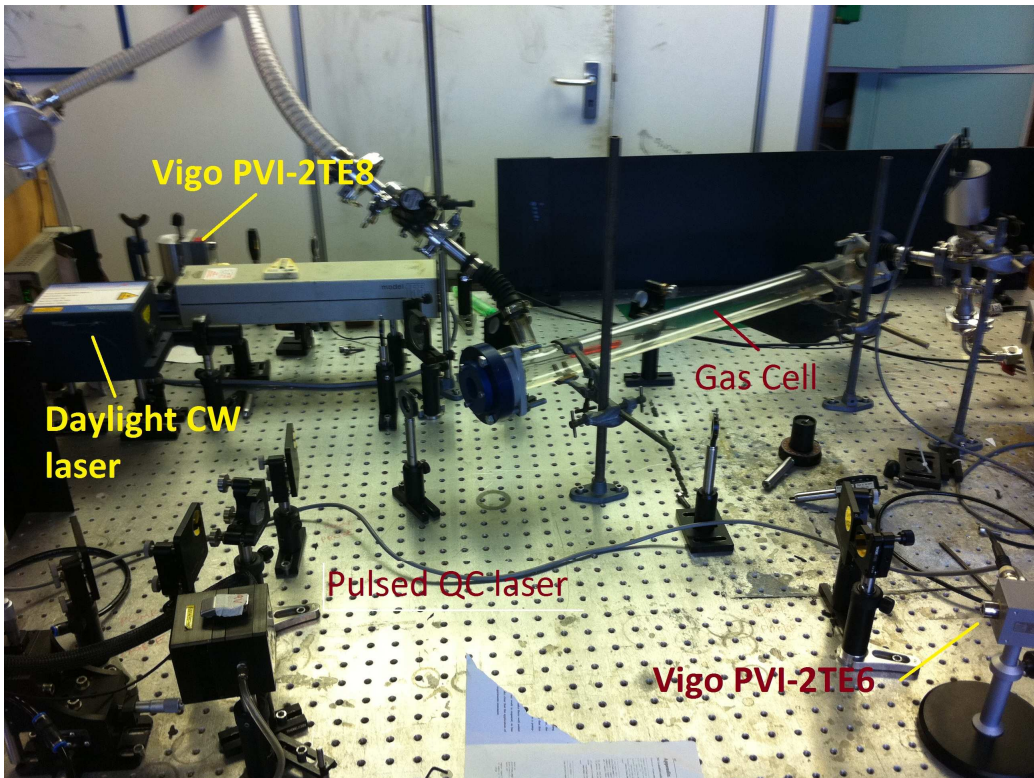


Fig. 4.12: Experimental layout for pump-probe runs.

In figure 4.12 setup for the pump-probe experiment can be seen. The cell for these experiments was a single pass cell resulting in a path length of 70cm through the gas sample. This cell was used instead of the White cell for its ease of set-up, also it had already been used for the Lamb-dip experiments. For these runs the pressure of the sample gas needs to be greater than in a multi-pass cell as the absorber density would be less, given by

$$a_A = P \times l \times \left(\frac{273K}{293K} \frac{1}{760Torr} \right) \quad (4.1)$$

Where P is the gas pressure in Torr and l is the path length in cm, a_A has units of $(\text{cm} \cdot \text{atm})_{stp}$ [80].

In order to maximize the power from the pulsed QC laser it was decided to tune the laser to focus on the Λ -doublet at 1906.15cm^{-1} . To do this the laser temperature was set to -25°C and the pulse length was reduced to 150ns , as the QC lasers are temperature dependent the cooler they are the more efficient they become. For the pump-probe experiments the CW laser was controlled using a PZT, that is a piezo electric crystal transducer attached to the grating of the external cavity system [81]. When a ramping current from a function generator is applied across the grating it allows a controlled scan of 1cm^{-1} at a frequency of up to 100Hz . In comparison to the pulsed system this repetition rate greatly differs from its normal operational settings, on average the pulsed system operates with a repetition rate ranging from 2.5KHz to 20KHz . For the first settings, CW operating at 3Hz and pulsed at 20KHz , no fine structure was visible. It was surmised that the repetition rate of the pulsed laser was too fast so it was reduced to match the rep rate of the CW laser. This turned out to be too slow for the detector/AC pre-amplifier to detect. The slowest repetition rate that could realistically be use with the pulsed laser was 100Hz , fortunately this matched the maximum of the PZT. Again no visible effect was seen. The next step was to attempt to have the pulsed system triggering off the CW system. The trigger output from the function generator controlling the PZT was connected to the pulsed system so that when the current ramp started the pulsed QC laser would fire. A Stanford DG535 digital delay was used in order to delay the signal triggering the pulsed laser, various delay times were tried with no discernible effect on the spectra. As a final thought the triggering of the pulsed laser was controlled by the oscilloscope, LeCroy WaveSurfer 44MXs-A, the thinking behind this was to trigger when each successive ramp of the CW laser was being detected. Unfortunately no matter what was attempted the hyper-fine components were not visible, see figure 4.13.

Although the experiments were unsuccessful it may still be possible to use the CW laser to act as both pump and probe by utilizing the technique mentioned at the start of this section. Indeed a similar technique was theorized for an attempt to perform pump-probe using the pulsed QC laser within the lab at Strathclyde, the lack of space on the optical table meant the set up of the extra equipment would require a major redesign of the existing experimental lay out that we were unwilling to do at this point.

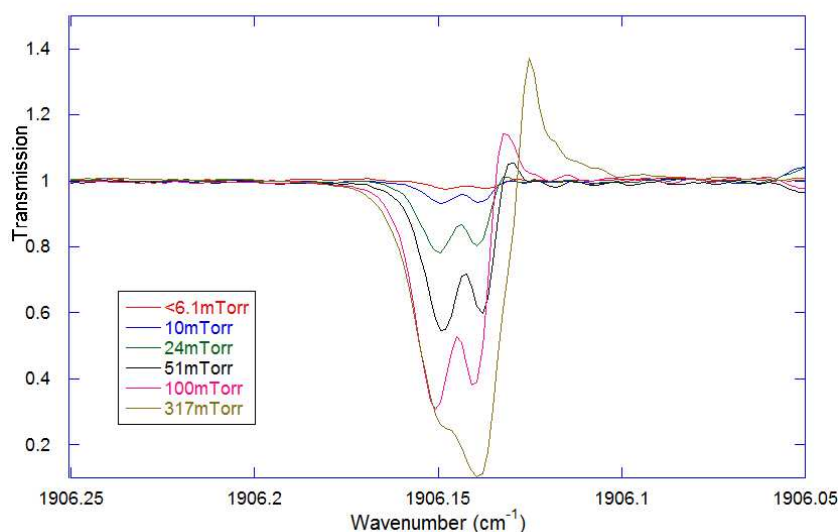


Fig. 4.13: Spectra recorded by pulsed QC during pump-probe experiments

4.2.3 Repeat of White cell experiments

As the pump-probe experiments were unsuccessful it was agreed that some of the experiments using the White cell should be repeated. The reasoning being that if these experiments were repeated and the rapid passage splitting effects were visible again then it would give credence to the argument that the effect was real. For this set of experiments it was decided to look at weak features as well as the main absorption lines. In multi-pass cells it is possible to observe features not normally visible, such as isotopic gases and hot-band transitions. This is connected to the absorber abundance, eqn 4.1, as the natural abundance of isotopes can be extremely low. For example ^{15}N has an abundance of only 0.366%. Similarly the ^{18}O isotope only has a natural abundance of 0.2% and the ^{17}O is even less abundant being only 0.038% of naturally occurring oxygen.

Although it requires higher pressures of the sample gas in order for the weak features to be visible, usually resulting in the main band lines totally absorbing, they often do not have rapid passage effects as this, on average, requires several Torr of sample gas for there to be enough isotopologues, or enough upper band population for the case of hot-band transitions, for rapid passage to be a problem.

This time the R(7.5) doublet at 1903.13 was tuned to be at both the start of the scan where the chirp rate is the fastest and as close to the end of the scan as possible.

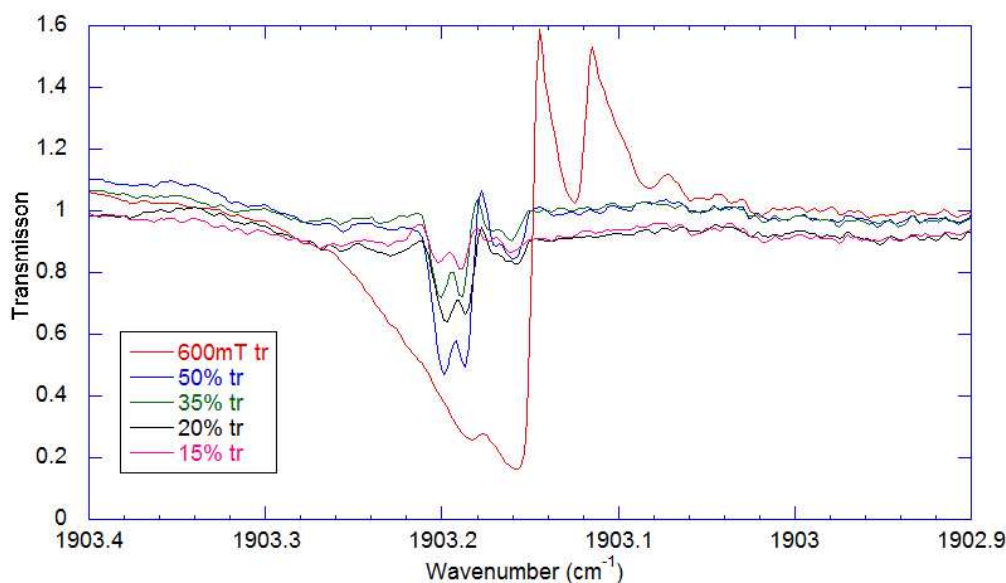


Fig. 4.14: R(7.5) doublet at the start of the laser scan

As the baratron/ meter combination was unable to give accurate low pressure readings (pressures below 20 m Torr) it was decided to work on a rough absorption percentage and to calculate partial pressures at a later time. The pressures were set for each run and the laser temperature was lowered from 0°C to -18°C in controlled steps giving spectra at varying chirp rates, allowing us to explore the chirp related nature of the rapid passage effects. At a substrate temperature of 0°C the R(7.5) doublet was as close to the start of the laser scan without the laser turn-on causing any distortion, see figure 4.14. Again the splitting in the rapid passage spike was visible in the higher pressure spectra, with 600 mTorr of gas in the cell.

The absorption lines were then moved through the laser scan by varying the laser substrate temperature. When the temperature of the laser was at -4°C both the singlet and the doublet were completely in the scan range and could both be said to be in the fast chirp regime, see figure 4.15.

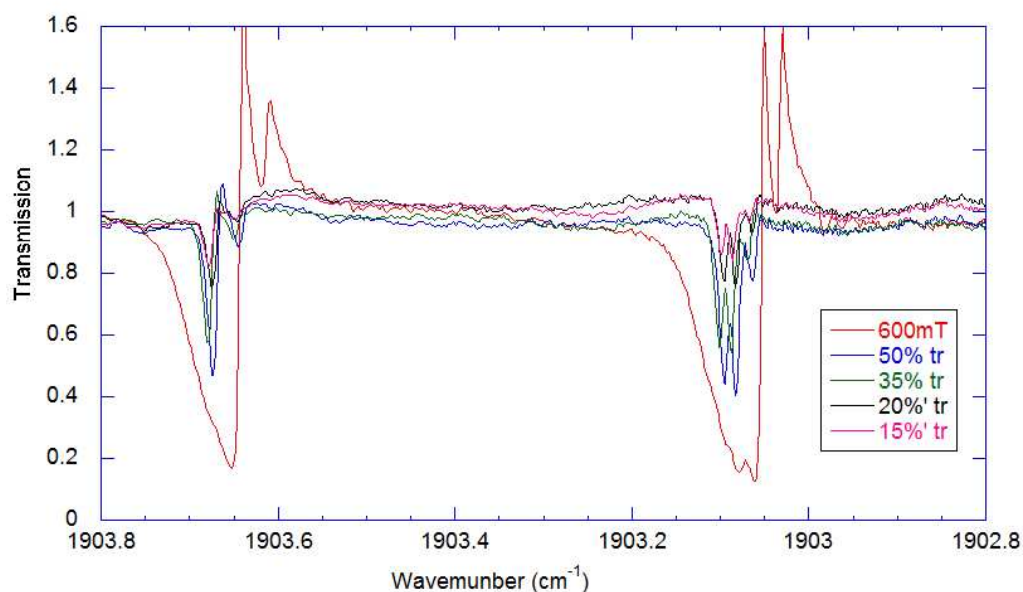


Fig. 4.15: Both the R(7.5) singlet and doublet groups at the fast chirp regime.

The splitting in the rapid passage signals have a marked difference for the singlet over the doublet. For the singlet the amplitude of the secondary rapid passage spike is only half the first spike, giving strength to the argument of interference between features as it had the appearance of damped oscillations. The doublet, on the other hand, had rapid passage spikes of equal amplitude which could be argued that they were spikes associated with each line group of the doublet.

It is not until the doublet is at the end of the laser scan, where the laser frequency chirp is at its slowest, that the rapid passage signal has almost returned to its expected appearance with only a slight splitting at the peak, see figure 4.17.

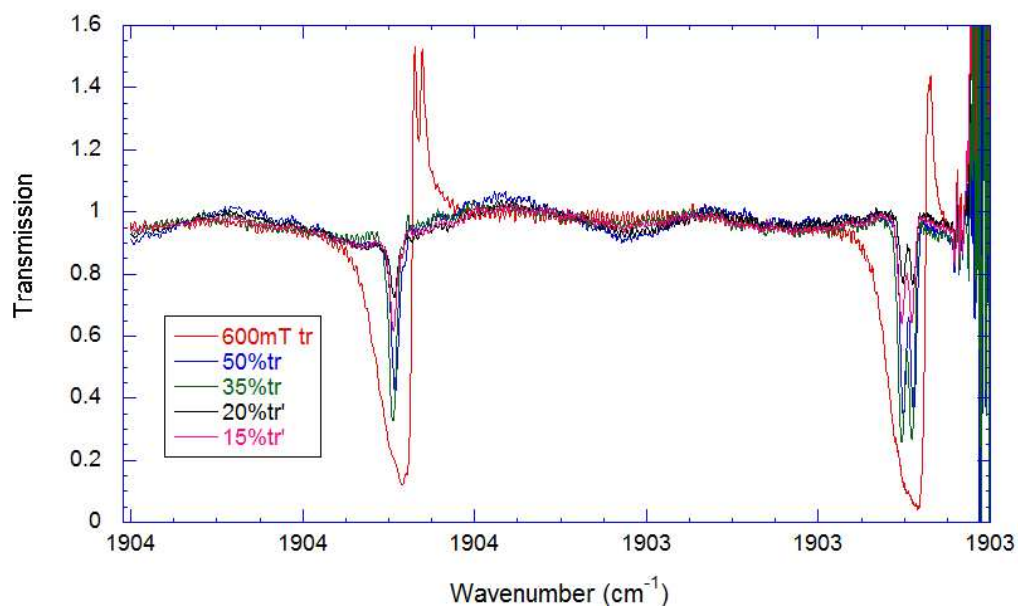


Fig. 4.16: Laser tuned to -14.5°C , this temperature has the doublet at the slowest chirp rate.

On the singlet the secondary spike has the same amplitude as the first and when the singlet is pushed to the end of the chirp, see figure 4.16, it is almost as would be expected with just a small indication of splitting.

With the R(7.5) lines at the end of the laser scan there is a weak doublet visible, the R(20.5)_{e,f} lines of the $^{15}\text{N}^{16}\text{O}$ isotopologue at 1904.4786cm^{-1} and 1904.49cm^{-1} , these are visible mid-chirp and are partially resolved. Also there appears to be another doublet next to the main doublet at a frequency lower by 0.024cm^{-1} . At first this was thought to be the R(27.5) line of the $^{14}\text{N}^{18}\text{O}$ isotopologue, however the HITRAN database lists this doublet to be 0.213cm^{-1} lower in frequency and to be ten times weaker.

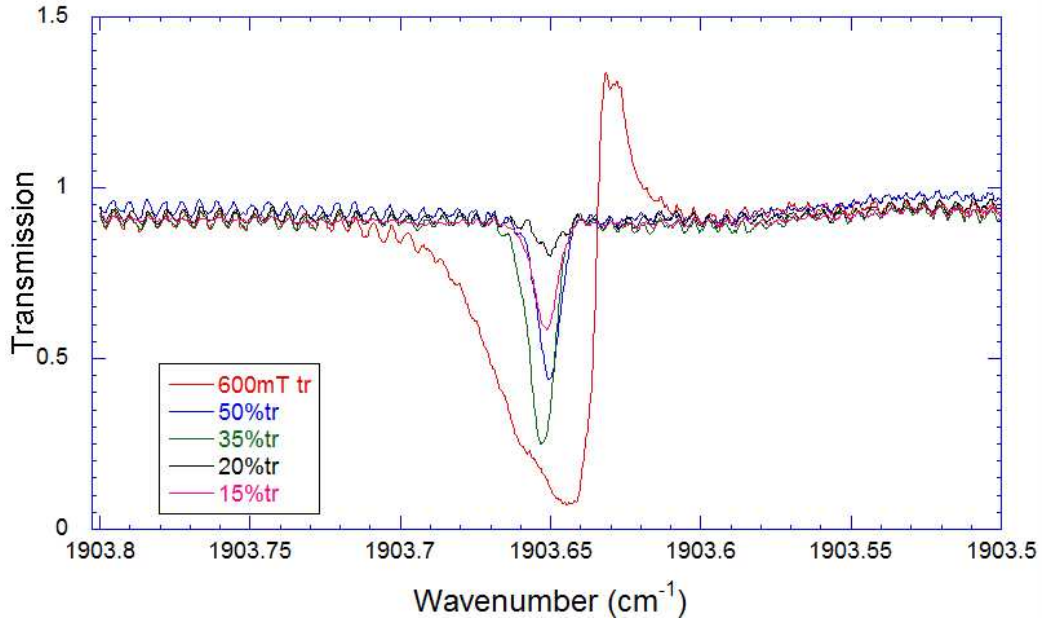


Fig. 4.17: R(7.5) singlet at end of laser scan.

Suspicious increased that there might be a problem, when analyzing the data after returning back to Strathclyde as the R(7.5) doublet also shows this secondary doublet when the gas pressure is low. Figure 4.18 shows the R(20.5), right, and the R(7.5) doublet at 50% absorption, left. Both have the same secondary doublet feature at a slightly lower frequency (both 0.024 cm^{-1} from the main feature) and were recorded mid-way through the laser scan, i.e. mid-chirp. A closer look at the spectra recorded with the lines near the start of the laser scan shows a similar effect, figure 3.39 shows the singlet and doublet lines in the fast chirp regime and under closer examination the secondary lines next to the main absorption lines is visible. When the 50% spectrum is looked at in closer detail, figure 4.19, the secondary features have a separation of 0.032 cm^{-1} , this doubling of features disappears when the lines are at the slow chirp regime.

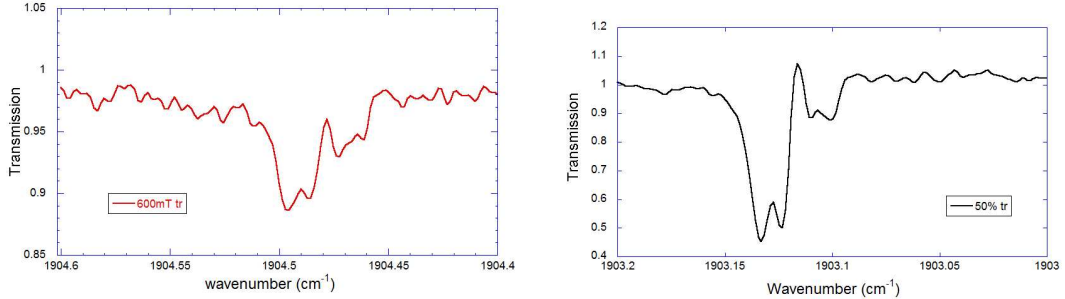


Fig. 4.18: Left, $^{15}\text{N}^{16}\text{O}$ R(20.5) $_{e,f}$ lines with secondary doublet. Right R(7.5) doublet at 50% transmission, this also has a secondary doublet.

This confirmed the effect was chirp related and that the experiments were repeatable also gave credence to the argument that the effect was real.

As part of the analysis it was explored how to remove some of the noise on the baseline. Normally if there is a distortion on the baseline it can be reduced by applying a damped sine wave. However the oscillations on the baseline when using the White cell had the appearance of etalon fringes, figure 4.20. Due to the non-linear nature of the frequency chirp the etalon fringes appear bunched together at the start of each laser scan and more spread out at the end. Each peak has the same spacing in the frequency domain and this allows for determination of relative wavenumber for a spectra. Conversely when the etalon fringe pattern is plotted against time a small section of the plot can be used to determine the spacing of the faces of the etalon.

From figure 4.20 the temporal separation of ten fringes is in the order of 60ns, this gives an average of 6ns between each fringe or *ca* 166 MHz. When this value is put into equation 4.2 where c is the speed of light and l is the physical length of the etalon, the result is a length of 90 cm for the cause of the fringe pattern on the baseline. This turns out to be very close to the separation of the mirrors used in the White cell used in the experiments, the cell had an overall length of 1m but the mirror mounts and the physical thickness of the mirrors would reduce this.

$$\text{Fringe Spacing} = \frac{c}{2l} \quad (4.2)$$

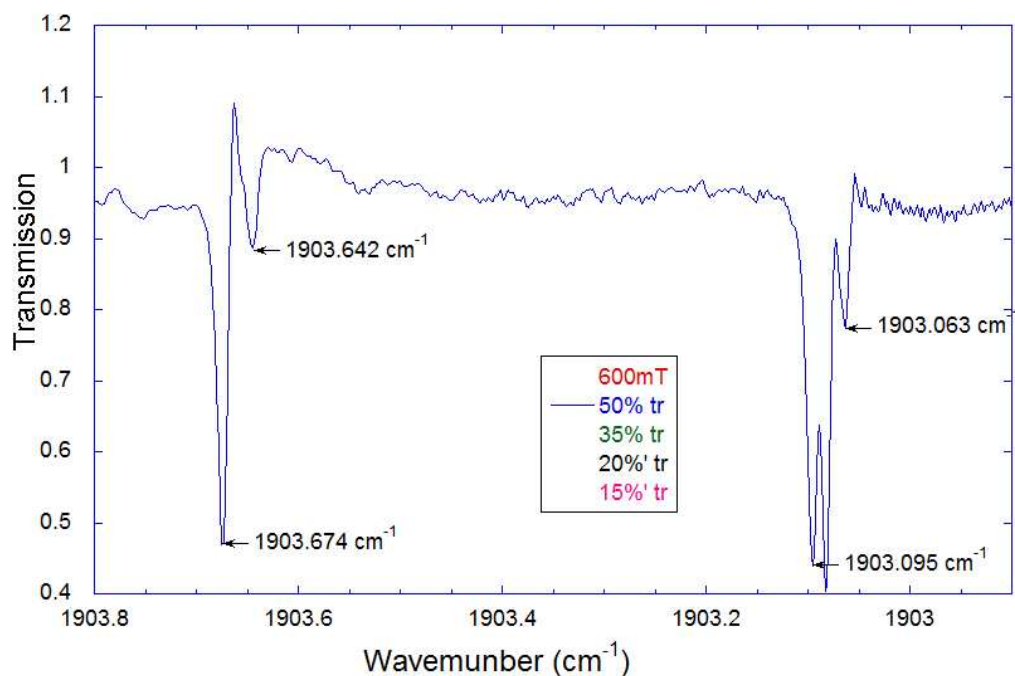


Fig. 4.19: Close up look at the 50% absorption spectra from figure 3.28.

It is clear that there was a problem with the construction of the cell in that the output beam did not fully exit the cell. A portion of the beam being reflected back into the cell would cause interference and result in a fringe pattern in the same way as an etalon.

At the end of the experimental runs, for safety, the gas left in the pipe connecting the cylinder to the cell had to be evacuated through the cell. This put the pressure in the cell over 1 Torr, as the baratron had a range of 0 to 1 Torr the pressure could not be determined. The laser was tuned so the R(7.5) doublet at the start of the scan and left running as the extra gas was let into the cell, with the extra gas in the cell some very weak features were visible, figure 4.21.

Three sets of doublets appeared as the gas pressure increased midway along the scan. This gave a rough idea of the wavenumber region of these lines, as the laser was tuned to start at roughly 1903.5 cm^{-1} and has a scan range of 2.5 cm^{-1} this meant the doublets were around 1902 cm^{-1} .

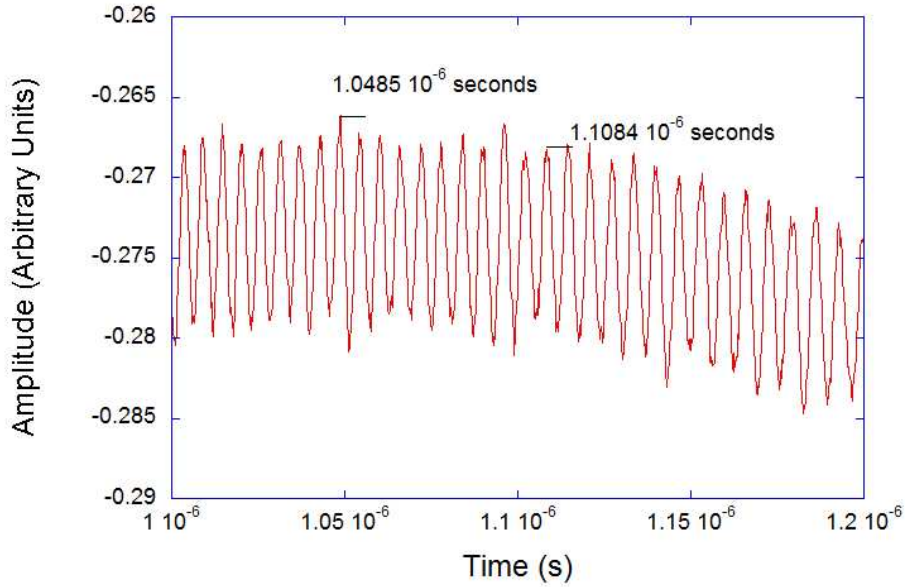


Fig. 4.20: Baseline fringe pattern.

When checking the HITRAN data the strongest of these doublets was identified as the $R(26.5)_{e,f} \ 2\Pi_{\frac{1}{2}}^1 \rightarrow 2 \ \Pi_{\frac{1}{2}}^0$ transitions of the $^{14}\text{N}^{18}\text{O}$ isotopologue at 1902.03cm^{-1} . The fact that we were seeing three sets of doublets caused some debate as with all the experiments so far we had observed a weaker set of lines immediately after the main absorption lines, these were increasing in absorption strength which was counter to everything previously noted. Further investigation would be required to validate that these features were real and not an artifact of the system, this was carried out as part of the collisional tests done at our lab in Strathclyde University.

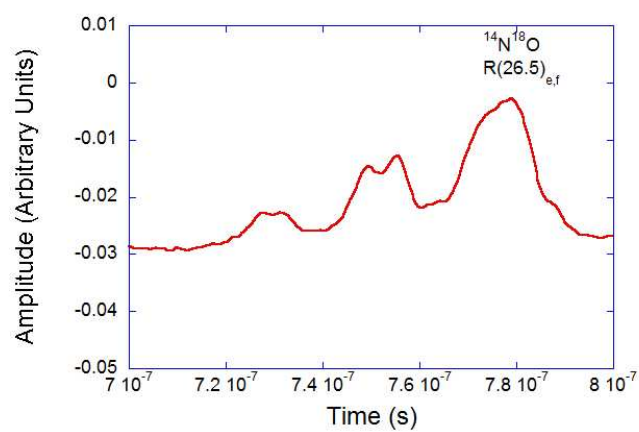


Fig. 4.21: Three set of weak doublets visible due to the higher pressure of NO in cell.

4.3 Collisional Damping Experiments Within Strathclyde Laboratory

A distributed feedback quantum cascade laser, DFB-QCL, is tuned by the heating of a distributed Bragg reflector built on top of the waveguide. The Bragg reflector stops the laser emitting at other than the desired wavelength so as it is heated by the applied current pulse it expands changing the wavelength of the light emitted. When operated in the intra-pulse method the laser rapidly chirps allowing a fast scan of a spectral region. The benefit of this fast scan is that it permits high speed recording of gases, when used in absorption spectrometers, with high resolution. The down side is the resultant line-shapes, rapid passage signal, that arise due to alignment and gain [42] [79] when the lasers frequency sweeps faster than the relaxation time of the system. A method used to minimize this is to introduce a collision partner into the system, usually a gas that does not absorb in the region of interest. Addition of a buffer gas to the system reduces the time between collisions the subject gas experiences thus reducing the effects of the rapidly scanned laser giving a line-shape that approaches a Lorentzian.

An understanding of how different collision partners damp the rapid passage signals that occur with the fast sweep of the laser has important implications in atmospheric monitoring as well as determining the efficiency of collision partners in reducing any nonlinear effects due the fast sweep of the laser. The pressure of the buffer gas required to remove the odd line-shapes plays a part in the design of absorption spectrometers for trace atmospheric gas detection, current systems based on absorption cells use pressures in the region of 100 to 150 Torr of gas flowing through the cell. These pressures give line-shapes that permit accurate determination of the concentration of the trace gases measured, however the dwell time of the sample in the cell limits the speed of the spectrometer so a reduction of the pressure in the cell reduces the dwell time and thus increases the speed of the spectrometer.

4.3.1 Nitrous Oxide

In order to become accustomed with the equipment it was decided that to repeat some experiments with nitrous oxide that had been performed by visiting student Nicola Tasinato should be carried out. Nicola was looking into the effects of molecular collisions on spectral line-shapes. As part of his studies he performed experiments using N_2O as the subject gas and buffered with argon, helium, carbon dioxide and nitrogen, the results were published in [82]. At the time these experiments were carried out Nicola had returned to his home university and had no involvement with the experimental work carried out during this project.

After performing some test runs where only N_2O was added to the cell and then evacuated in steps it was noticed by supervisor G. Duxbury that the absorption strength of the main singlet lines was not as expected, figure 4.22. The $7.84\ \mu\text{m}$ laser was operating at 0°C , 1300 ns pulse, 14 V and a repetition rate of 2.5kHz. These settings covered the $\text{P}(12)_e$ and $\text{P}(13)_e$ lines of the asymmetric stretch $1_0^0 - 0_0^0$ band and as the pressure reading from the baratron was 1.8 Torr these lines should have been fully absorbing with the $\text{P}(20)_{e,f}$ $1_1^1 - 0_1^1$ l -type doublet clearly visible between them.

At first it was believed that there was a problem with the alignment of the beam as it entered the cell in that instead of the beam passing through the front mirror it was striking the back surface of the mirror and returning out of the cell to the detector. This would only give a path length of a couple of centimeter which would explain such a weak signal. Before any adjustments were made to the alignment of the mirrors, either in the cell or on the optical table, another gas was tried in the cell. The ν_4 band of methane absorbs strongly in this region making methane a good choice to check if the alignment was at fault. When methane was added it became clear that the problem was not with the alignment but with the cylinder of N_2O . The N_2O was a Fluka branded sample supplied by Sigma Aldrich in the form of a pressurized tin instead of a lecture bottle. The valve on the tin was not a needle valve that is fitted to lecture bottles and other larger cylinders, and the assumption was it had allowed air to enter. This seems the most likely explanation to why the absorption features were so weak when the baratron reading indicated that 1.8 Torr of gas was present in the cell.

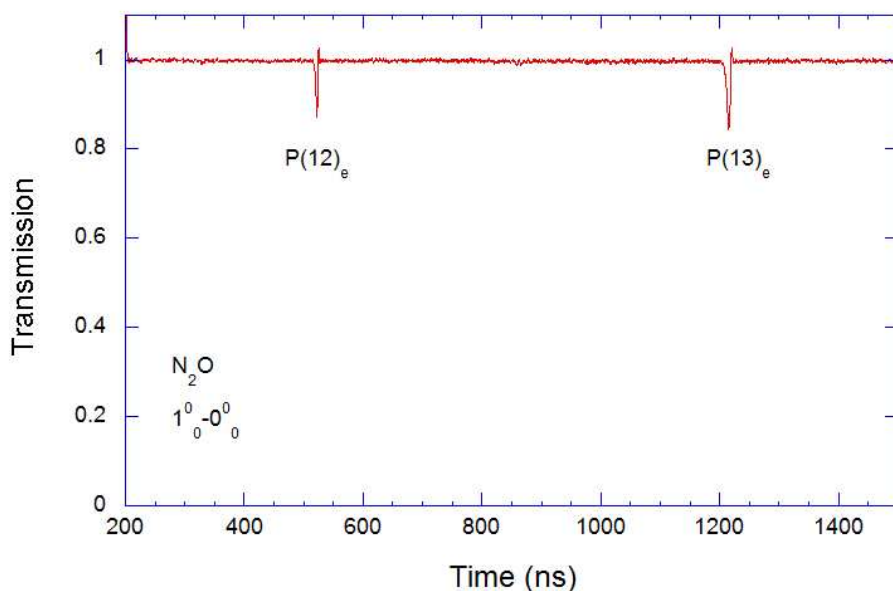


Fig. 4.22: Nitrous oxide recorded during first experiments. Baratron was reading 1.8 Torr

After new cylinders of gas had been procured it was deemed sensible to repeat the original experiments carried out by Dr Tasinato. This provided vital experience using the equipment in the lab and an understanding of how the lasers tuned with different settings. Various settings were used during the experiments, by adjusting the temperature and the voltage applied spectral lines can be 'moved' to different chips rates.

In figure 4.22 the $P(11)_e$ line of the fundamental ν_1 band of nitrous oxide at slow chirp rate of 29 MHz/ns, for the laser settings used the chirp rate of the laser ranges from 100 MHz/ns to 25 MHz/ns. As such low pressures of N_2O are required for the absorption lines to be visible an accurate reading of gas pressure could not be determined using meter/baratron combinations. To get round this the percentage absorption of the line focused on was kept at approx. 40% for each experimental run. Starting at top left and moving clockwise in figure 4.23 the gases used as collision partner are CO_2 , N_2 , He and Ar.

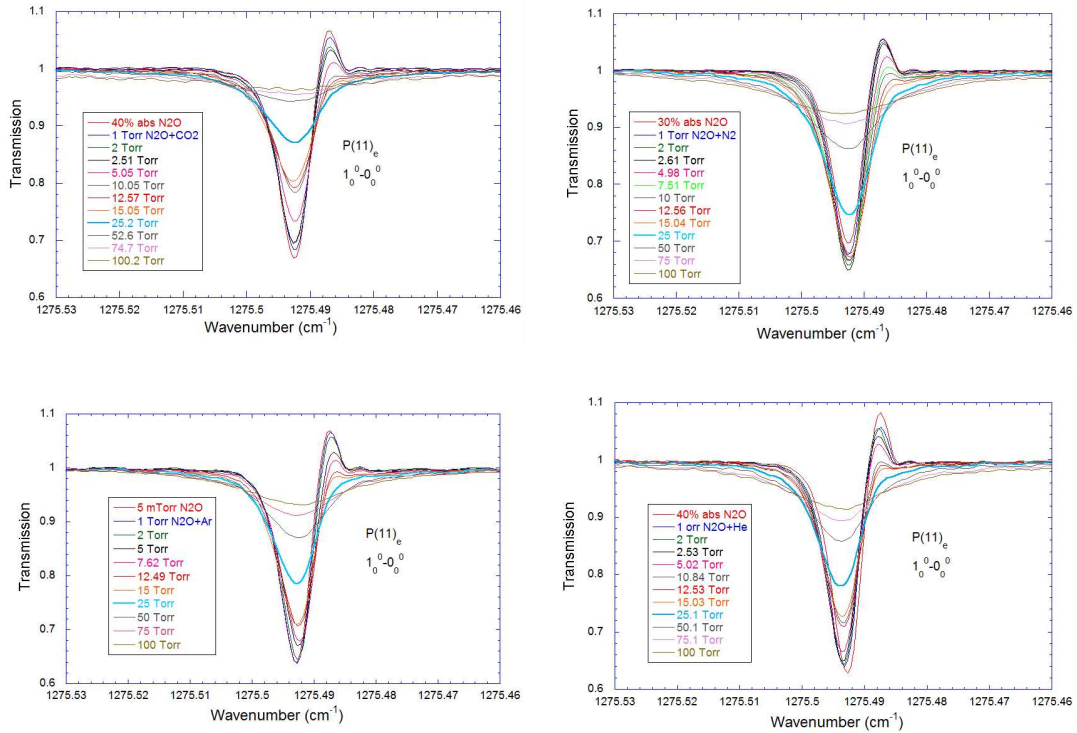


Fig. 4.23: The $P(11)_e \nu_1$ band of nitrous oxide buffered with collision partners CO_2 , N_2 , Ar and He.

In each spectrum the 25 Torr of collision partner added is highlighted, heavy blue line, to show the effectiveness of the collision induced broadening. Helium and Argon show a very similar effect, nitrogen rapidly reduces the gain spike but requires greater concentrations to broaden the line. Carbon dioxide is the most efficient of the gases used here, in both quenching the gain spike and in broadening the absorptive line. For pressures of buffer gas less than the 25 Torr the line-shapes show the same response for each gas. This shows that in this region the laser sweep induced line shape is more dominant than the shape induced by the buffer gas. As the pressure of the buffer increases past 25 Torr broadening of the absorptive part of the line shape becomes more dominant and the difference in the efficiency of the collision partner becomes clearer.

Normally when performing collisional damping experiments the buffer gas is chosen such that it is either not infrared active at all, as for noble gases and diatomic nitrogen, or not infrared active in the same region. Carbon dioxide has its main mid infrared band at $4.3\mu\text{m}$ (2349cm^{-1}), this would make it a good candidate as collision partner when working in the $7.84\mu\text{m}$ region. However there is a weaker band in this region arising from the $^{18}\text{O}^{12}\text{C}^{16}\text{O}$ isotopologue. This band is the symmetric bending vibration and is normally Raman active ($\Sigma_g^+ - \Sigma_g^+$), but the ^{18}O atom breaks the symmetry of the molecule. The centre of mass of the molecule is changed as well as the ^{18}O atom having a nuclear spin of 2.5(Fermi) where ^{16}O has spin 0(Boson) resulting in an induced polarization. In his 1985 paper Toth lists the band centres for the $^{18}\text{O}^{12}\text{C}^{16}\text{O}$ 10002-00001 ($0,2^0,0-0,0^0,0$) and 10001-00001 ($1,0^0,0-0,0^0,0$) bands as 1259.425 cm^{-1} and 1365.483 cm^{-1} respectively [83]. Herzberg refers to these transitions being Fermi-resonant [40] which results in the strength of the absorption lines being greater than they would be expected.

Line	ν_0^a (cm^{-1})	J'	J''	S^0^a ($10^{-25}\text{ cm molecule}^{-1}$)	$\gamma_{self}^0^a$ MHz Torr $^{-1}$
R(24)	1277.77849	25	24	4.977	3.65
R(23)	1277.04724	24	23	5.199	3.69
R(22)	1276.31567	23	22	5.402	3.73
R(21)	1275.58375	22	21	5.582	3.77
R(20)	1275.85161	21	20	5.735	3.81

^a from [83]

Tab. 4.1: Assignment, line strength and self broadening coefficient of the observed rovibrational transitions belonging to the 10002-00001($0,2^0,0-0,0^0,0$) band of $^{18}\text{O}^{12}\text{C}^{16}\text{O}$, table reproduced from [82]

Table 4.1 lists a few of the lines associated with the 10002-00001 ($0,2^0,0-0,0^0,0$) band centered at 1259.425 cm^{-1} that are visible using the $7.84\mu\text{m}$ laser, of these lines the R(23),R(22) and R(21) lines were visible when the laser was tuned such that the N_2O P(11)_e line was at the slow end of the chirp.

The R(23) line is shown in figure 4.24 in the fast chirp region, 75.5MHz/ns . Close examination shows that the 25 Torr of buffer gas pressure added is the pivotal point where the chirp dependent line shape no longer dominates and the line shape induced by the buffer gas is prevalent.

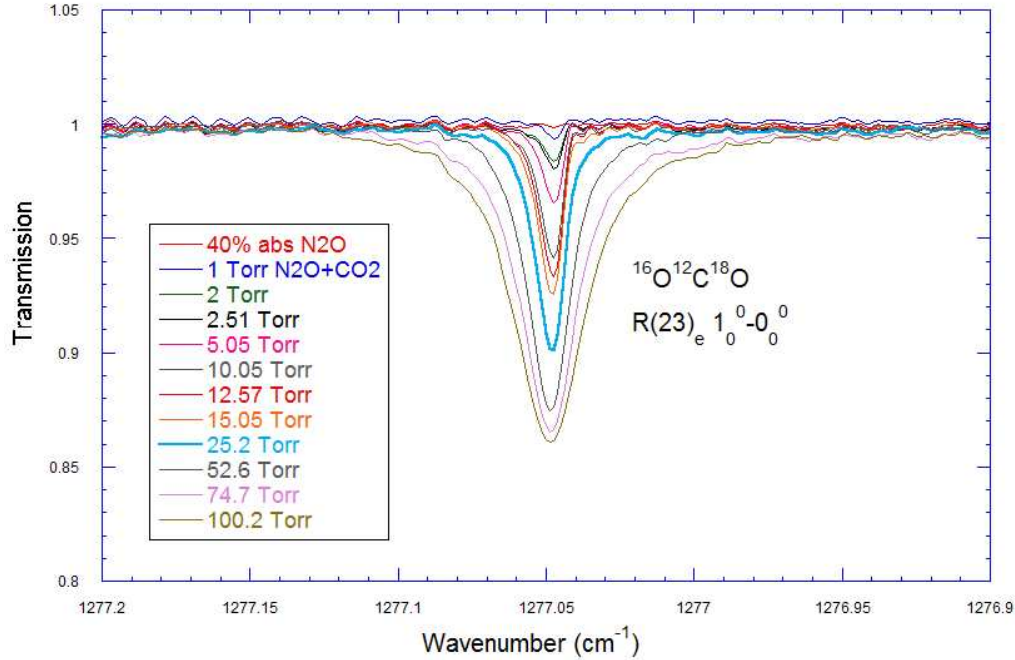


Fig. 4.24: The R(23) $^{18}\text{O}^{12}\text{C}^{16}\text{O}$ of the 10002-00001 band showing a combination of self broadening and collisional broadening with $^{16}\text{O}^{12}\text{C}^{16}\text{O}$

4.3.2 Methane

Methane is one of the most potent greenhouse gases and according to the Intergovernmental Panel on Climate Change (IPCC) it has a 20 year Global Warming Potential (GWP) of 72, that is if the same mass of methane and carbon dioxide were introduced into the atmosphere then the methane would trap 72 times as much heat as the carbon dioxide in the 20 year time scale [1]. This makes understanding the nature of the molecule and how it interacts with other gases of significant importance as it contributes to Global Warming. As with the nitrous oxide experiments collisional damping of the molecule can remove the rapid passage features that arise from the laser scanning through the absorption line and give a line-shape close to a Voigt profile.

As the absorption strength of methane lines had been used to check the cell alignment it made sense to study methane also as the subject of collisional damping experiments. As it is of the point group T_d it has multiple symmetry axes that follow the accepted tetrahedral structure of the molecule. This structure is confirmed by the Raman and infrared vibrational spectra [40]. The fundamental band excited by the $7.84\mu\text{m}$ laser is the ν_4 band, point group T_2 , where the molecule symmetry is reduced by the deformation of the molecule, figure 4.25.

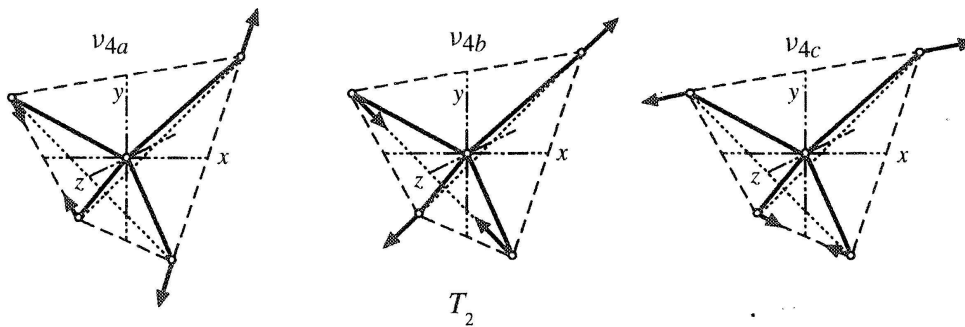


Fig. 4.25: Graphic representation of the deformations of methane ν_4 fundamental, image taken from [40] [38].

The laser was set to scan over the $P(5)$ components, laser set to temperature of -18°C , voltage at 15.5V , a 1500ns pulse length and repetition rate of 2.5 kHz . These settings placed the $P(5)_{f1} 4_0^1$ line at the end of the laser scan where the chirp rate is the slowest and resolution the greatest, chirp rate $\approx 25\text{ MHz/ns}$ giving a resolution of 0.028 cm^{-1} . This chirp rate close to the end of the laser scan was a result of the laser being driven at close to its maximum safe voltage of 16V .

As for nitrous oxide, the collisional damping of the different partners used has the same effect on methane, that is the rapid passage spike disappears when there is $12\text{-}15\text{ Torr}$ of the buffer and the line-shape begins to adopt a more regular profile when the buffer gas pressure is 25 Torr , figure 4.26. The most surprising outcome was the resultant spectra when helium was the collision partner, there is a visible downward shift in the absorption frequency of the spectral line. At first it was thought to be a slight change in the tuning of the laser caused by a temperature variation within the developer head.

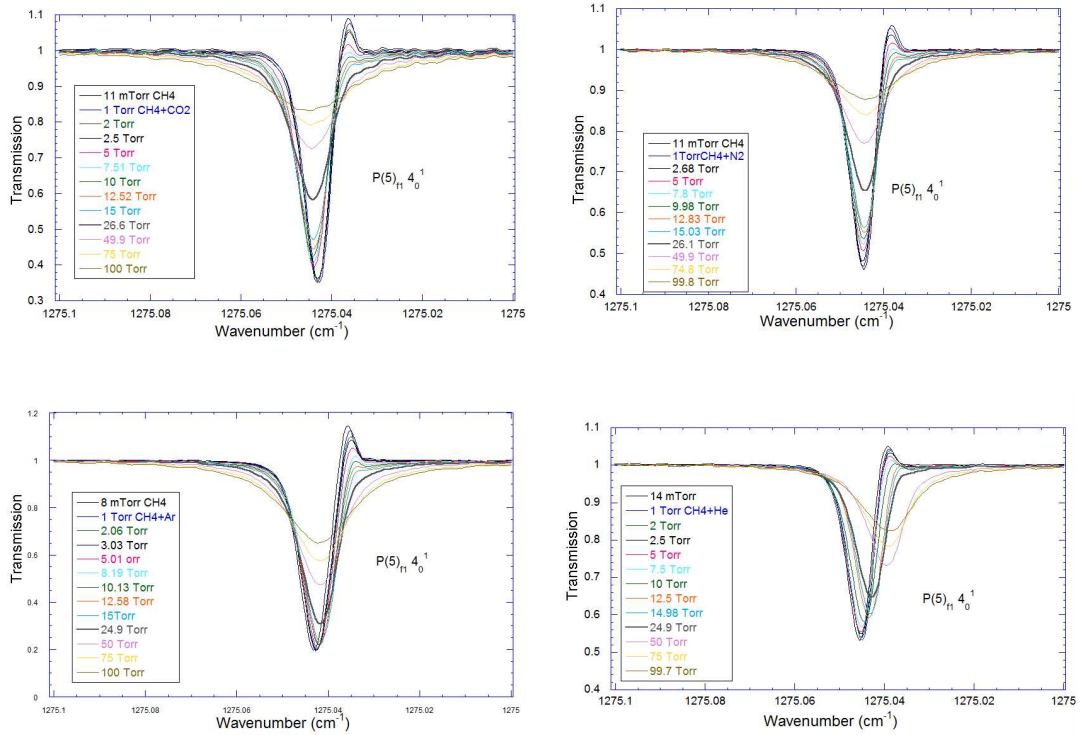


Fig. 4.26: The $P(5)_{f1}$ line of the ν_4 fundamental of methane buffered with collision partners CO₂, N₂, Ar and He.

This was ruled out as a similar shift, although only very slight, is visible in the spectra of the CH₄-Ar collisional experiments. This experimental run was performed after the CH₄-He experimental run with the laser running continuously throughout all the experiments performed that day. Any problem with the cooling in the head would have been clearly visible as it would cause the normalized signal recorded by the acquisition LabView program to distort. The induced shift caused by the buffer gas pressure increasing was ruled out early on, when taking the parameter from the HITRAN data for CH₄ $\delta_{air} = -0.00196 \text{ cm}^{-1} \text{ atm}^{-1}$, as it would only induce a shift of $-2.58 \times 10^{-4} \text{ cm}^{-1}$ for 100 Torr of buffer gas added, well below the resolution of the system.

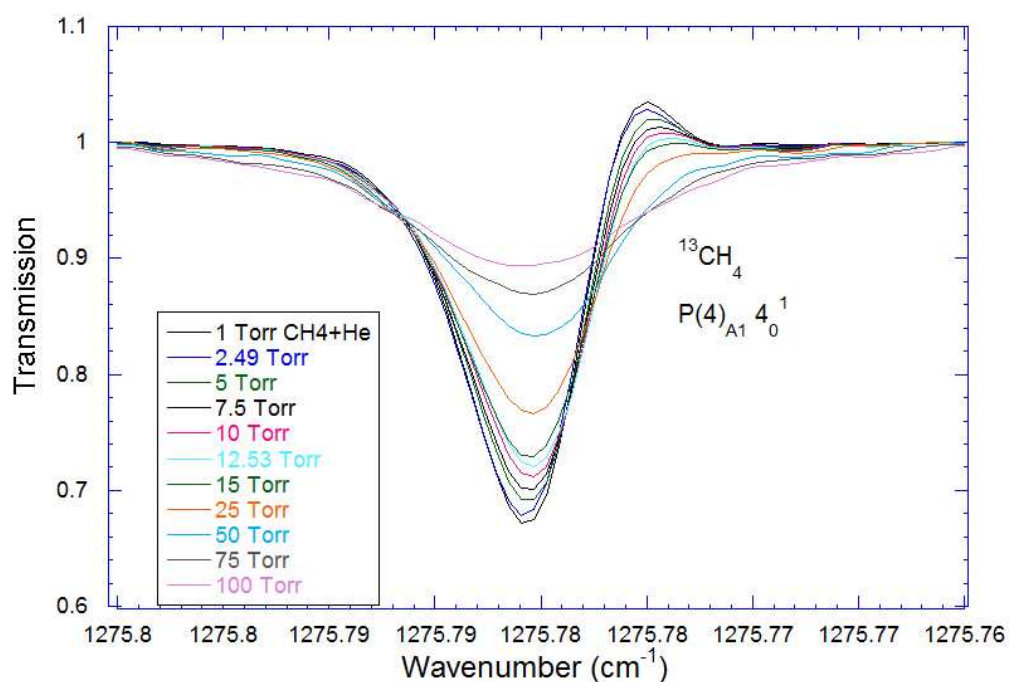


Fig. 4.27: $P(4)_{a1} 4_0^1$ absorption line of the $^{13}\text{CH}_4$ isotopologue also with helium as collisional partner.

In figure 4.27 the $^{13}\text{CH}_4$ isotopologue line $P(4)_{a1} 4_0^1$ at 1275.78cm^{-1} was recorded such that the chirp rate of the laser scan was the same as the $^{12}\text{CH}_4$ $P(5)_{f1}$ line featured in figure 4.26. This was done by reducing the voltage applied to 13V and changing the substrate temperature to -5°C . This also has the downward frequency shift visible leading to the conclusion that the effect was real.

After much discussion the logical thinking was that the shift was most likely the result of the helium collision causing a distortion in the shape of the molecule. This makes sense as the ν_4 band of methane is the asymmetric stretching vibration and if helium atoms collide with individual atoms of the molecule the intermolecular bond lengths would be affected resulting in a change in vibrational frequency.

4.3.3 Nitric Oxide, Repeat of Oxford University Experiments

After returning for Oxford the aim was to repeat the collisional experiments and to examine some of the weak features observed. Unfortunately the only noble gas available at this time was helium so it was decided to use N_2 and CO_2 as these would provide a collisional partner of similar size, especially the N_2 as it is also a diatomic linear molecule with both atoms being the same size (nitrogen has atomic radii of 65pm, oxygen has radii of 60pm).

With the difference in path lengths between the White cell in Oxford and the Herriott cell in the Strathclyde laboratory, the White cell had a 20 m path length and the Herriott cell has a path length of 62 m, the absorber abundance in the Herriott cell is three times that of the White cell. This makes it easier to observe the weak features as there is a greater chance for isotopologues to absorb even though less gas is required to produce a spectrum. So in order to keep the experiments as close to those done in Oxford the nitric oxide was let into the cell and some removed so the absorption was at 50% and at 80% before the collision partner was introduced.

Again the main focus of the experiments was the $R(7.5)$ ${}^2\Pi_{3/2}$ singlet and ${}^2\Pi_{1/2}$ doublet set. The first aim was to have the lines mid to fast chirp to see if there was any sign of splitting in the rapid passage spikes. A temperature setting of -9°C was chosen as this matched settings used in Oxford. It must also be noted that all spectra are recorded in the time domain and converted into the frequency domain during post analysis, so effects seen in the spectra recorded in Oxford are temporal in nature and not additional transitions.

With the pressure in the cell at 1.59 Torr any splitting should have been clearly evident as the splitting seen in Oxford became more evident as the pressure increased. As can be seen in figure 4.28 there is no sign of any splitting on either the singlet or doublet. The next step was to re-tune the laser so the doublet was at the slow end of the chirp, again using the same settings used in Oxford.

Even with the $R(7.5)$ doublet at the slow end of the chirp a normal rapid passage signal, although small, can still be seen at 11 mTorr (red trace in figure 4.29) and as the pressure increases the only distortion to the line-shape is due to the rapid passage. No matter what settings used the signals seen in Oxford could not be replicated with the equipment available at the Strathclyde lab.

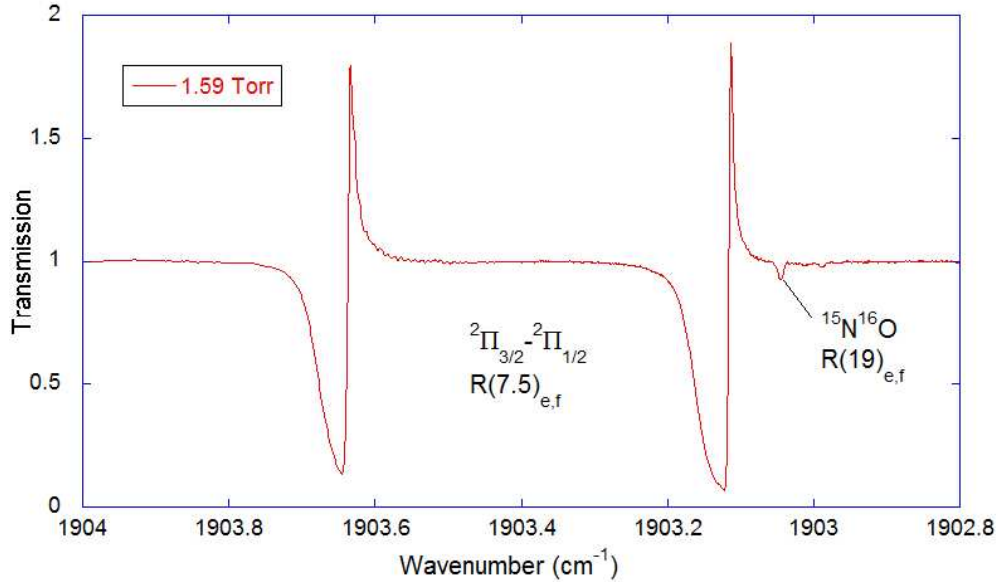


Fig. 4.28: Nitric oxide R(7.5) lines at 1.59Torr.

It was originally believed that the effects seen in the Oxford might have been an artifact caused by the misalignment of the White cell used, however after discussion with Prof. Duxbury concerning some recent publications [53] [54] [55] reporting work on nitric oxide carried out at the Pacific Northwest National Laboratory in the USA it was realised that features seen in the Oxford data could be a real phenomenon only visible due to the matching between the fast Vigo MCT detector and the LeCroy oscilloscope. In figure 4 of [54] the effect of the laser sweep rate on splitting of Λ doublets is shown, the faster the laser sweep the greater the splitting effects. It was already concluded that the splitting in the rapid passage signals was related to the chirp rate of the pulsed laser. Although the splitting in the paper was connected with Autler-Townes effects it may be that the fast pulsing of the laser is causing a similar effect. Also closer examination of figure 3.30, in conjunction with Figure 14(c) of [55], the effect on the R(7.5) Λ doublet shares some similarities.

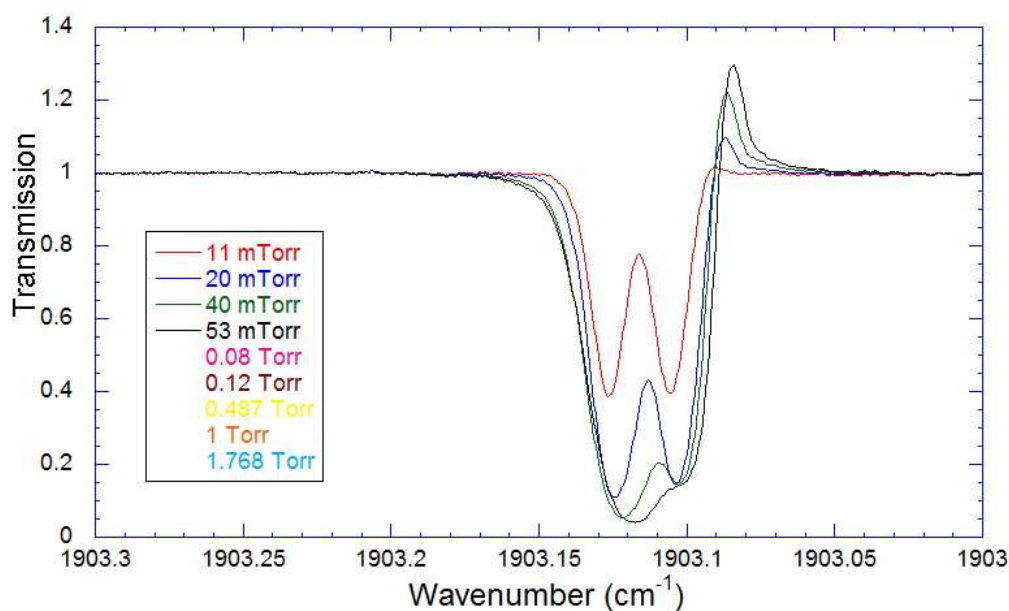


Fig. 4.29: R(7.5) doublet at slow chip. Normal rapid passage signal still visible even at lowest pressure (red trace).

In figure 4.30 the trace marked (i) shows the signal from a short reference cell of length 10cm and (ii) the signal from a 100m path length astigmatic Herriott cell. The bottom trace shows the well resolved doublet however it is the top trace that is of most interest. This displays the line-shape change when laser power is reduced, it is when the laser power is similar to that of the pulsed laser that the line-shape appears to have the constructive interference like pattern seen in the R(7.5) doublet in figure 4.10. This interference like pattern in the doublet was one of the features thought to be an artifact of the system but on closer inspection as the pressure of buffer gas was added the line-shape took on the appearance of a pressure broadened line albeit overlaid with the etalon fringe pattern displayed throughout the baseline, heavy black trace in figure 4.31.

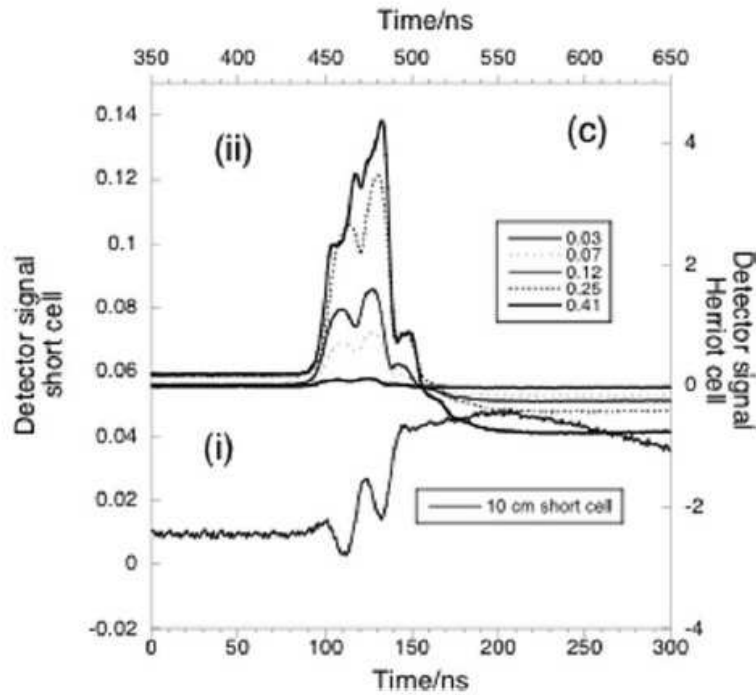


Fig. 4.30: Copy of Figure 14(c) from [55], reproduced with kind permission of G. Duxbury.

The main convincing factor was the appearance of the three weak doublets when the excess NO was let into the cell at the end of the experiments at Oxford. If the effects seen on the singlet and doublet lines were an artifact of the system then a similar effect should also have been visible on these three sets of weak lines.

It appears that the original thinking that the effects seen were an artifact of the system was in error. It is more likely the case that the original beam passing through the cell was causing a population change into an upper energy level, the back reflection within the cell was then causing the interference patterns between the hyperfine components. In essence the misalignment of the White cell was performing a pump-probe effect but without the hyperfine components becoming visible, instead the visible effect is destructive and constructive interference patterns depending on the energy splitting between the e and f components.

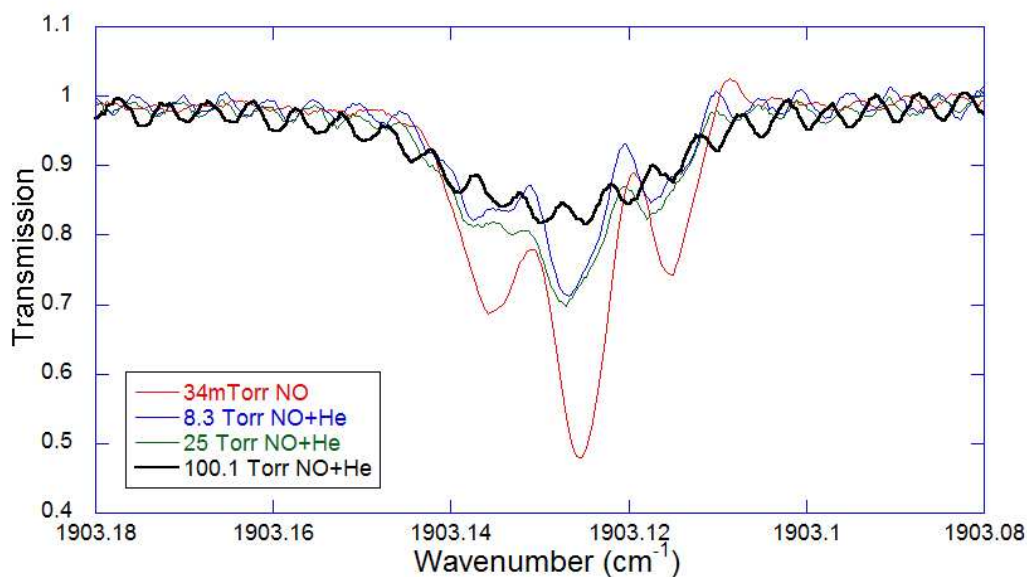


Fig. 4.31: Close up of the $R(7.5)_{e,f}$ doublet, the line shape reverting to a predicted pressure broadened line with increasing buffer gas pressure.

The splitting of the ${}^2\Pi_{\frac{1}{2}}$ Λ doublet e and f components is greater than that of the ${}^2\Pi_{\frac{3}{2}}$ singlets [84] and this would result in the differences in the effects seen.

As part of the pressure tests it was decided to look for the features seen on the last day working with the Oxford group, the set of three doublets shown in figure 4.21. The strongest of these doublets had been identified as the $R(26.5)_{e,f}$ ${}^2\Pi_{\frac{1}{2}}^1 \rightarrow {}^2\Pi_{\frac{1}{2}}^0$ lines of the ${}^{14}\text{N}{}^{18}\text{O}$ isotopologue. With the laser temperature at -5°C and the pressure within the cell of almost 3 Torr of nitric oxide the same set of three doublets was visible at the end of the chirp, see figure 4.32.

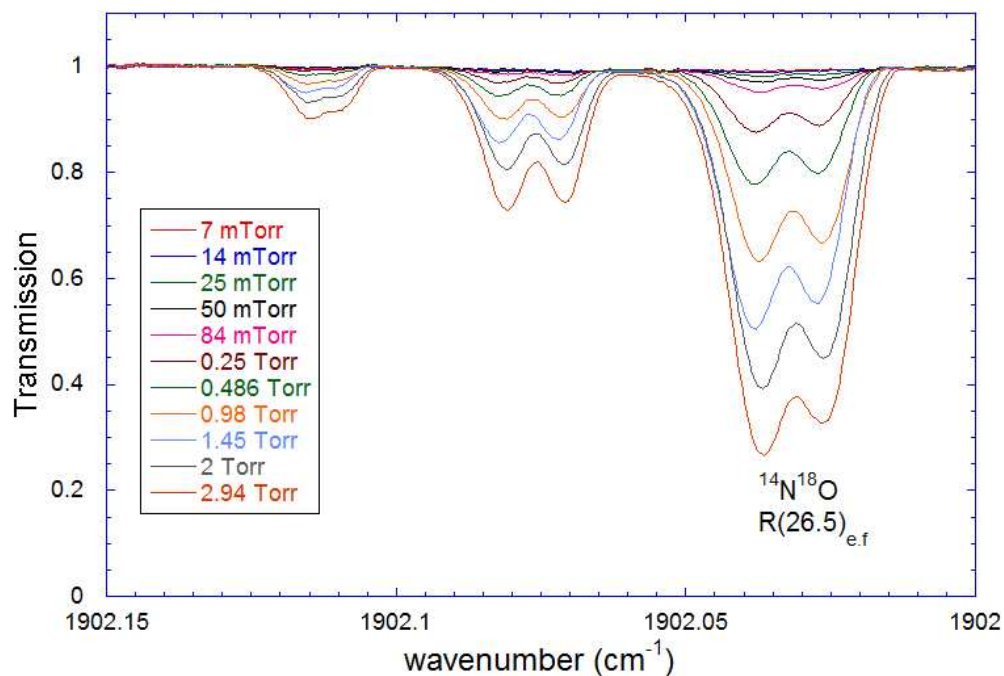


Fig. 4.32: Nitric oxide isotopic doublets, the $^{14}\text{N}^{18}\text{O}$ is the only one listed in the HITRAN database. The others are likely to be $^{14}\text{N}^{17}\text{O}$ and a hot band.

For completeness the laser was tuned so the three doublets were mid chirp and fast chirp to see how the chirp rate of the laser affected the line-shapes, see figure 4.33. At mid chirp the resolution has dropped such that the weakest of the three doublets appears as a single broadened line and at the start of the chirp they have almost all lost any sign that they may be doublets, there is even some rapid passage spikes appearing at the higher pressures when in the mid to fast chirp regimes.

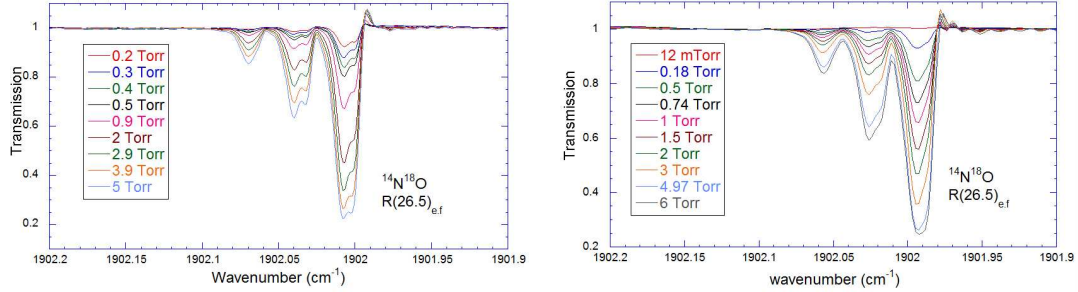


Fig. 4.33: Nitric oxide weak doublets at mid chirp, left, and at fast chirp, right.

As previously mentioned the three doublets are likely to be isotopologues with the strongest of the three already identified as $^{14}\text{N}^{18}\text{O}$, the middle doublet is likely to be $^{15}\text{N}^{18}\text{O}$ and the weakest may be $^{14}\text{N}^{17}\text{O}$ or a hot-band transition. The splitting of the middle doublet is greater than the identified $\text{R}(26.5)_{e,f}$ doublet. This is most probably down to spin statistics of the isotopologues. Being an open shell molecule the electron spin is included in the quantum number \mathbf{J} as $\mathbf{J} = \mathbf{N} + \mathbf{S}$. For the main lines, those of the $^{14}\text{N}^{16}\text{O}$ isotopologue, the nuclear spin has an integer value and $\Delta\mathbf{J} = \Delta\mathbf{F}$, where $\mathbf{F} = \mathbf{J} + \mathbf{I}$ and \mathbf{I} is the nuclear spin. When the nuclear spin no longer has an integer value, when ^{15}N (spin $\frac{1}{2}$) replaces the ^{14}N , this change in \mathbf{I} results in $\Delta\mathbf{J} \neq \Delta\mathbf{F}$. This can result in weaker transitions and different splitting between absorption features e and f levels. So with this in mind it would make sense that the middle doublet could possibly be the $^{15}\text{N}^{18}\text{O}$ isotopologue.

The weakest of the three doublets is only becoming resolved in the slow chirp region, so the theory of it being either a hot-band transition or a low abundance isotopologue seems to be the likely explanation. If not a hot-band transition then it may be $^{15}\text{N}^{17}\text{O}$ as the total nuclear spin of this isotopologue has an integer value and the individual isotopes have low natural abundance. It would require either pure isotopic samples or an accurate simulation to verify these assumptions however most simulated spectra only deal with transitions of the most abundant isotopologue of the molecule simulated.

The next step was to look at how the line-shapes were affected by collision partners. To keep in line with the Oxford experiments the nitric oxide was let into the cell and the pressure reduced to give approximate percentages of absorption. The chosen buffer gas was then slowly introduced in steps up to a maximum of 100 Torr. The first buffer gas to be used was nitrogen as it has a similar atomic structure but is a closed shell molecule of point group $D_{\infty h}$, i.e. it maintains its symmetry under rotation and has no dipole moment and is not infrared active whereas nitric oxide is group $C_{\infty v}$ (a sub group) and has a strong dipole moment. In essence the nitrogen acts as if it is a noble gas and any interaction with the NO should be purely kinetic.

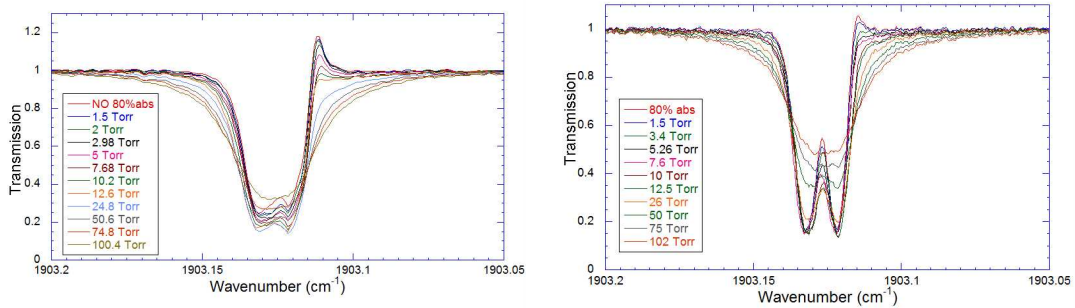


Fig. 4.34: Nitric oxide R(7.5) doublet buffered with nitrogen, mid chirp left ($\approx 53\text{MHz/ns}$) and slow chirp right ($\approx 15\text{MHz/ns}$) .

In figure 4.34 the R(7.5) doublet at mid (53MHz/ns) and slow (15MHz/ns) chirp rates are shown with an obvious difference in the resolution of the individual lines. At mid chirp there is not much of a dip between the separate lines of the doublet and it takes the addition of approximately 25 Torr of nitrogen before a line-shape close to the Voigt profile is achieved, whereas at slow chirp there is close to 40% of total absorption between the lines in the doublet and it only requires 10 Torr of nitrogen before we the line-shape adopts a regular appearance.

When it came to performing experimental runs using helium as the buffer gas the laser setting used in Oxford were duplicated to allow a direct comparison of the two different cells. As the absorber abundance is greater in the Herriott cell for the same gas pressure as in the White cell, the percentage of absorption method was used.

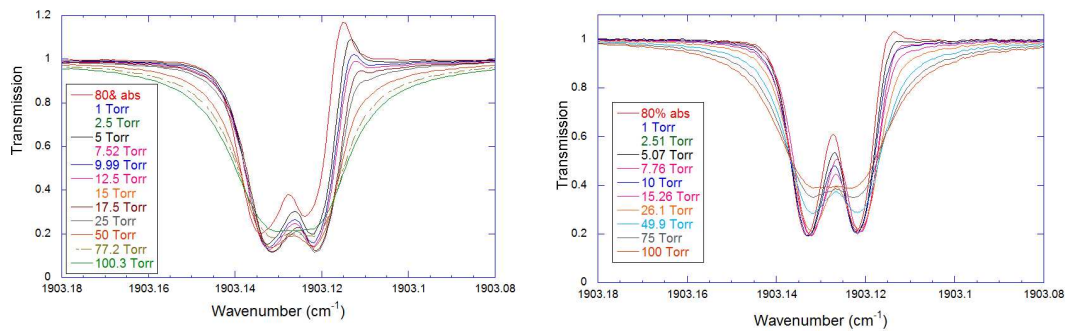


Fig. 4.35: Nitric oxide R(7.5) doublet (80% absorption) buffered with helium as with the nitrogen experiments the chirp rates for the lines positions was the same, mid chirp left ($\approx 53\text{MHz/ns}$) and slow chirp right ($\approx 15\text{MHz/ns}$)

With the absorption at 80% of maximum, figure 4.35, the rapid passage signals show a similar response to the buffering with nitrogen with the spikes vanishing at the same pressure of buffer gas added to the cell. It would appear that the nitrogen is indeed acting as if it is a noble gas i.e. the interaction between the sample gas the the collision partner are purely kinetic in nature. Unlike the spectra recorded during our visit to Oxford University it was possible to observe the response of the rapid passage signals to different collision partners.

It was decided that carbon dioxide should be used as a collision partner as it also has the same point group as nitrogen, it is also a linear molecule, but is triatomic and a strong absorber in the mid infrared, mainly due to the asymmetric stretching vibration centered at approximately 2349 cm^{-1} . Again the laser settings were kept the same, -9°C for the doublet to be mid chirp and -14°C for the doublet to be at slow chirp. Even though absorption of the carbon dioxide is weak in the 1900 cm^{-1} region there is an absorption line close to the NO R(7.5) singlet, CO_2 P(28)_e, see figure 4.36. With the proximity of the CO_2 absorption line to the singlet it was fortunate that the doublet was the main focus of the experiments. There are two weaker lines at a slightly higher frequency that have overlapping wings slightly drawing down the baseline between the lines, as the laser scan from high to lower frequency the rapid passage spike is not affected.

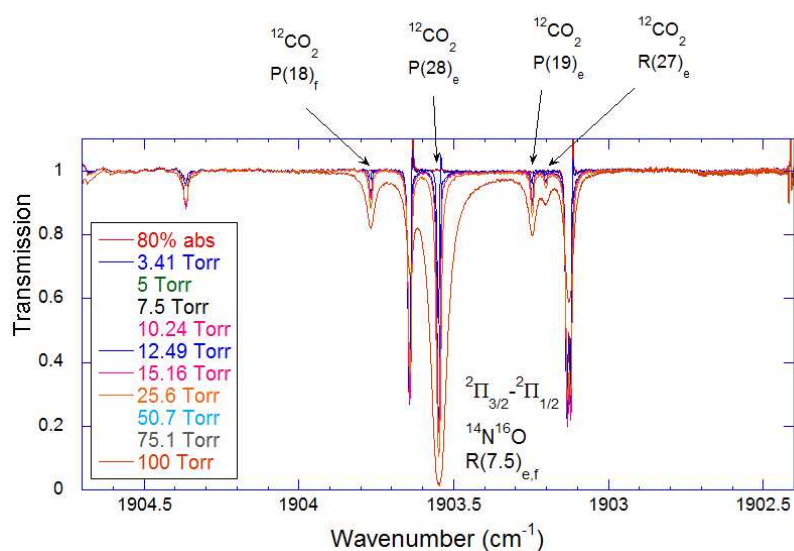


Fig. 4.36: NO buffered with CO_2 . The CO_2 P(28)_e line close to the NO singlet distorts the line-shape so much that any information from the rapid passage damping is lost.

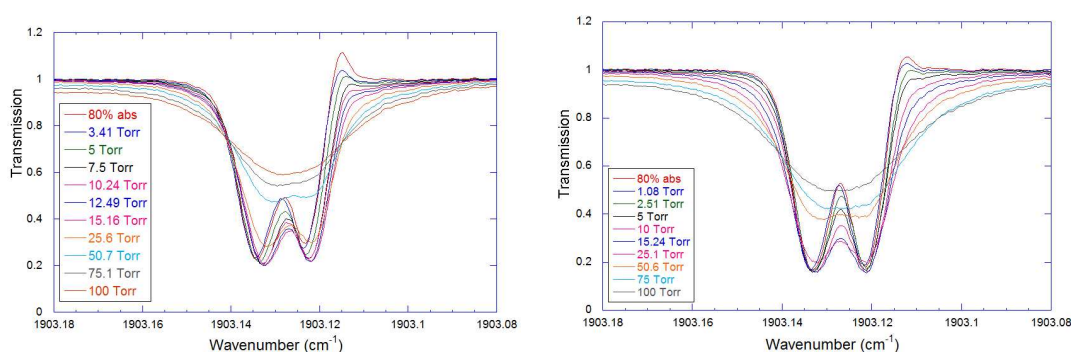


Fig. 4.37: Nitric oxide R(7.5) doublet (80% absorption) buffered with carbon dioxide. The baseline drop is due to weak CO₂ lines.

Unlike with the nitrogen and the helium it only required 10 Torr of CO₂ when the doublet is at mid chirp and 5 Torr at slow chirp for the rapid passage spike to vanish. This would indicate that there is another process other than kinetic interaction damping the system. It is possible that the dipole moment of NO is interacting with the quadrupole of CO₂ making CO₂ a more efficient collision partner.

4.4 Nitrogen Dioxide and its Dimer

While performing the nitric oxide experiments the laser system had been set up so both the mounted lasers were configured to fire sequentially. The lasers used operated at wavelengths of $5.15\ \mu\text{m}$ and $7.84\ \mu\text{m}$ with the $7.84\ \mu\text{m}$ laser being triggered from the $5.15\ \mu\text{m}$ laser. This was done as it was decided to try nitrous oxide as a collision partner as it is also a linear molecule of the same point group as nitric oxide, $C_{\infty v}$, and has a strong permanent dipole moment.

It was during the first set of experimental runs that it was noticed that when only nitric oxide was introduced into the cell the expected spectrum was visible in the $5.15\ \mu\text{m}$ laser window but surprisingly there was a spectrum with absorption features visible in the $7.84\ \mu\text{m}$ window as well. It was initially decided that there was a possible contaminant or a reaction of the gas had taken place in the nitric oxide cylinder as it was not possible to find any reference to spectra in this region, the spectra was recorded then the cell evacuated and some nitrous oxide added as a possible suspect of either the contaminant or reaction product.

In figure 4.38 the red trace is the nitric oxide, the blue trace is 1 Torr of nitrous oxide. This was not the result we expected, only the main transitions of the ν_1 band of nitrous oxide matched with the suspect nitric oxide. On closer inspection there are some weak features that match with the l -type doublets of the N_2O as well as other weak features that did not match.

In an attempt to rule out nitrous oxide as the contaminant gas a similar amount of each gas was introduced into the cell, 27 mTorr of NO was added and N_2O was added to take the pressure up to 60 mTorr. If when the N_2O was added all the lines present increased in absorption strength then it would be likely that there was a contamination of N_2O in the NO cylinder.

Figure 4.39 has the equal mix of NO and N_2O , with the original NO spectrum in red, showing the only lines that increase in absorption are those of the N_2O . This led us to the conclusion that N_2O was not the cause of the features seen. The only other possible gas that could form inside the NO cylinder is nitrogen dioxide, NO_2 .

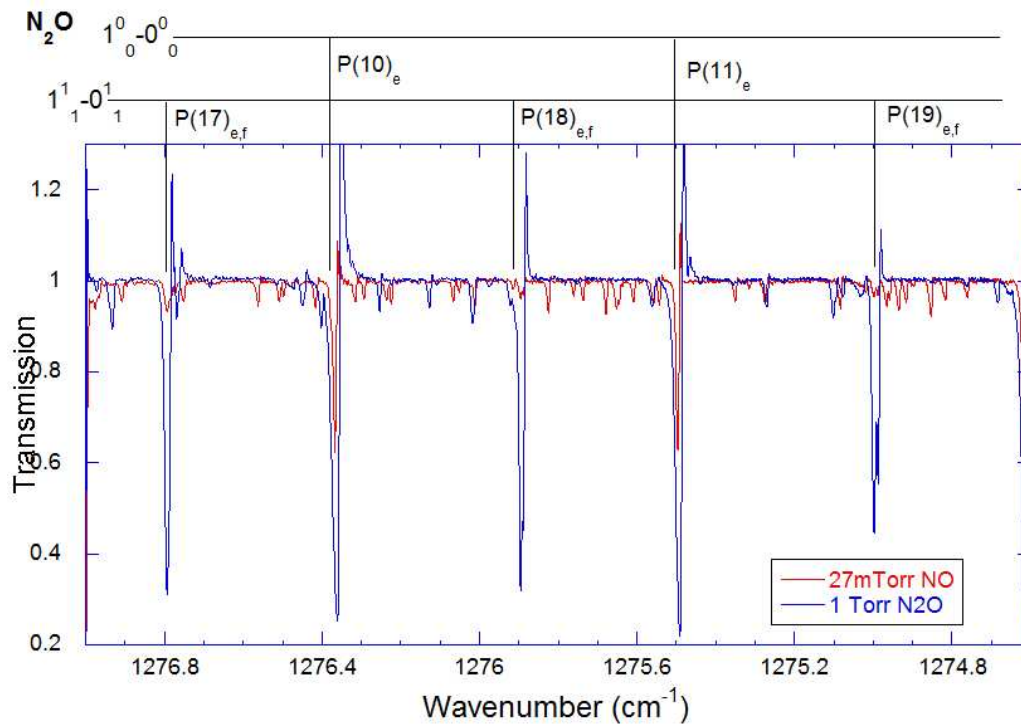


Fig. 4.38: Nitric Oxide in the $7.84\mu\text{m}$ region with Nitrous Oxide spectra overlaid. Both recorded with laser settings of 1500ns pulse length, temperature at -15°C , voltage 15V with an external trigger running at 10 kHz.

According to the HITRAN data the nitrogen dioxide transitions are a factor of approximately a thousand times less intense than the nitrous oxide transitions in the $8\mu\text{m}$ region, with the strongest mid infrared band, the ν_3 band, centered at 1610 cm^{-1} . This is where most detection systems measure concentration of NO_2 , whether that be in the atmosphere or in industrial processes. With this in mind a relatively large amount of gas was introduced into the cell in order to see the many weak lines. It was at this point when it was noticed the baseline was being distorted. Fearing a problem with the laser the cell was evacuated only for the baseline to return to normal. Figure 4.40 shows the baseline distortion when only nitrogen dioxide is admitted to the cell, and with a total gas pressure of 1.75 Torr in the cell. As the pressure was reduced to a fraction of a Torr, the baseline distortion decreased in proportion to the pressure reduction.

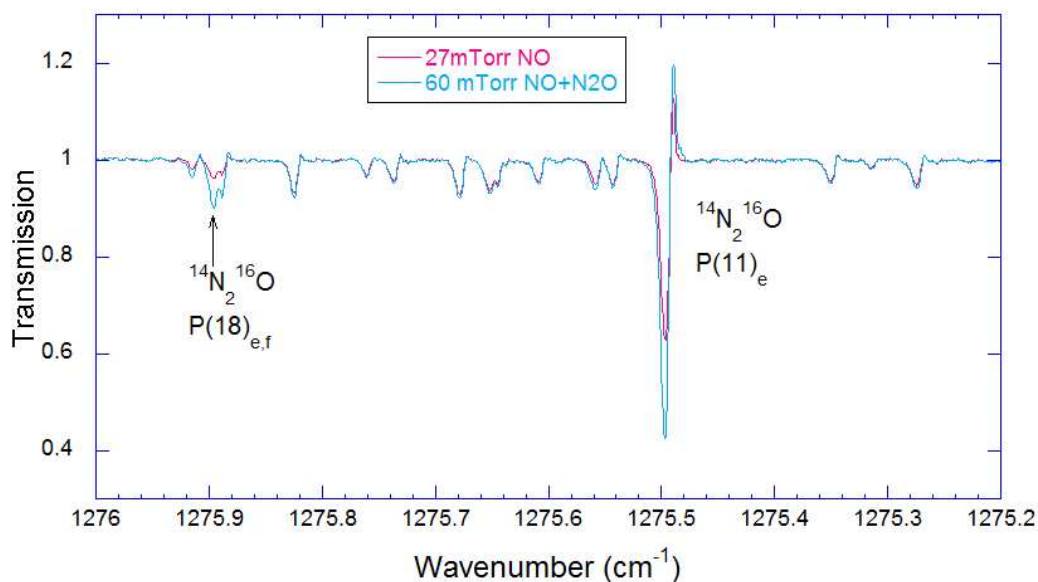


Fig. 4.39: Roughly equal amounts of N₂O and NO, recorded with the 7.84 μm laser.

One thing could explain the cause of the baseline shift, compare figure 11.16 on page 392 of ref. [38]. It shows a spectrum of the atmosphere at an altitude of 12 km recorded by a NASA DC8 aircraft over Greenland. In the spectrum different species that are prevalent at that altitude are clearly distinguishable, namely O₃ and HNO₃ amongst strong H₂O lines, also there is a broad dip in the baseline of the spectrum that is attributed to N₂O₅. In the spectrum the N₂O₅ has its band centre at 1725 cm^{-1} with wings that extend, with no real definition of individual absorption lines, for $\approx 45 \text{ cm}^{-1}$ each side of band centre forming a quasi-continuum.

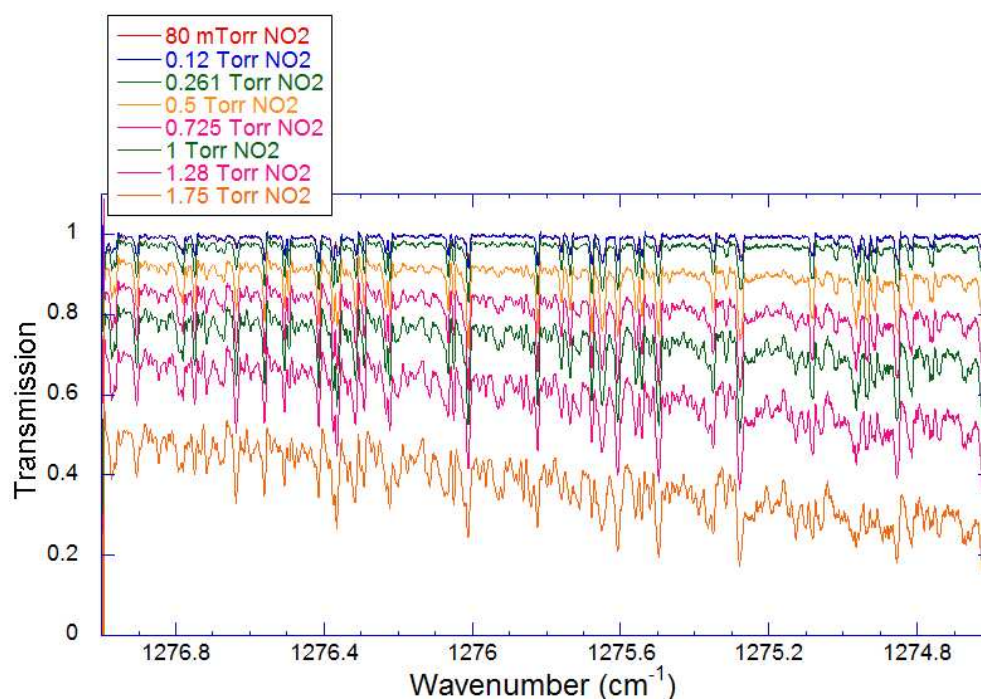


Fig. 4.40: Strange behavior on baseline in the $7.84 \mu\text{m}$ region caused by NO_2 .

In the original publication Toth also states that N_2O_5 has a band that absorbs from 1230 cm^{-1} to 1260 cm^{-1} [85]. It is unlikely that this is the cause of the baseline shift seen in the lab as this compound normally forms in the stratosphere at nighttime through the breakdown of Ozone. It can also be synthesized in the lab by dehydration of nitric acid with phosphorus oxide.

In order to confirm that a continuum state in the 1275 cm^{-1} region was being observed molecules with a known quasi-continuum absorption in the $7.84 \mu\text{m}$ region were tested in the gas cell, this would also confirm the laser was operating properly, see figure 4.41.

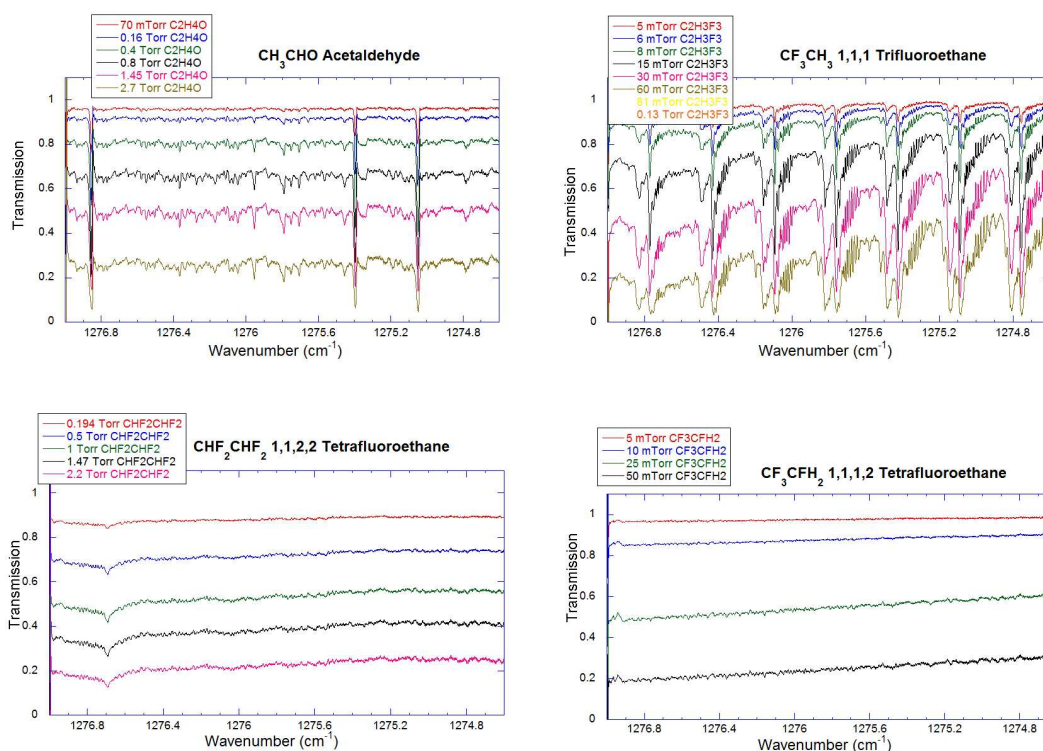


Fig. 4.41: Four molecules each showing a quasi-continuum state with varying amounts of features overlaying the continuum.

Each molecule used can be described as a 'floppy' molecule. They have a single bond between the two carbon atoms with one carbon atom surrounded by heavier atoms than the other carbon, with the exception of 1,1,2,2 Tetrafluoroethane that shows slightly more weak features than 1,1,1,2 Tetrafluoroethane. The single bonded carbon atoms permit the ends of the molecules to rotate freely, this torsion within the molecule can give rise to Fermi resonances where the normally weaker overtone bands gain intensity and the main transitions lose intensity. The resultant spectral lines can have equal intensity. In combination with other perturbations such as Coriolis effects, this can result in many absorption lines that overlap and can appear to be a single broad feature.

So after ruling out N_2O_5 forming in the cell the only possible explanation for the effect seen was therefore that the NO_2 was dimerizing. The equilibrium reaction $2\text{NO}_2 \rightleftharpoons \text{N}_2\text{O}_4$ is taught as part of general experiments at the undergraduate level for chemistry students, for example as described by Hennis *et.al.* [86]. According to Bent in his 1963 paper [87] the dimer can take different forms each with different symmetries. The different conformations will also give rise to a more complicated spectrum. It is most likely that the dimer formed has the form where the two nitrogen atoms form a weak bond, figure 4.42.

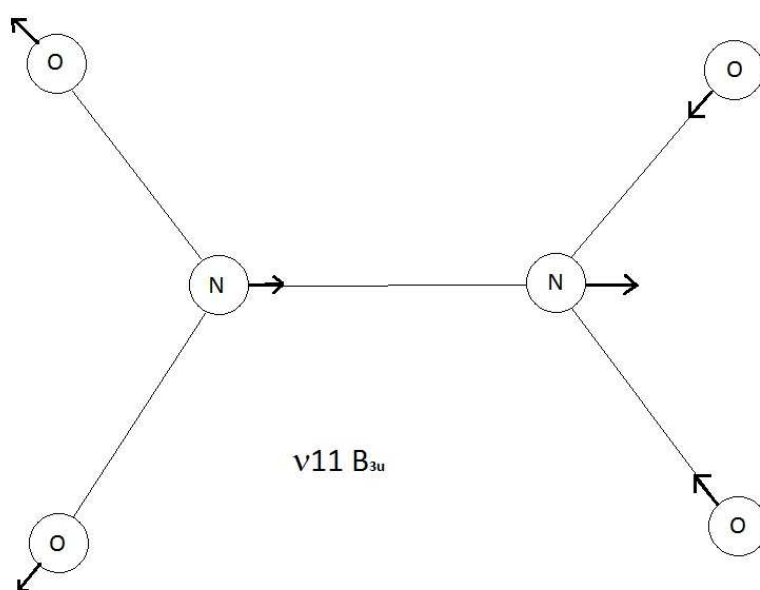


Fig. 4.42: Dinitrogen tetroxide dimer of NO_2 , bold arrows show the relative motion of each atom associated with the $\nu_1 1$ band absorption.

The out of phase symmetric stretching ν_{11} band has its centre at 1261 cm^{-1} [88] [89] [90] and it is absorption in this band that causes the baseline shift seen with the $7.84 \mu\text{m}$ laser. As a way to reinforce the theory of the dimer forming the original experiment where the baseline shift was seen was repeated, with the laser tuned to a different region and use of the $7.46 \mu\text{m}$ laser. By using the $7.46 \mu\text{m}$ laser in combination with the $7.84 \mu\text{m}$ laser the sample of gas can be tested at the same time in two different spectral regions, see figure 4.44. The $7.46 \mu\text{m}$ laser operates in a region where the closest N_2O_4 band, the ν_1 band centered at 1382.3 cm^{-1} , is not infrared but Raman active [91] [92] [90]. The 4C-PQCLAS systems manufactured by Cascade Technologies use a $6.14 \mu\text{m}$ laser for the detection of NO_2 , this region also lies away from any infrared active bands of N_2O_4 but lies in the strong $0,0,1 \rightarrow 0,0,0$ band of NO_2 .

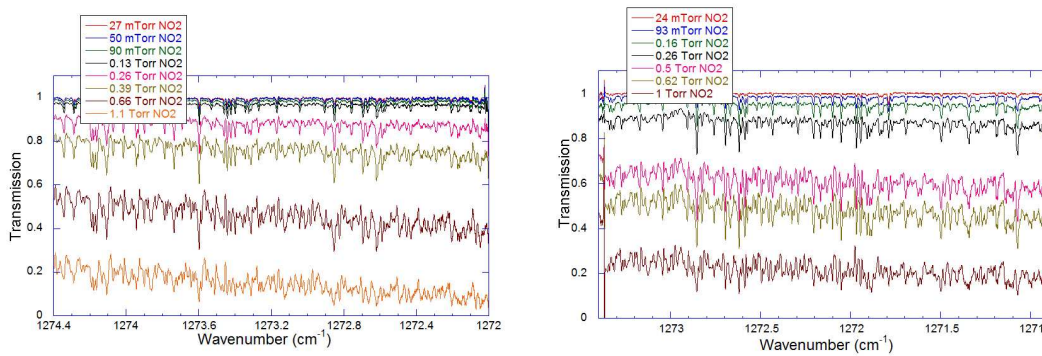


Fig. 4.43: Overlapping spectra displaying the quasi-continuum state as it nears the band centre.

When repeating the NO_2 experiments the $7.84 \mu\text{m}$ laser was tuned by heating the laser to $+35^\circ\text{C}$ such that its spectral window approached the band centre of the dimer. In figure 4.43 the right spectrum is within 10 cm^{-1} of band centre and displays a leveling out of the baseline shift.

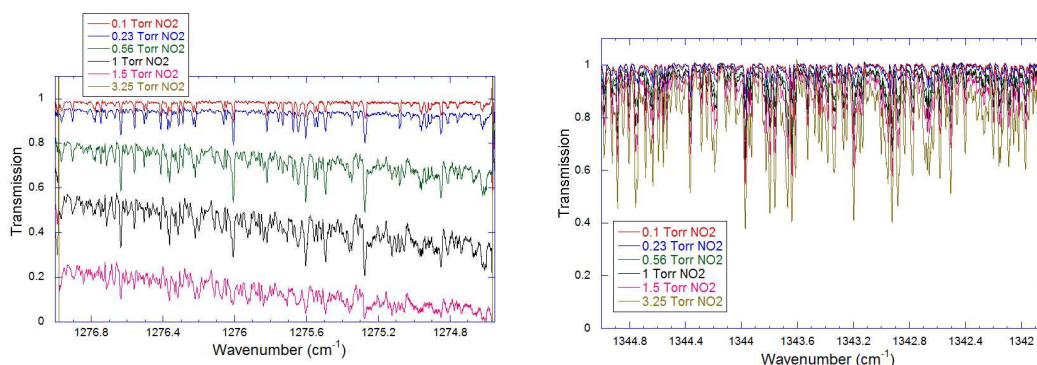


Fig. 4.44: Left the $7.84\mu\text{m}$ laser spectrum of NO_2 clearly visible is the baseline shift with increasing pressure. Right the $7.46\mu\text{m}$ laser spectrum, recorded at the same time as the $7.84\mu\text{m}$ laser spectrum, shows no sign of a baseline shift.

Closer examination of the left hand spectrum in figure 4.43 shows sharp features becoming visible, as the pressure increases, in the gaps in the NO_2 spectrum that we have attributed to partially resolved rotational structure of N_2O_4 . The right hand spectrum shows a small window of the $1,0,0 \rightarrow 0,0,0$ band of NO_2 with no baseline shift, the fact there is no shift in the baseline in this spectrum strengthens the argument that the dimer is forming.

As part of the analysis the work done by Hepp *et.al.* in their 1998 paper [59] was of great interest as they perform measurements at $7.9\mu\text{m}$, i.e. the same region where the baseline effects were seen. In this paper they state that 'only a small fraction of the molecules at room temperature are in the ground state'. They also state that at pressures of 1 atmosphere (760 Torr) the pure gas is almost completely in the dimeric form but in their 1995 paper Dyer and Hendra state that in the gas phase at 20°C a sample of N_2O_4 would be almost 16% NO_2 [93] which would explain why the dimer is visible at pressures as low as 50 mTorr. Hepp and colleagues then performed measurements of N_2O_4 using the supersonic jet cooled method described by Georges *et.al.* [94] to reduce the vibrational transitions available to the molecule. They use a combination of Argon and a research purity mixture $\text{NO}_2/\text{N}_2\text{O}_4$ each with a flow rate of 4litre/minute through a $30\mu\text{m}$ slit. This resulted in the sample being cooled down to 30K ensuring that only the fundamental bands were being excited.

They go on to show that as well as the fundamental bands there is also another a-type band nearby that borrows intensity from the fundamental bands through anharmonic resonance, but unlike the ν_9 and the ν_{12} bands where they identify the associated satellite bands as the combination bands $\nu_6 + \nu_{11}$ and $\nu_6 + \nu_{10}$ respectively the satellite band associated with the ν_{11} band is only described as a 'Dark Band'. They do, however, include the ground state vibrational constants and the vibrational energies, rotational and coupling constants for each of the excited bands studied as well as the resultant observed and calculated spectra.

The listed values were used as parameters input into spectral simulation programs devised by Herb Pickett in 1991 [57] in order to recreate the calculated spectra from the Hepp *et.al.* paper and with the aim of generating a simulated room temperature spectrum. These are a set of copyrighted programs, freely available for use in the spectroscopic community, that calculate line positions and intensities based on ground state and excited state rotational constants. Part of the output data is the calculated value of the partition function for different temperatures. This allows the program to alter the intensities of lines according to temperature. The programs can be downloaded from the NIST Internet resource and come as a collection that can be applied to different natures of molecules from linear molecules, asymmetric and symmetric tops, to molecules with *l*-type structure and molecules with $^2\Pi$ states.

For the simulations carried out only the SPCAT program was used as previous members of the group and Prof. Duxbury had generated calculated spectra from earlier versions of the Pickett programs. As well as this they had written programs that take the output from SPCAT and fit the data to a Gaussian/Lorentzian or Voigt line shape that depends of the path-length and resolution of the spectrometer being simulated.

At first the simulated spectra were substantially different from those in the Hepp paper, this turned out to be a simple error in the .VAR input file for the SPCAT program where not all of the variables were being read by the SPCAT file. After this was remedied the simulations run for a temperature of 30K matched those in the paper. Figure 4.45 shows the Q-branch of the ν_{11} simulated spectra.

By changing the resolution in the fitting routines and fitting the data to have a Lorentzian line shape the simulated spectra shows that even at 30K the overlap of lines can cause baseline distortions, figure 4.46.

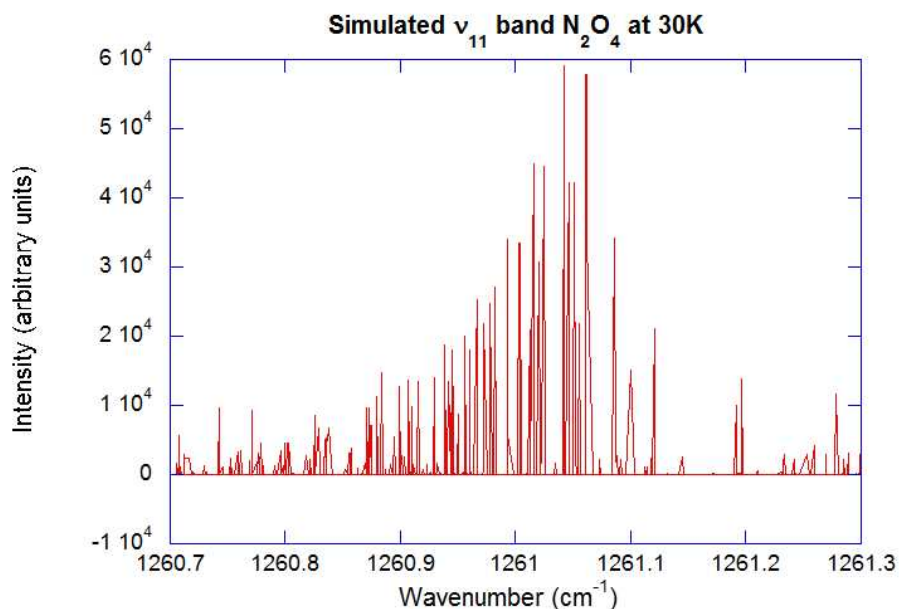


Fig. 4.45: Simulated spectrum of N_2O_4 at 30K. The region shown is the Q-branch of the ν_{11} band.

However it was when the temperature of the simulations was increased to generate a spectrum for a sample at room temperature that the similarities ended, figure 4.47. Closer examination of the Luckhaus and Quack 1992 paper [90] gave the explanation. In this paper supersonic jet expansion is also used to cool the gas, the main difference is that the gas is cooled to 100k instead of the 30K in the later work done by Hepp *et.al.* Even at this temperature there is evidence of hot-band transitions when comparing the recorded spectra of the ν_{11} band and the calculated spectra of the same. This may be due to the lack of the associated 'Dark Band' that is defined in the Hepp *et.al.* paper. This would remove lines from the simulation as well as distorting the intensities of the main band.

It is evident that the structure near the Q-branch of the ν_{11} band in the simulations does not fit with what would be expected and when compared with the work done by Hurtmans *et.al.* in their 1993 paper [89], there is no correlation between the two.

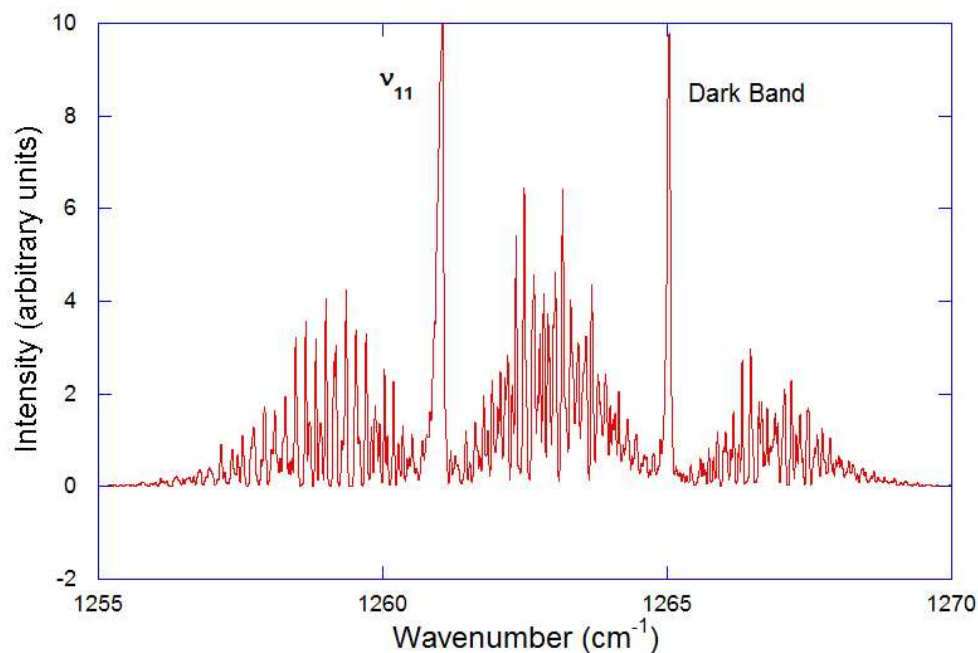


Fig. 4.46: Simulated spectrum of the ν_{11} and its associated 'Dark Band' with data fitted to a Lorentzian line-shape.

This paper is of great importance to the analysis of the effects observed as it has FTS spectra of N_2O_4 from 600 cm^{-1} to 1950 cm^{-1} at varying temperatures, most importantly at 293.15K . After contacting co-author Jean Vander Auwera and discussing the effects observed in Strathclyde he was kind enough to send some of the original spectra including one recorded at room temperature. When a comparison is done between the simulations and the FTS spectra recorded by J. Vander Auwera it is clear that there are other bands present in the FTS spectra over the simulation, due to combination bands of the lower frequency vibrations, giving rise to perturbations such as Fermi resonances. This is displayed in figure 4.48, the difference in the 'Dark Band' R-branch and the area between the two band centres indicates that to simulate the spectrum at temperatures greater than 100K for just the ν_{11} band or 30K when both bands are considered would require far more investigation into the molecule than falls into the remit of this thesis.

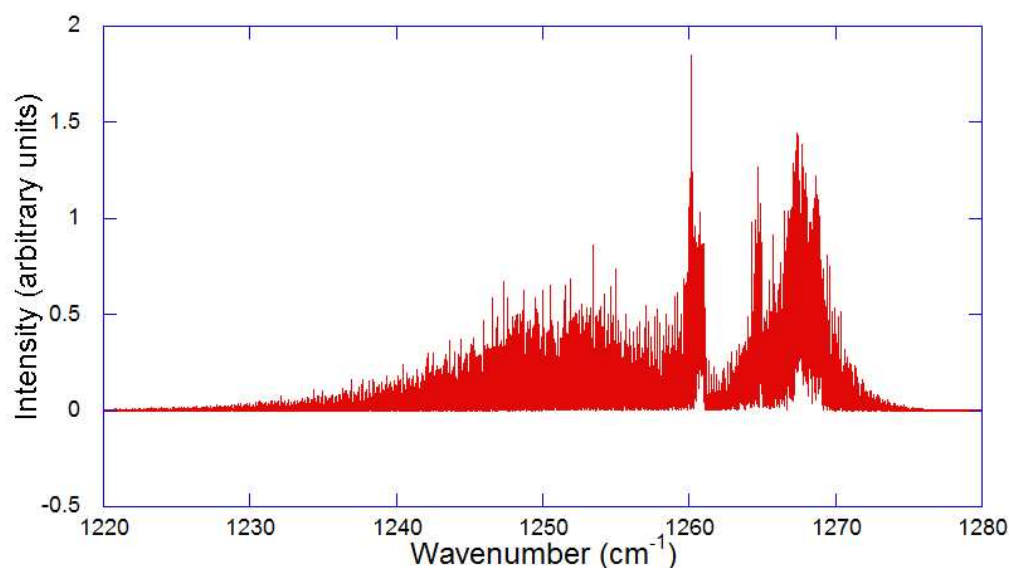


Fig. 4.47: Simulation of ν_{11} and Dark Band at 300K.

Even though the simulations were not matching the FTS spectra performing them was a useful exercise as the Pickett programs can be used to simulate the spectra of other molecules with less features.

As we had a copy of a room temperature FTS spectra of N_2O_4 it was sensible to compare this with the $\text{NO}_2/\text{N}_2\text{O}_4$ spectra recorded at Strathclyde. This would flag up any features that are not visible with low pressure NO_2 but become visible with greater amounts of gas in the cell. Figure 4.49 is a comparison between the FTS spectra of J.Vander Auwera and the Strathclyde Spectra. The FTS spectra was recorded at a pressure of 7.5 Torr and a path length of 180cm, the spectrometer at Strathclyde has a path length of 62m and it is this long path length that contributes to the ability to detect features at low pressures that are normally only seen at high pressures in FTS spectra.

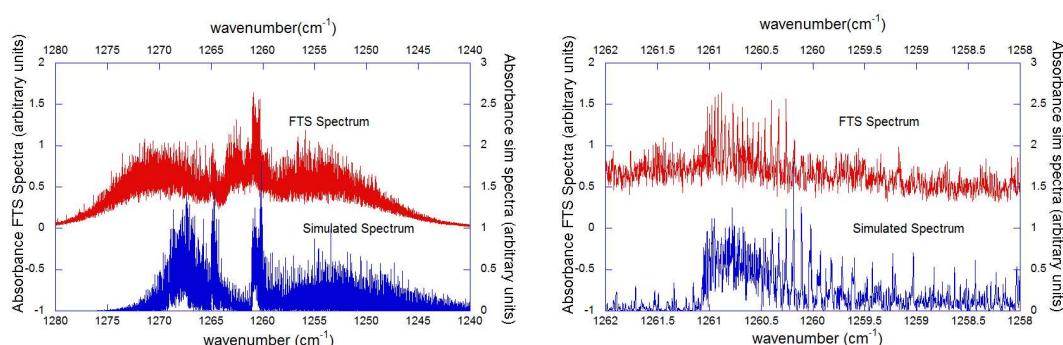


Fig. 4.48: Comparison of FTS and simulated spectra of N_2O_4 , both at a gas temperature of 261.7K. Left shows the ν_{11} and 'Dark Band' for both spectra, the difference is clear. Right is a zoom of the Q-Branch of the ν_{11} band, although there are some matching features the intensities of individual lines differs greatly. In the FTS spectrum the Q-Branch line intensities indicate the presence of a Fermi resonant combination band.

When the two spectra are looked at in detail, Figure 4.50, the features visible at 80mTorr and 0.1Torr can be attributed to be that of NO_2 only. As the pressure increases new features, as well as the baseline shift, become visible in the 'gaps' between the NO_2 lines that match with features in the FTS spectra. This again confirms that the cause of the baseline shift is the formation of the dimer and that with the long path length in the Herriott cell enables the detection of dimer formation at pressures as low as 100 mTorr of NO_2 .

Gas detection and monitoring systems that employ a multi-pass gas cell, such as the systems manufactured by Cascade Technologies and those used by the National Physical Laboratory and the Met Office, normally operate with gas flowing through the cell. The Cascade Technologies systems operate at pressures from 50 Torr to 150 Torr of gas flowing through the cell so a prudent course of action was to see if N_2O_4 is detectable at this pressure.

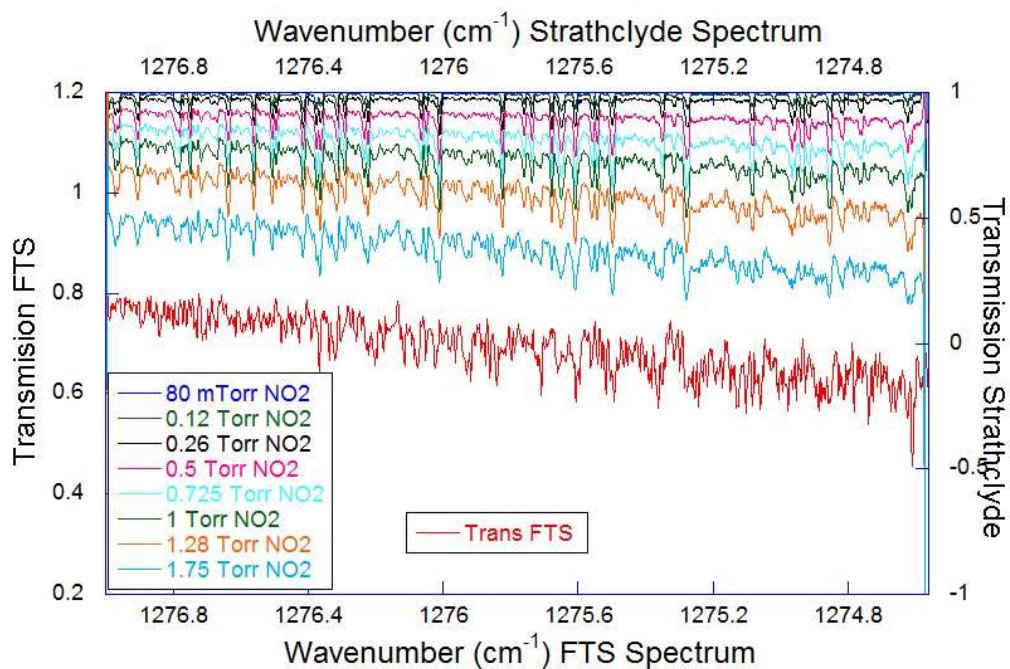


Fig. 4.49: Comparison of FTS and recorded Strathclyde spectra.

To do this sufficient NO₂ was added to the cell to see the dimer forming, i.e. the baseline being shifted down, and nitrogen added up to a pressure of 100 Torr. As with previous tests the 7.84 μm and the 7.46 μm lasers were used in the double pulse configuration so the same sample is tested in the two regions at the same time.

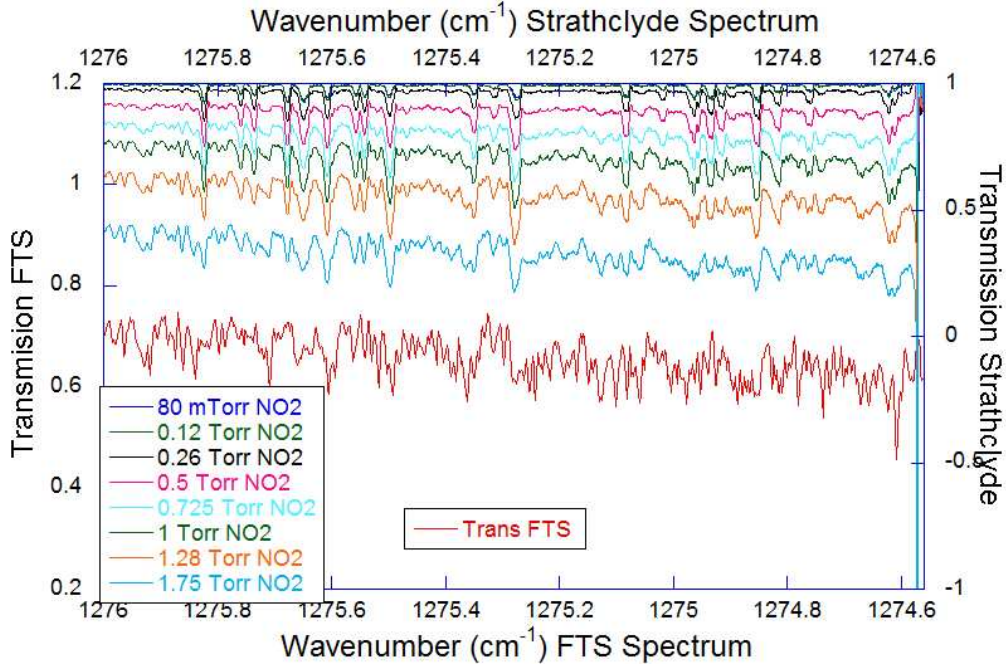


Fig. 4.50: Zoom in of figure 4.49 with features between the FTS and Strathclyde clearly matching.

In figure 4.51 the collisional damping of the system with Nitrogen shows that the dimer still persists at the pressure normally used in absorption cell gas analyzers, the heavy red trace. The fact that NO_2 readily forms its dimer, even at low pressures, may result in the concentrations of atmospheric NO_2 calculated when measured in the $6.14\mu\text{m}$ region giving a wrong reading. Most of the papers concerning the measurement of NO_2 or N_2O_4 make reference to a mathematical relationship between the partial pressures of the monomer and the dimer

$$K_p = \frac{p^2(\text{NO}_2)}{p(\text{N}_2\text{O}_4)} \quad (4.3)$$

where K_p is an equilibrium constant that has been calculated for temperatures ranging from 233.4K to 403.93K in [95] [96].

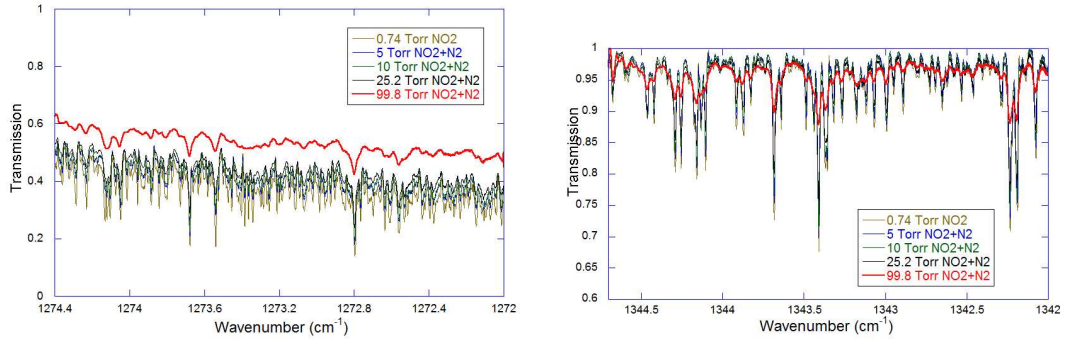


Fig. 4.51: Collisional damping of the $\text{NO}_2/\text{N}_2\text{O}_4$ system with N_2 recorded in two different regions.

In the Hepp paper [59] they go on to state that the partial pressure of the dimer can be calculated by

$$p(\text{N}_2\text{O}_4) = p(\text{NO}_2/\text{N}_2\text{O}_4) + \frac{K_p}{2} - \sqrt{p(\text{NO}_2/\text{N}_2\text{O}_4)K_p + K_p^2/4} \quad (4.4)$$

Where $p(\text{NO}_2/\text{N}_2\text{O}_4)$ is the total pressure in the cell. This can be then used to find the partial pressure of the NO_2 by substituting into the simple relation that the total pressure is the sum of the partial pressures,

$$p(\text{NO}_2/\text{N}_2\text{O}_4) = p(\text{NO}_2) + p(\text{N}_2\text{O}_4) \quad (4.5)$$

If these equations are used for the data recorded at Strathclyde a room temperature sample with a total pressure of 0.2 Torr would yield a partial pressure of N_2O_4 of 0.11 Torr. This goes up to 1.11 Torr for a total pressure of 1.75 Torr, which would mean that if this was not being taken into account when measuring NO_2 concentrations then it may be the case that detection systems based on lasers operating between the ν_9 and ν_{11} bands of N_2O_4 that do not compensate for this will be giving concentrations far less than the actual concentration.

Fourier transform spectra used in this section were reproduced with kind permission of J. Vander Auwera for the sole purpose of identification of N_2O_4 .

4.5 Effect of New Power Supply on Line-Shape When Recording High Resolution $^{14}\text{NH}_3$ and $^{15}\text{NH}_3$ Spectra

Two of the lasers in the Strathclyde lab are a matched pair operating in the $6.15\mu\text{m}$ region, that is they were grown and cleaved from the same sample and have a similar response. As part of the connection with the spin out company, Cascade Technologies, the group received some new equipment. Part of this was a new drive box that has redesigned circuitry that smooths the current pulse and reduces ripple bleeding through to the laser. The lasers themselves have a slower chirp than the other lasers in the lab with a chirp rate in order of 8MHz/ns at the end of the current pulse. With the laser frequency changing at this slow a rate the line-shapes approaches a Gaussian profile at low pressure.

The laser used for the previous experiments was the $6.15\mu\text{m}$ laser 62 which displayed a flattening of line-shape at its slowest chirp rate, figure 4.52. This flattening of the ${}^r_8\text{Q}(9,2)$ line of NH_3 in the spectrum where the laser is at -30°C and when the laser frequency is changing at 7MHz/ns is attributed to the instrumental broadening from the power supply. There is even distortion on the ${}^r_6\text{Q}(6,0)$ line, where the line appears to suddenly broaden as the laser scans through the red side of the line.

The electronics of the new power supply had extra smoothing designed to reduce over-shoot at the start of the current pulse and drop-off as the pulse progresses, this should reduce any effects of current pulse distortion on the laser. The current over-shoot at the beginning of the laser pulse can sometimes cause the frequency to up-chirp slightly in the order of 0.1cm^{-1} . At the end of the pulse there is a slight drop in the current through inefficiencies in the electrical components of the drive box, any drop in the current applied to the laser can cause variations in the laser power resulting in distortion of line-shapes. Any distortion of line-shape will become increasingly visible as the chirp-rate slows. Hence as the $6.15\mu\text{m}$ lasers, laser 61 and laser 62, have chirp-rates in the order of 10MHz/ns at the end of the pulse they are the obvious choice for determining if effects from the drive circuits are bleeding through to the laser beam.

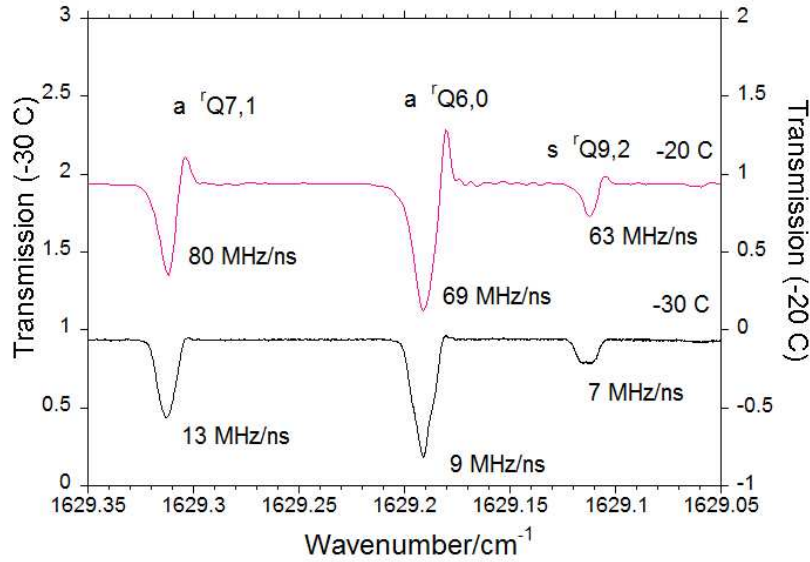


Fig. 4.52: Comparison of rapid passage line-shape of part of the Q-branch of the ν_4 band of $^{14}\text{NH}_3$. The overlap region of two different laser temperature settings with chirp rates shown, gas pressure was 3 mTorr. From [97]

At the time of performing the experiments laser 62 was in storage, laser 61 was mounted in a head and it was decided to use this instead of swapping it out with laser 62 due to time constraints. During the initial characterization of the laser by previous student K. Hay [29] it was noticed that there was a problem with laser 61 in that it was displaying bistability. This manifested itself, at the time, as an uncertainty in which wavelength the pulse started and the ratio at which the different modes the laser operated at. These varied with laser temperature and pulse length, with one mode becoming more dominant at lower temperature. With this in mind part of the test was to determine if this could be rectified or at least whether it would be possible to pick out the more dominant mode. During testing of the laser there was no sign of this bistability, it is likely that the second mode was exiting the front facet of the device at a different angle from the main mode and by adjusting the lens in the front of the head the second mode could be blocked.

With this adjustment the laser appeared to operate at a single mode and it was deemed to be performing sufficiently well to allow it to be used for spectroscopy.

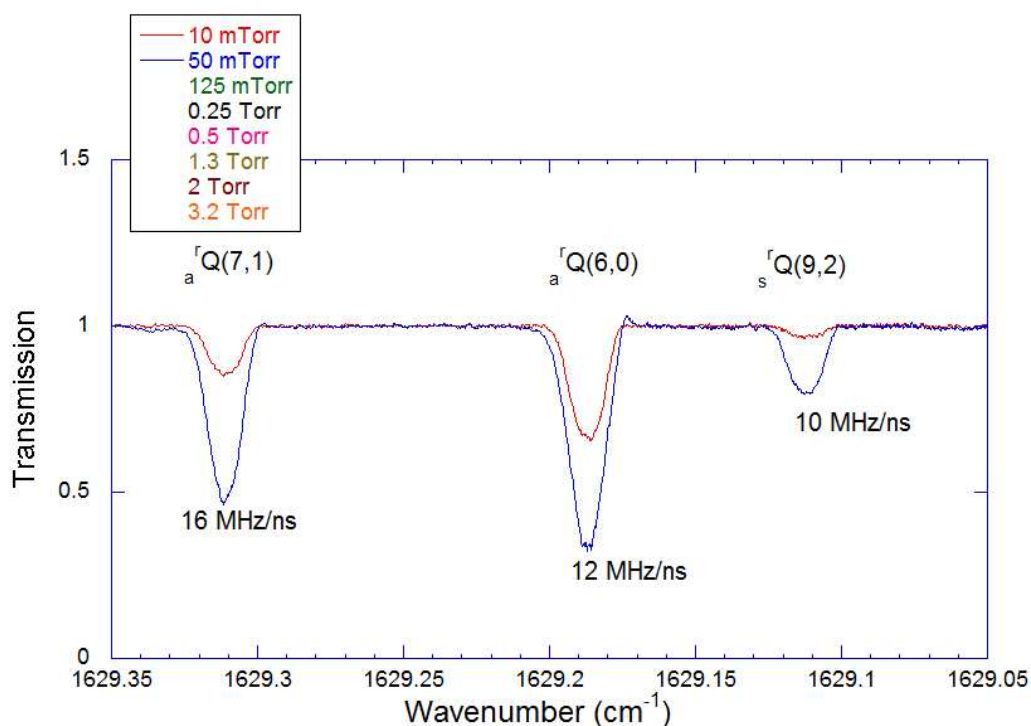


Fig. 4.53: Q-branch region of ν_4 band of $^{14}\text{NH}_3$ recorded using Laser 61 at -30°C

The first step was to repeat the original experiment, the laser settings for the laser 62 work were pulse length of $2\mu\text{s}$, repetition rate of 5kHz and voltage of 8.5V . However due to the lens adjustment required to filter out the unwanted mode the weakness of the signal through the cell meant the lowest operational voltage that gave an acceptable signal was 9V . As an example of the effect a very small change in laser setting can have on the laser performance figure 4.53 shows the same region featured in figure 4.52. The only difference between the two spectra is the 0.5V difference in laser voltage, this manifests as a difference of chirp rate. Although there is a small difference in the chirp rates, $\approx 3\text{MHz/ns}$, this is not sufficiently different that the line-shape will be distorted.

On close examination of the $r_a Q(6,0)$ line in figure 4.53 it appears that this line is displaying a flattening of the "peak". This is merely a combination of the reduced laser power going through the cell, the averaging done by the DAQ card and the process of calibration of the spectrum.

When comparing the $r_s Q(9,2)$ line in both figures 4.52 (laser at -30°C) and 4.53 it appears that the new power supply does indeed reduce the effects of unwanted current variations bleeding through to the laser. The new circuitry components within the drive box also improved the temperature control, often the actual temperature can vary slightly from the set temperature. When the laser is operating at either end of the allowed temperature range (-30°C to $+45^\circ\text{C}$) heat extraction is not as efficient or as responsive as when operating at mid range (0°C). This shows as a slight increase, $\approx 1^\circ\text{C}$, in the temperature displayed by the control software over the set temperature. This small variation does not result in any real effects when recording spectra, it is only problematic at the higher end of the scale but the control software only permits a maximum temperature of $+45^\circ\text{C}$ whereas the lasers are capable of operation as high as $+50^\circ\text{C}$.

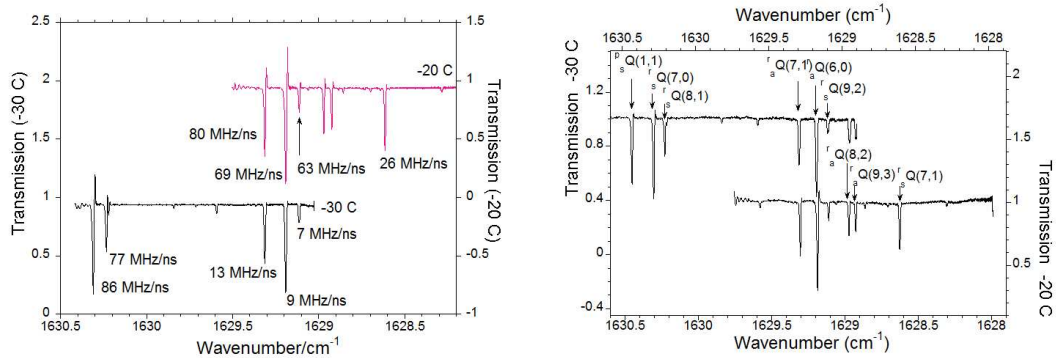


Fig. 4.54: Comparison of the spectra where the laser is at -30°C and -20°C . Left was recorded using laser 61 with older drive box, right using laser 62 with new drive box.

In figure 4.54 where the laser is at -30°C and -20°C the spectra in the right plot were recorded using the new drive box and laser 61, as it matched with laser 62 its response is almost identical. However comparing these spectra with the spectra of corresponding temperature recorded previously with laser 62, left of figure 4.54, it is obvious that there is an extra absorption line in both the spectra where the laser is at -30°C and -20°C . In fact with the new drive box and laser 61 the spectrum with the laser at -30°C starts 0.17 cm^{-1} before the spectrum from laser 62, with the ${}^P_5\text{Q}(1,1)$ line becoming visible at the start of the pulse.

Also in the newly recorded spectrum with the laser at -20°C the weak feature at 1629.356cm^{-1} is visible due to this spectrum starting 0.23cm^{-1} before the laser 62 spectrum. Even with any variations in the manufacture of the devices, both devices were grown from the one sample, it does not explain the difference in the frequency at the start of the pulse. As the extra 0.5V applied to laser 61 would result in the pulse starting at a slightly lower wavenumber, this means this can be disregarded as a cause for the observed difference. This leaves improvements in the temperature control circuitry as the only explanation for the difference in starting wavenumber, i.e. the combination of the new drive box and laser 62 resulted in the laser substrate temperature being very close to the set temperature. Only a lowering of temperature results the start of the pulse being at a larger wavenumber.

As the laser was functioning sufficiently well in combination with the new drive box at lower temperatures it was decided that a comparison of ${}^{14}\text{NH}_3$ and ${}^{15}\text{NH}_3$ would be a useful exercise. The ${}^{14}\text{N}$ nucleus has integer nuclear spin whereas the ${}^{15}\text{N}$ nucleus has spin $\frac{1}{2}$, both of the isotopologues have statistical weights of $K_a=4$ and $K_c=2$ [98]. It is projection of $\mathbf{I} = \frac{1}{2}$ onto the main axis of rotation that results in $\Delta\mathbf{J} \neq \Delta\mathbf{F}$, this manifests as extra transitions and differences of intensities compared to ${}^{14}\text{NH}_3$.

Figure 4.55 shows ${}^{15}\text{NH}_3$ and ${}^{14}\text{NH}_3$ spectra recorded using the same laser settings as previously used for the ${}^{14}\text{NH}_3$ comparison between the laser 62 and laser 61 spectra. Transition due the ${}^{15}\text{N}$ atom's nuclear spin are clearly visible, i.e. the strong ${}^P_5\text{Q}(3,1)$ line at 1629.85 cm^{-1} . Other lines visible, marked with u, are undefined as yet, the ${}^{15}\text{NH}_3$ isotopologue has had little work carried out in the mid-infrared, work done by Di Lonardo *et al.* [99] and Cottaz *et al.* [100] have been used for identification of lines. Other work in ammonia uses the ${}^{15}\text{N}$ isotopologue of ammonia for biomedical uses, eg. as a tracer [101], and for NMR studies [102] as it gives sharper lines.

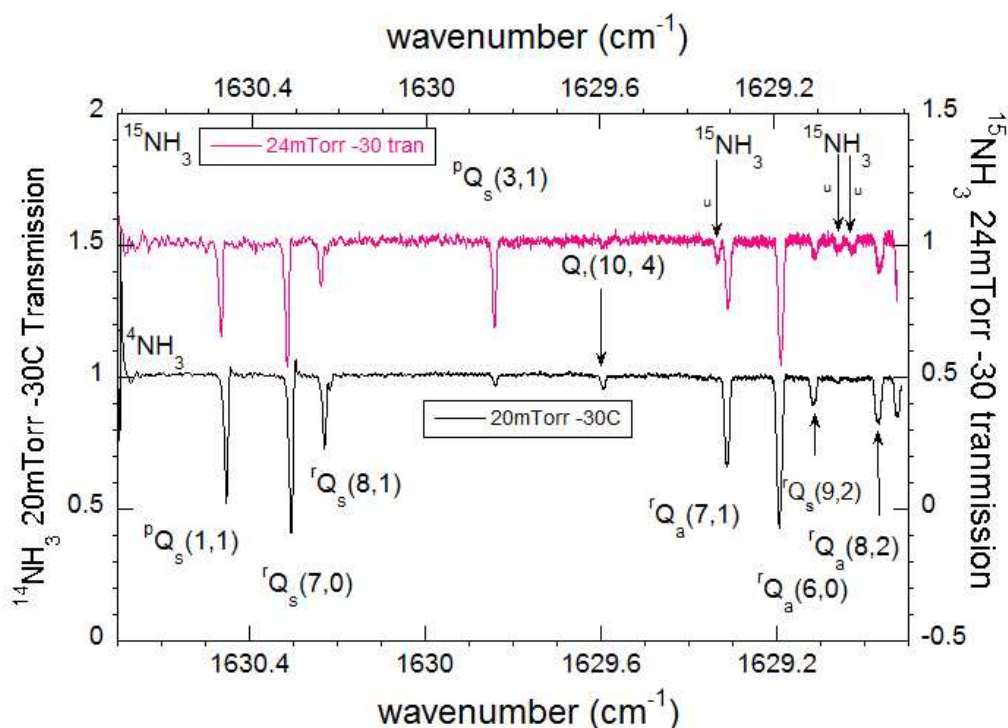


Fig. 4.55: Comparison of Q-branch of the ν_4 of $^{15}\text{NH}_3$ and $^{14}\text{NH}_3$ spectra with laser temperature at -30°C

The temperature range set by the control software lets the $6.15\ \mu\text{m}$ laser used, laser 61, cover a wavenumber range of $1621.5\ \text{cm}^{-1}$ to $1630.7\ \text{cm}^{-1}$. In order to obtain spectra covering this wavenumber range the laser can be temperature tuned in small steps, by starting at -30°C and increasing in steps of $+5^\circ\text{C}$. Each temperature step would normally require the cell to be evacuated, a background taken (this allows the DAQ card to normalize the signal from the detector and give a transmission spectrum), and to record a new etalon fringe pattern (allows the recorded time domain spectrum to be calibrated and converted into the frequency/wavenumber domain). Doing this requires great care in ensuring the gas pressure is the same for each temperature step. Unfortunately the supply of $^{15}\text{NH}_3$ available to the group was very limited.

So as a get around the cell pressure was set and the temperature increased in steps of $+5^{\circ}\text{C}$ with a spectrum recorded for each step, after this was completed the cell was evacuated and the temperature steps reversed with laser signal (through empty cell) and etalon fringes recorded. The acquisition LabView routine records both the averaged detector signal as well as the normalized signal from the ACQiris AP200 DAQ card, by using the averaged signals of laser signal with gas present in the cell and those with the cell empty it is possible to perform the normalization in post analysis. While doing the temperature range spectra absorption of atmospheric water at 1627.83 cm^{-1} , 1623.56 cm^{-1} and 1622.60 cm^{-1} resulted in sections of total absorption, ammonia lines in these regions are therefore not visible or only the peaks of strong transition features are visible on the wings of the water absorption.

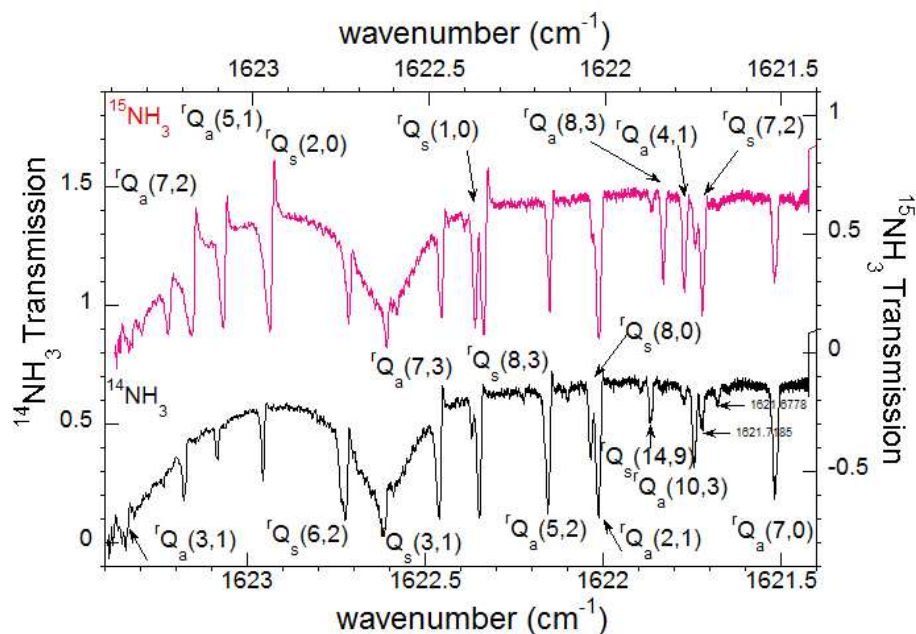


Fig. 4.56: Comparison spectra of $^{14}\text{NH}_3$ and $^{15}\text{NH}_3$ at cell pressures of 240 mTorr for each spectrum, laser temperature set at $+45^{\circ}\text{C}$, water lines are clearly visible at start of pulse

In figure 4.56 $^{14}\text{NH}_3$ and $^{15}\text{NH}_3$ spectra recorded with the laser temperature at the highest allowed setting of $+45^\circ\text{C}$ at a pressure of 240mTorr both show absorption of water. The wing of the 1623.55914cm^{-1} line is visible at the start of the pulse and the 1622.59773cm^{-1} can be seen overlapping the ${}^r_s\text{Q}(3,1)$ transition in the $^{14}\text{NH}_3$ spectrum. Line identifications of the $^{15}\text{NH}_3$ spectra are ongoing.

It should be noted that lines that feature in both the $^{15}\text{NH}_3$ and $^{14}\text{NH}_3$ are likely to be $^{14}\text{NH}_3$ with the lines associated with $^{15}\text{NH}_3$ only marked as such.

4.6 Conclusion

As a tool for high resolution QC lasers have been proven a useful replacement for lead salt devices as they do not require LN₂ cooling. The relatively large spectral window associated with long current pulses allows the detection, if present, of several different molecular species. However the non-linear nature of the fast frequency down-chirp results in distorted line shapes with rapid passage and free induction decay signals. This can be reduced or eliminated by the addition of a buffer gas that does not absorb in the same region as the molecule of interest, commonly by the addition of N₂ although other buffer gases have similar or better damping effects N₂ is the most common gas present in the Earths' atmosphere and provides a useful comparison to many portable spectrometers used to monitor pollutants.

The damping of the rapid passage signals of N₂O and of NO show a similar response to each gas chosen as a buffer this is most likely due to them both being linear molecules. CH₄ on the other hand has a tetrahedral structure, it is a spherical top, and although the rapid passage signals are quenched when ≈ 25 Torr of buffer gas is added the broadening of the absorption features is not as pronounced compared to that of N₂O and NO. It is the apparent shift in the absorption lines of CH₄ when buffered with Helium. This is most likely due to collisions changing the bond lengths within the molecule thus changing the vibrational frequencies.

Although there was difficulties when performing collisional experiments on NO, due to the construction of the White cell, the evidence of a chirp related effect visible in the spectra was an unexpected bonus. At first it was believed to be an artifact of the system but at higher pressures the rapid passage signals vanished whether it was buffer gas or pure NO causing the broadening. It seems this effect was a result of a standing wave forming in the White cell acting as a pseudo pump-probe.

The dimerization of NO_2 into N_2O_4 is a process that is taught to chemistry students around the world. However it was believed that this process occurred in samples of NO_2 at pressures close to atmospheric pressure. It has been shown that this process occurs at pressures as low as 0.1 Torr, this is made possible by the long path length of the Herriott cell in the Strathclyde University laboratory. Similar systems for gas detection using absorption spectroscopy, for example the Cascade Technologies CT2400 and newer systems, use a similar path length. At present it may be the case that absorption spectrometers used for gas detection do not take into account for the dimerization, due to industrial confidentiality companies are unwilling to divulge this information. As NO_2 is a by-product of the breakdown of explosives an accurate detection method is important. As the dimer forms at low pressure and remains visible when 100 Torr of N_2 is added Herriott cell, this is the pressure Cascade Technologies use in their spectrometer Herriott cells, then it must be compensated for when calculating concentrations of NO_2 detected.

The NH_3 experiments were carried out at the very end of the experimental work contained in this thesis and at the time of writing the analysis of the spectra was being performed by G. Duxbury and still in the early stages. With this in mind figures 4.55 and 4.56 already show newly identified absorption lines associated with $^{15}\text{NH}_3$ that have not been reported in the literature at present.

5. SET-UP AND TESTING OF A CW QCL FOR USE IN A HIGH SPEED SPECTROMETER

As part of our collaboration with the spin-out company Cascade Technologies we received , on loan, a Distributed Feedback Continuous Wave (DFB-CW) QC laser with a centre wavelength of ca. $7.77 \mu\text{m}$. This was to determine the feasibility of constructing a CW-QC laser based spectrometer working in the $8 \mu\text{m}$ region as most other CW-QC laser systems work in the $5 \mu\text{m}$ region. The narrow line-width of the CW-QCL laser could result in a spectrometer with greater resolution than a pulsed QCL, however the scan rate may be slower. Engineering doctorate(Eng D) student Robert Campbell had begun working with Cascade Technologies, as the industrial partner of the postgraduate scheme, to work with the CW laser. When it was decided the laser testing should take place in our lab, we had the extra space and equipment needed, Robert joined us at Strathclyde University. The initial testing and characterization was performed in collaboration with Robert. All other experimental work was performed whilst he was away from the lab.

The laser device was manufactured by Alpes Lasers, Switzerland and was mounted in a modified Cascade Technologies LS-03-D system developer head, the developer head is designed for use with pulsed QC lasers so in order for a CW laser to be operated the electronics required to be altered. This meant the head could not be evacuated and back filled with nitrogen and therefore the temperature of the laser could not be taken below the dew point of water as this would damage the device. Instead of the standard control module that forms part of the LS-03-D laser system the temperature and current control required separate control devices, again due to the change in electronics. The temperature controller used was an ILXLightwave LDT5980 High Power Temperature Controller and the current controlled by an ILXLightwave LDX3232 High Compliance Current Source

During initial testing it was noticed that after extended periods of operation the temperature readout on the controller would climb indicating that Peltier cooler was having difficulty cooling the laser device. To solve this the fan assembly on the rear of the developer head was replaced with a water cooler.

This improved the temperature stability of the laser although when changing the temperature setting it still required time for the displayed temperature to stabilize.

5.1 *Initial Testing*

Unlike the pulsed lasers that tune due to the heating caused by the applied current pulse, the CW-QC laser tunes by increasing current with an external ramp applied to the current source by a signal generator. However like the pulsed lasers the substrate temperature defines the starting frequency of the scan. It is possible to operate a CW-QC laser in pulsed mode in the same way as the pulsed QC lasers are driven but this was not part of the project and was not tried. The main difference between the pulsed and CW QC lasers is the output power. A pulsed QC laser commonly operates from as low as 0.1 mWatt to a few milliwatts, high power pulsed QC lasers are beginning to become available from manufacturers such as Alpes Lasers and Hamamatsu with output power of up to 600mW, on the other hand the CW-QC laser power increases with the current applied. The power of the of the CW laser ranged from 0.1 mW at threshold to over 240 mW. This maximum power comes from the laser specification data supplied by the manufacturer (figure 5.1), as we could not cool the laser below 4°C the maximum power output we could achieve was in the order of 160 mW. The data sheet states the device can operate up to 50°C but as we previously had problems with temperature stability we decided not to operate above 35°C to reduce the chance of damaging the device.

As per the specifications sheets the power output of the laser increases with the current applied with output power in the order of 245 mW for a current of 730 mA and laser temperature of -20°C. However these values would have been achieved under ideal test conditions and as the laser was mounted in a modified developer head it was sensible to perform our own measurement of the power for increasing currents not only for a confirmation of the output but as an indication of the safety protocols needed.

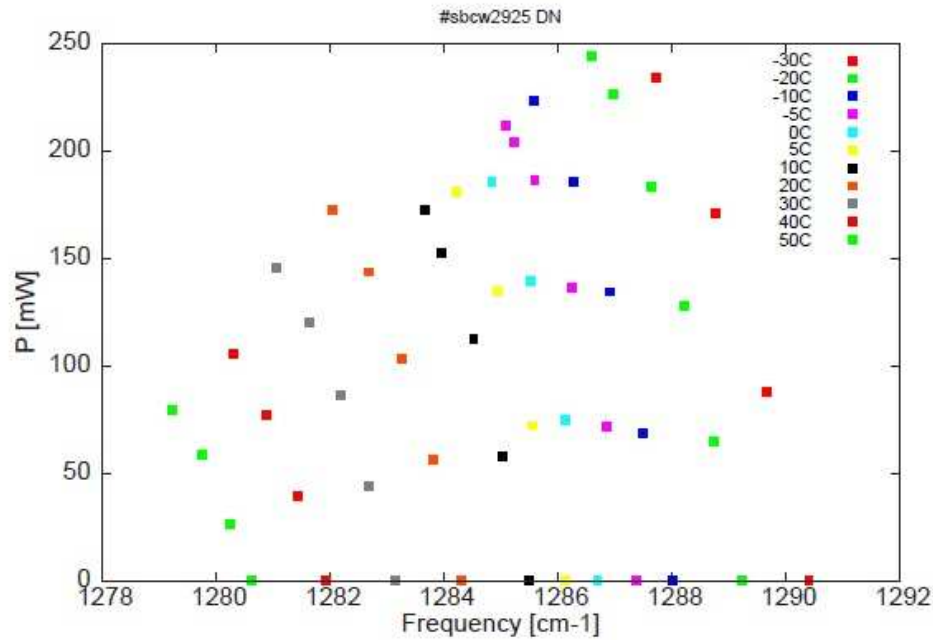


Fig. 5.1: CW-QC laser power against current taken from manufacturers data sheet.

The first test was performed with only the Peltier cooler controlling the laser temperature, temperature set to $+20^{\circ}\text{C}$, this only gave output powers half of those listed in the specifications sheets. Next was to repeat with the cooling fan in the developer head running, results of this test are shown in figure 5.2. The power meter used was an OPHIR ORION-TH-ROHS with an OPHIR 3A-SH-ROHS detector element.

Even with the fan running the power output of the laser was substantially less than the manufacturers specifications. This can be attributed to several factors such as the collimation optics at the front of the developer head was in need of adjustment, it was possibly causing beam dispersion, the detector element of the power meter could have been overheating, lack of heat dissipation from the detector could give incorrect readings, the not-quite linear plot of power versus current in figure 5.2 could be indicative of this. It was during this time that the heat extraction problem started to be noticed.

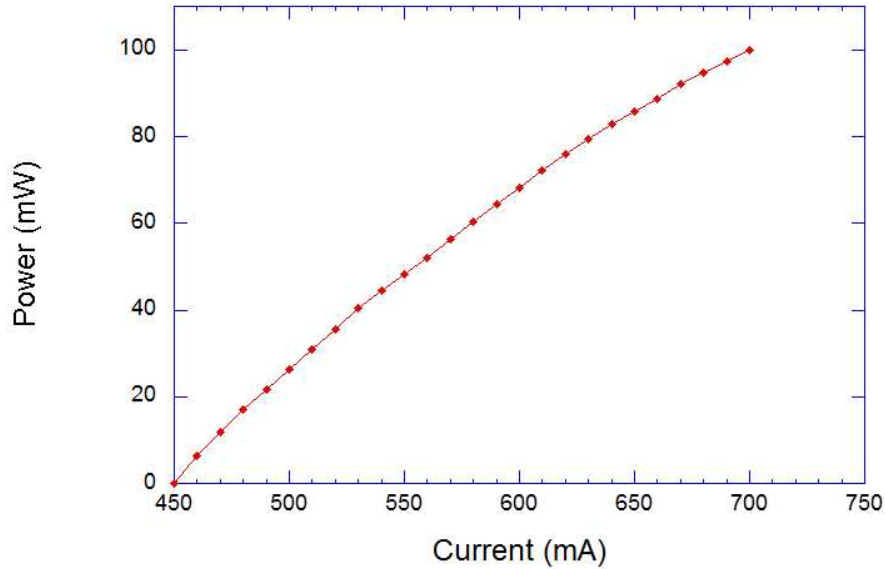


Fig. 5.2: Power v's current for CW-QC laser operating at +20°C.

As part of understanding the response of the device it was essential to know what wavenumber range it can be tuned over. To accomplish this the laser was used as the light source on our BOMEM FTS, the temperature set and the current applied increased in small increments starting from the threshold current up to a maximum safe operating current.

In figure 5.3 two of the temperature settings used for the tests, 15°C and 25°C, show that the tuning range of the laser is limited to a 2.5cm^{-1} window similar to the pulsed lasers. It was during these tests that the temperature stabilization issues became a severe problem with the laser temperature increasing from the set +20°C up to mid 40's, after only an hour operating time, before the laser could be safely shut off. This is the point when it became apparent that the Peltier/fan combination was not suitable for heat extraction and the water cooled attachment replaced the fan assembly on the developer head.

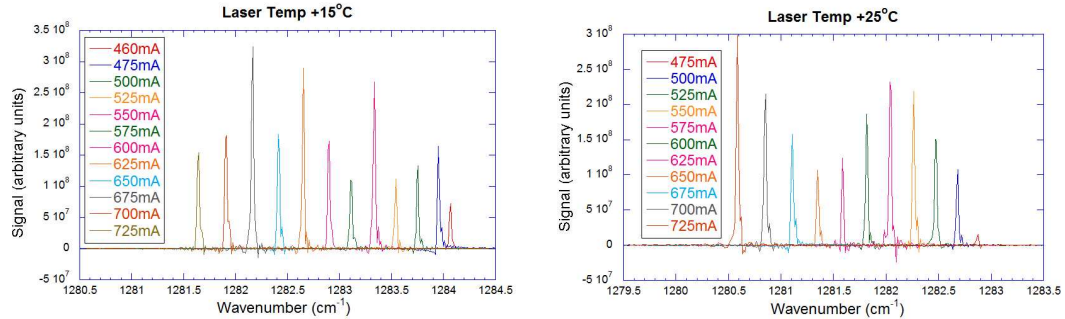


Fig. 5.3: BOMEM output for set temperature with varying current.

5.2 Laser drive and detector tests

After receiving and fitting the water cooled attachment the temperature stabilization problem reduced, but still did not respond well to large changes in the laser temperature, allowing prolonged use.

The laser was set so the power output was low i.e. the current close to the lasing current, this was to protect the Vigo detector. A chopper was placed in the beam to give an effective pulsed beam with a repetition rate of 20KHz, this gave a signal on the oscilloscope, Tektronix TDS 3.52, but the chopper was distorting the signal due to lack of uniformity of movement. Next was to modulate the current source by applying a sine wave, using a RS 610-635 2MHz signal generator. Placing an etalon in the beam showed the wavenumber scan range as well as any problems with the driving current, these would show as distortion in the fringe pattern.

Figure 5.4 shows the fringe pattern recorded with a Germanium etalon with a frequency spacing of 0.0195 cm^{-1} . By counting the peaks it is clear that the laser frequency is changing by $\approx 0.25 \text{ cm}^{-1}$ when a 1 KHz sine wave modulation is applied directly to the current source. A slower frequency modulation would allow the laser to scan over a longer frequency chirp, but when this was attempted the signal vanished from the oscilloscope. It was likely the detector was unable to 'see' this slow change in the laser frequency. The Vigo detectors we use are coupled to an alternating current pre-amplifier, designed to detect high repetition pulsed signals.

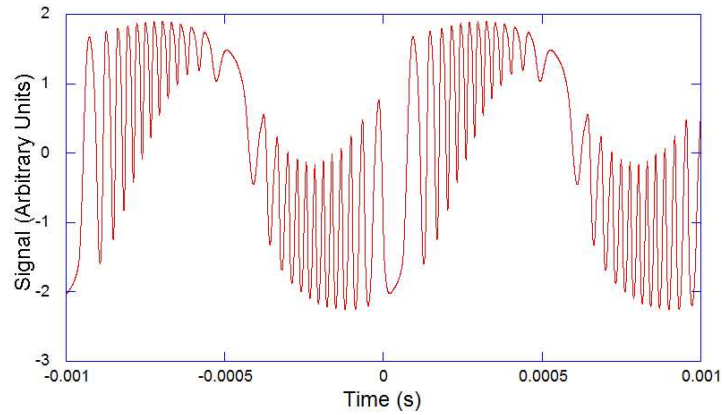


Fig. 5.4: Etalon fringe pattern when 1 KHz sine wave modulation was applied to current source.

Further tests on the modulation found that by increasing the amplitude of the modulation and changing to a triangular waveform the modulation frequency could be increased to 10 KHz and still give a spectral window of 0.4 cm^{-1} .

The spectrometer setup used for atmospheric pollutants measurements on the NERC ARSF (National Environmental Research Council, Airborne Research & Survey Facility) plane [6] was re-used as it allowed the use of a pulsed QC laser as well as the CW-QC laser. It made sense to re-use this spectrometer as its portable nature meant it could be easily moved into position for use with the CW laser, the multi pass cell (path length of 72m) and mounted mirrors were still in alignment with the green alignment laser and the pulsed QC laser that could be attached to the spectrometer and by adding a small plane mirror and a knife-edge mirror the CW beam could be made to co-propagate with the pulsed QC and green lasers. The He-Ne laser was set to co-propagate with the CW-QC laser so when the spot patterns from both alignment lasers, visible on the rear mirror of the cell, matched it meant that both infrared beams were traveling the same path. Figure 5.5 show a schematic of the CW-QC laser in relation to the spectrometer.

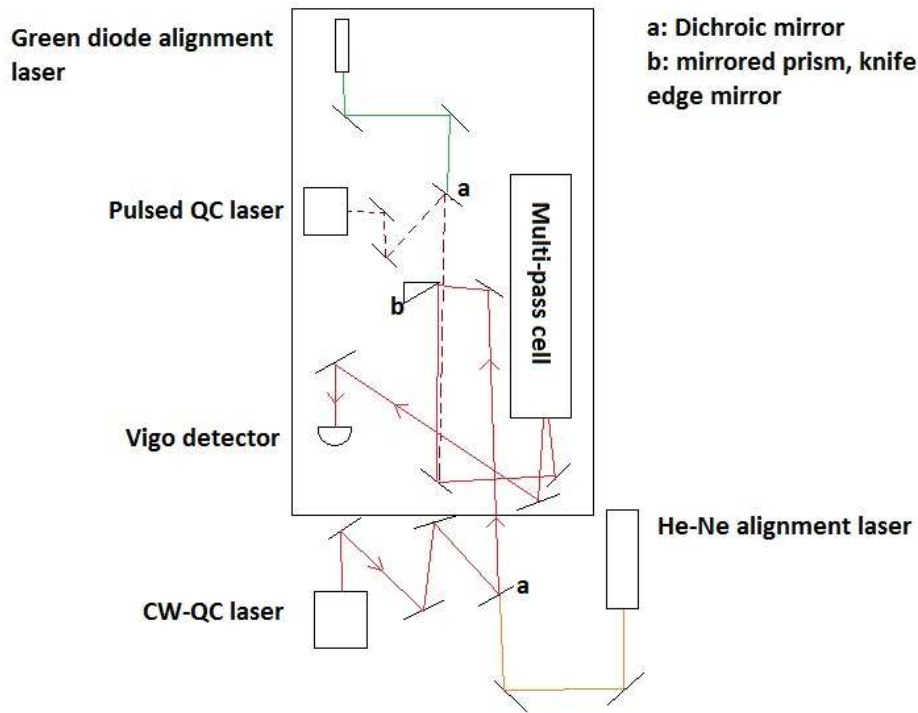


Fig. 5.5: Schematic of the CW-QC laser and pulsed QC laser spectrometer (outline shows the original spectrometer). The knife edge mirror (b) and the plane mirror opposite were added to make the CW beam co-propagate with pulsed beam.

Once the CW-QC laser was going through the cell and giving a detectable signal work was focused on driving the laser in order to maximize the spectral window scanned through. Cascade Technologies were interested in how a second harmonic ($2f$) spectra recorded through a lock-in amplifier compared in sensitivity with their pulsed QC laser spectrometers.

Before using the lock-in amplifier it was required to check if the longer path length had any measurable effect to the etalon fringe pattern recorded.

The fringe pattern in figure 5.6 was recorded with the beam passing through the cell and when compared with the fringes in figure 5.4 it is clear that there is noise on the signal. As we knew the beam was dispersive the first thought on the source of the noise was the laser power falling on the detector.

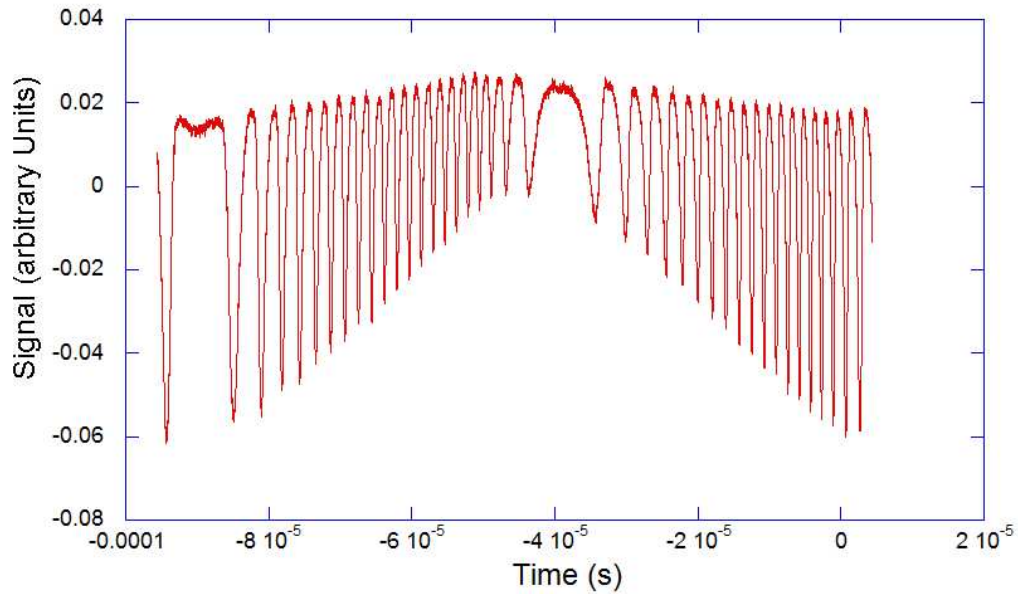


Fig. 5.6: Etalon fringe pattern with beam traveling through multi pass cell (the negative values on the time axis is purely due to oscilloscope settings).

The power meter detector was used to measure the power of the beam as it left the cell and as the beam fell onto the Vigo detector, both gave an average reading of $50 \mu\text{W}$. A zinc selenide lens was placed in the CW beam before it reflected off the dichroic mirror and this improved the power reaching the Vigo to an average of $64 \mu\text{W}$. With the lens in place the noise was markedly reduced. This drop in power did not pose a problem as it meant the beam did not require any attenuation and did not saturate the detector, this can cause the detector element to burn out if excess power falls onto it for extended periods of time, see figure 5.7.

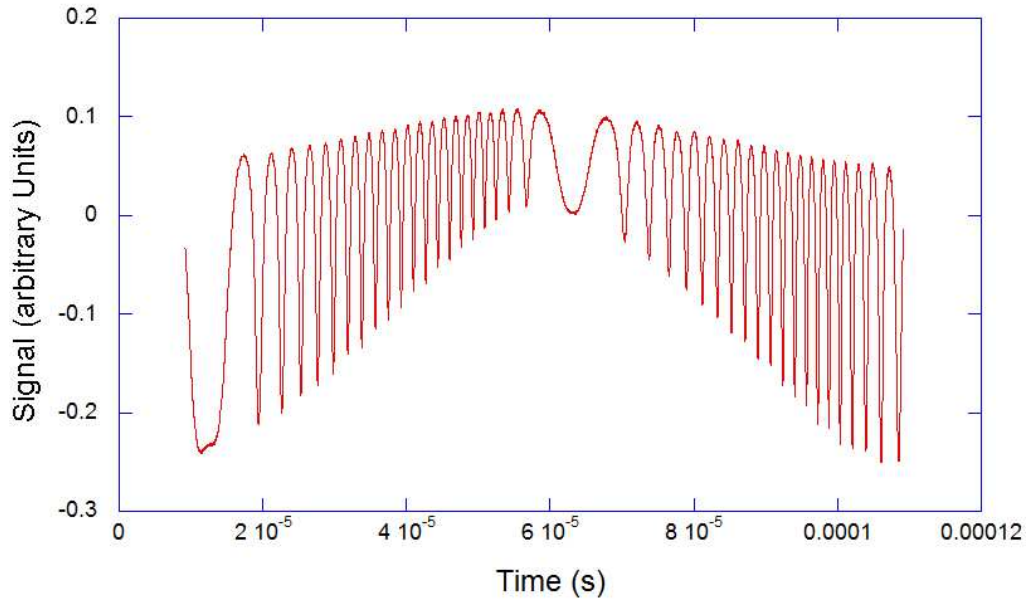


Fig. 5.7: Etalon fringe pattern recorded with ZnSe lens in place.

When comparing the etalon fringe patterns in figures 5.6 and 5.7 it is clear that the lens is helping in collimating the beam. The spacing of the fringes are equal in frequency space but they vary in temporal space with the changing chirp rate of the laser, even with only a small number of fringes it is clear that the CW-QC laser chirp has a more linear response over the pulsed lasers. The triangular wave function applied to the current source caused an increase in the current of ≈ 50 mA and with the laser temperature at $+20^\circ\text{C}$ the current for the start of the ramp was set to 600 mA. N_2O was added to the cell and by varying the starting current spectral features could be scanned through.

As the start current reached 615.6 mA a singlet and a l -type doublet were visible on the oscilloscope screen. These were initially identified as the singlet $\text{P}(4)_e$ and doublet $\text{P}(11)_{e,f}$ lines of N_2O [76]. It turned out that the oscilloscope was set incorrectly.

When this mistake was noticed the singlet was properly identified as the $P(3)_e$ (figure 5.8), it also showed that the resolution of the system, as it stood, was in the order of $\Delta\nu=0.00457\text{ cm}^{-1}$ as this is the separation of the l -type doublet.

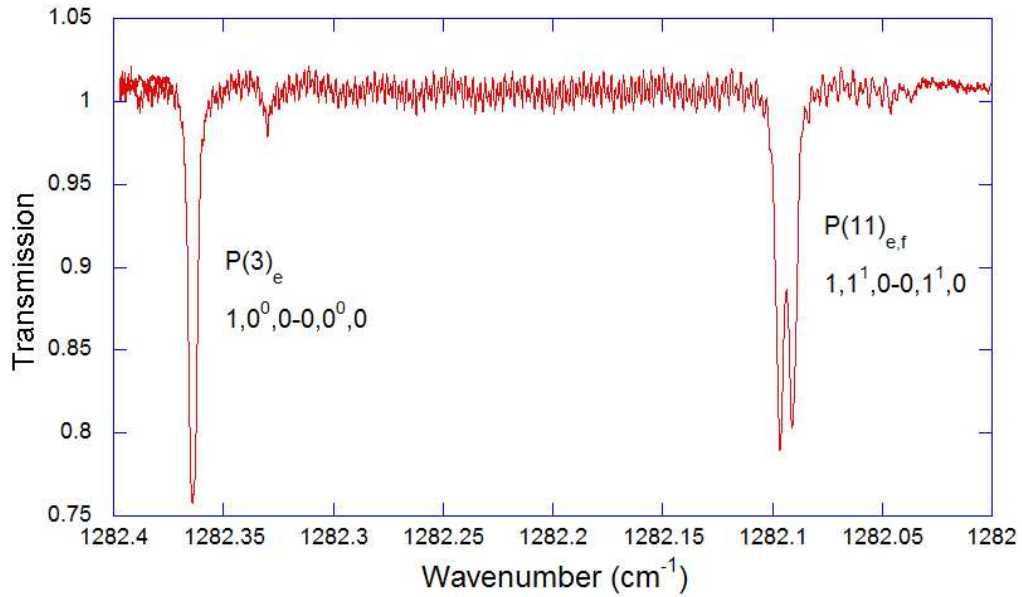


Fig. 5.8: Corrected calibration of CW spectra.

Although this method of driving the laser gave a near linear chirp and good resolution the spectral window was too small to be useful. Different frequency triangular wave functions were tried without any great effect on the spectra recorded. When it came to using the lock-in amplifier to obtain the second harmonic spectra it was realised that the Vigo detector may not be suitable as its response time of $\leq 7\text{ ns}$ could result in it being too fast to detect the laser signal, also the AC coupled pre-amp means the Vigo configuration is designed more for pulsed laser operation. Other groups using Vigo detectors for CW-QC laser measurements use them configured with DC coupled preamplifier, for example the Ritchie group at Oxford University [72] and the Martin group at Manchester University [103].

These two groups also use Daylight Solutions External Cavity CW-QC lasers that tune with changes made to the grating of the external cavity. As direct current modulation was being used to tune the CW-QC laser care must be taken to prevent exceeding the maximum safe current for the device, the ILXLightwave LDX-3232 allows for a maximum current to be set thus protecting the device, this was set at 700mA. Driving the laser for use with the lock-in would require a slow ramp with fast modulation superimposed onto it. The maximum safe current set on the current source would allow the length and magnitude of the slow ramp to be varied without causing damage to the laser. It was the combination of the detector configuration and the required slow ramp that made the detector not suitable. As with many research groups working in the infrared the group has liquid nitrogen cooled detectors, one of the LN₂ detectors we have, a Laser Monitoring Systems S-100 MCT(mercury cadmium telluride), has a slower response time than the Vigo. A mirror was added to the set-up in order to direct the beam away from passing through the multi-pass cell. This was for the safety aspect of filling the detector with nitrogen and not to disrupt the set-up for the beam going through the cell.

It was hoped that this detector would be able to detect a DC signal but this was not the case and it required the chopper to be placed in the beam before a signal was seen on the oscilloscope. One suggestion for a detection system was to use our 7.84 μm pulsed laser as a QWIP (Quantum Well Infrared Photodetector) [104]. This was discounted as it was realised that the operational wavelengths of the lasers were too far apart, also the diffraction grating on the front face of the pulsed QCL would only allow a single frequency to pass through.

After some debate it was decided to try a different LN₂ cooled detector, Kolmar KV104-0.1-A-3-S MCT detector, where the manufacturers confirmed it had a DC response. To pick out the DC signal it was connected to a Thurlby Thandar WA301 wide band DC amplifier. With this combination a DC signal was seen on the oscilloscope.

To gain better control the signal generator was changed to a Tektronix AFG 320, this signal generator has less noisy signal than the RS signal generator previously used and the ramp was changed to a saw-tooth wave function. This was first tried using the RS signal generator but the laser signal would drift and it was thought the heat extraction was unable to cope with the signal applied to the laser, i.e. the mark-to-space ratio of the saw-tooth function was too high. It turned out the RS was not generating a proper saw tooth function. Even using the Tektronix function generator the laser response meant that it was not lasing for roughly the first third of the current ramp, figure 5.11.

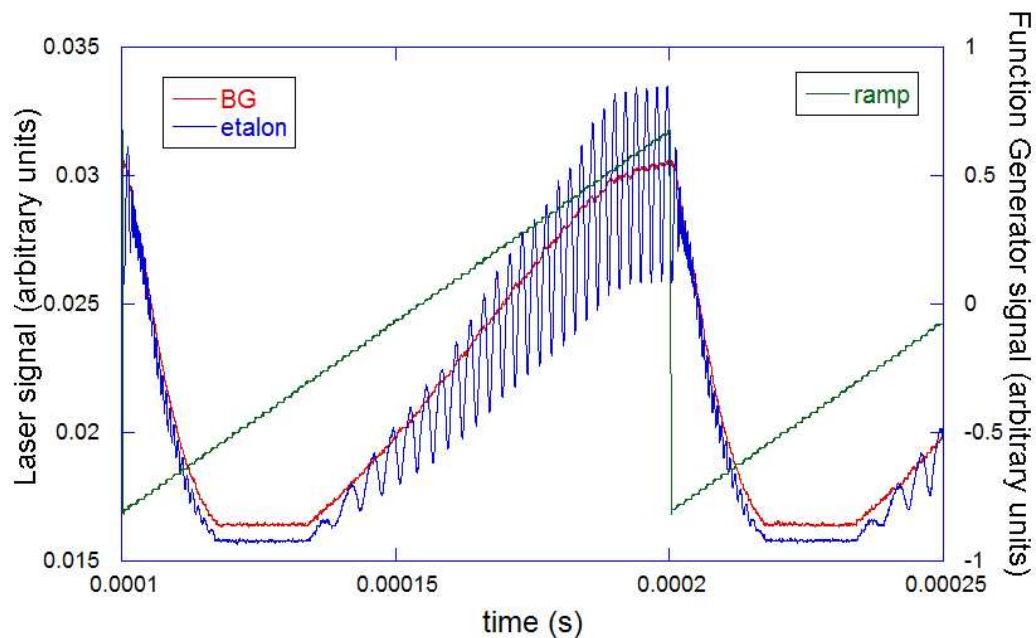


Fig. 5.9: Laser signal and etalon fringe pattern with saw-tooth ramp superimposed

The signals shown in figure 5.9 were the result of a fast saw tooth ramp, 10 KHz, and a starting current of 525mA. The initial current being above the threshold current, with the laser temperature at 20° the threshold current was ≈ 450 mA, meant the laser was not responding to the applied ramp as expected. This was believed to be due to the heat extraction that did not cause any drift in the laser frequency and the only way to improve this was to reduce the frequency of the applied current ramp. A saw-tooth ramp with frequency of 500Hz was applied to the laser as a first step to obtaining the second harmonic spectrum, this resulted in a longer scan and a spectral window of ≈ 0.8 cm^{-1} almost twice as much achieved with previous settings. Figure 5.10 shows the etalon fringe pattern recorded using the slower frequency ramp.

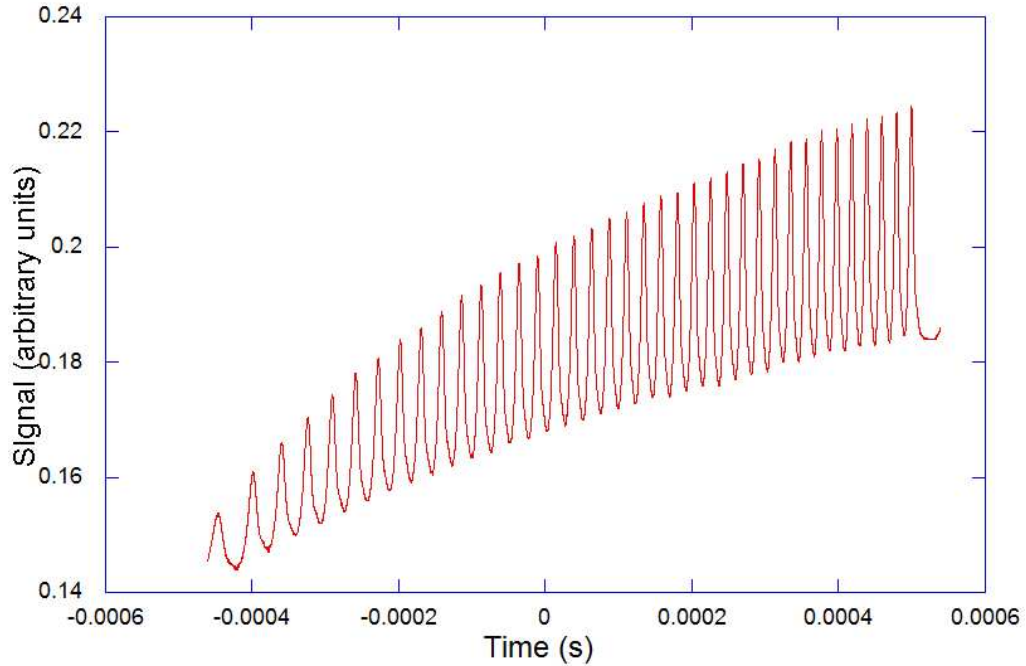


Fig. 5.10: Etalon fringe pattern obtained after changing the scan frequency to 500Hz. Recording the files were changed from saving by the oscilloscope (it has a built in floppy disc drive) to recording by a LabView routine through a GPIB-to-USB connection on a laptop.

It became clear that the frequency of the ramp played a greater effect on the driving of the laser than was expected. It turned out that the laser was responding better to a slower frequency current ramp to the extent that without changing the amplitude of the ramp the spectral window had doubled. Also it was noticed that the likely cause for the signal in figure 5.11 was that instead of the applied ramp starting at zero the wave function was oscillating about zero, i.e. when the laser current was set to start its scan at 525mA the applied 200mA ramp should have increased the current up to the maximum set limit of 725mA instead it was reducing the start current to 425mA. This explains what was seen in the graph, the laser was not lasing at the start of the ramp. The Tektronix function generator has the capability to offset the wave function applied and this rectified to problem.

The lock-in amplified requires a modulation of significantly different frequency to the slow ramp applied to the laser, added to the ramp so that this is filtered out. To add the fast modulation, generated by a Levell TG303, onto the ramp an in-house made analogue mixer mounted in a Biodata Microlink III was used. The resultant signal was then applied to the laser current drive box. Still using the Kolmar detector with the DC amplifier a Princeton 5209 lock-in amplifier was used in the first attempt to obtain the $2f$ signal. Instead of the saw-tooth ramp a triangular waveform was used as it was unknown how the laser would respond to the change in driving current. The temperature set at 14°C and the starting current at 435 mA, the threshold current for this temperature setting, ensured the device would not be overdriven and damaged. A 50 Hz triangular waveform with a 2.5 KHz sinusoidal modulation was the first combination tried without much success, possibly the frequency of the added modulation was too close to being a multiple of the ramp. The modulation frequency was then changed to 48.2 KHz but the lock-in was still unable to output a $2f$ signal. The ramp frequency was changed to 15 Hz with a modulation frequency of 23.5 KHz, this had the desired effect with the signal output from the lock-in becoming the recognizable fringe pattern when the etalon was in the beam. The etalon was replaced by a small gas cell, an aluminium Edwards vacuum system T-piece with wedged salt (potassium chloride, KCl) windows at each end of the straight section and a needle valve with a reducer (KF25 to KF12.5 for filling) on the 90° section, filled with 2 Torr of Methane giving a path length of 15 cm. By changing the ramp frequency to 4.5Hz and keeping the modulation at 23.5KHz the signal through the lock-in improved greatly.

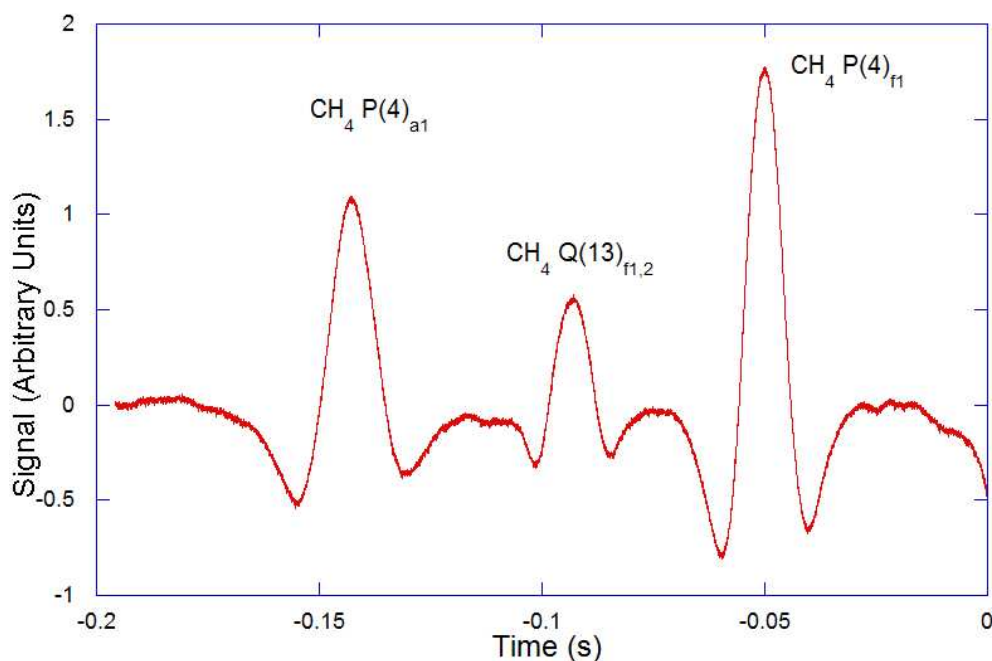


Fig. 5.11: Second harmonic signal of 2 Torr methane in a 15 cm cell.

The laser was set to 14°C and a starting current of 470mA corresponding to a wavenumber scan of $\Delta\nu \approx 1283.7 \text{ cm}^{-1}$ to 1282.7 cm^{-1} , the resulting signal obtained from the modulated ramp is shown in figure 5.13. The identification of the lines was troublesome at first as it was thought the Q(13) doublet lines should have been resolved and the intensity of the $P(4)_{f1}$ should be less than the $P(4)_{a1}$. The discrepancy in the intensities is most likely to be caused by the increase in laser power as its current ramps, i.e. power saturating the line. The Q-branch doublet being unresolved could have been due to a combination of factors, pressure broadening or over-modulation of the laser.

As it was now possible to obtain a 2f signal using the Kolmar/DC amplifier combination it was decided to have the beam passing through the multi-pass cell again. Before replacing it with the Kolmar detector the Vigo detector was tried to see if a signal was obtained. Surprisingly an etalon pattern appeared on the oscilloscope, the detector was picking up the fast modulation and must have been integrating it over the slow ramp. To check if the resolution was better than with the Kolmar, methane was added to the multi-pass cell and the settings changed to cover the ν_4 Q-branch in the 1285 cm^{-1} region, see figure 5.11. When compared to figure 5.12 the signal from the Vigo detector is much cleaner.

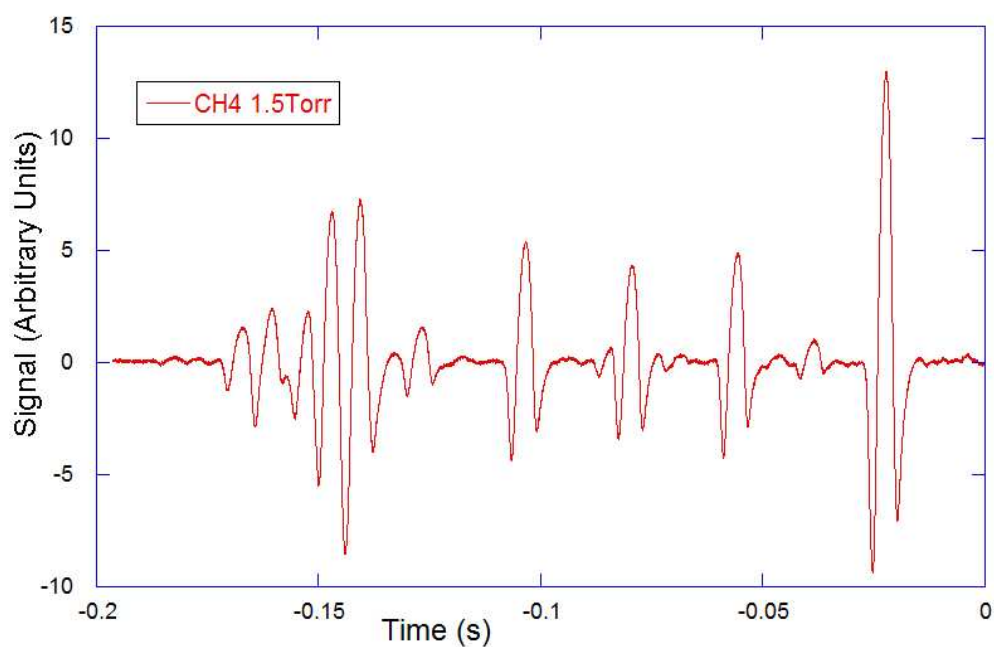


Fig. 5.12: Methane Q-branch recorded using AC-coupled Vigo detector with 2f signal produced by Princeton 5209 lock-in amplifier.

Since the second harmonic signal was now reproducible and with the benefit of having the Peltier cooled detector responding to the laser signal, improving the signal-to-noise and resolution became the new focus. The first step was to reduce the modulation frequency. The frequency of the modulation plays an important role in the shape of the spectral lines when generating a second harmonic signal. Slower frequency modulations give narrow lines but the feet are asymmetric, faster frequency modulation results in the feet being equal in size but the lines are wider and can form a 'belly' with loss of resolution in the system, there is a trade-off between resolution and line-shapes.

The Levell TG303 signal generator was removed from the set-up as the Tektronix AFG 320 has a two channel output with digital interface on each output meaning greater control of the modulation could be achieved. Both outputs still required to be added using the mixer. Keeping the saw-tooth ramp at 4.5Hz the modulation frequency was dropped to 1.69 KHz, chosen randomly as a suitably slower frequency than before. At this frequency the system was unable to give a 2f signal as the AC pre-amp connected to the detector was unable to process the signal meaning the lock-in amplifier was unable to pick out the modulation. By slowly increasing the modulation frequency it was found that the best resolution we could achieve was with a frequency of 2.69KHz.

5.3 Long Path Tests

Once the laser operation was controllable attempts were made for measurements of Nitrous Oxide, as Cascade Technologies had expressed an interest measuring N_2O in the atmosphere. First step was to use a pure sample of gas in the multi-pass cell in order to identify spectral lines and the settings required to scan through them. The main problem was evacuating the cell and maintaining low pressures as the only pump that could be connected to the cell was a dual-stage oil filled rotary pump, a Leybold D4B. The cell itself was designed primarily for gas flowing through at a steady rate, originally 100-150 Torr, rather than to hold a vacuum of a few mTorr. This meant that even though the Leybold pump could only get the cell down to 0.5 Torr the pressure would slowly increase as air would leak into the cell. This turned out to have an easy fix in that by simply resetting the seals for the cell ends and the pressure gauge greatly improved the vacuum tightness. Work had also begun on fitting an Edwards EXT70 turbo molecular pump onto the vacuum system. This required custom made connectors to be manufactured to house a butterfly valve between the inlet of the pump and the cell.

With the inability to cool the laser below the dew point of water the only lines of the ν_1 band of N_2O that were covered were the $\text{P}(2)_e$ and the $\text{P}(3)_e$ lines, however with the laser temperature set to 21°C and the start current at 480mA two l -type doublets and the $\text{P}(2)_e$ were covered in the same scan, figure 5.13.

With N_2O spectra recorded these could be used as a comparison to atmospheric samples, as part of the aim Cascade Technologies gave was to have air flow through the cell at a pressure of 50 Torr. The lab at Strathclyde University is on the top floor of the Physics Department giving easy access to the roof where a hose that allows sampling of the city atmosphere is fitted. In preliminary tests signals, although weak, were detected however they were not in the same part of the laser scan as expected. The first thought was that the temperature stability problem had returned but fortunately this was not the case.

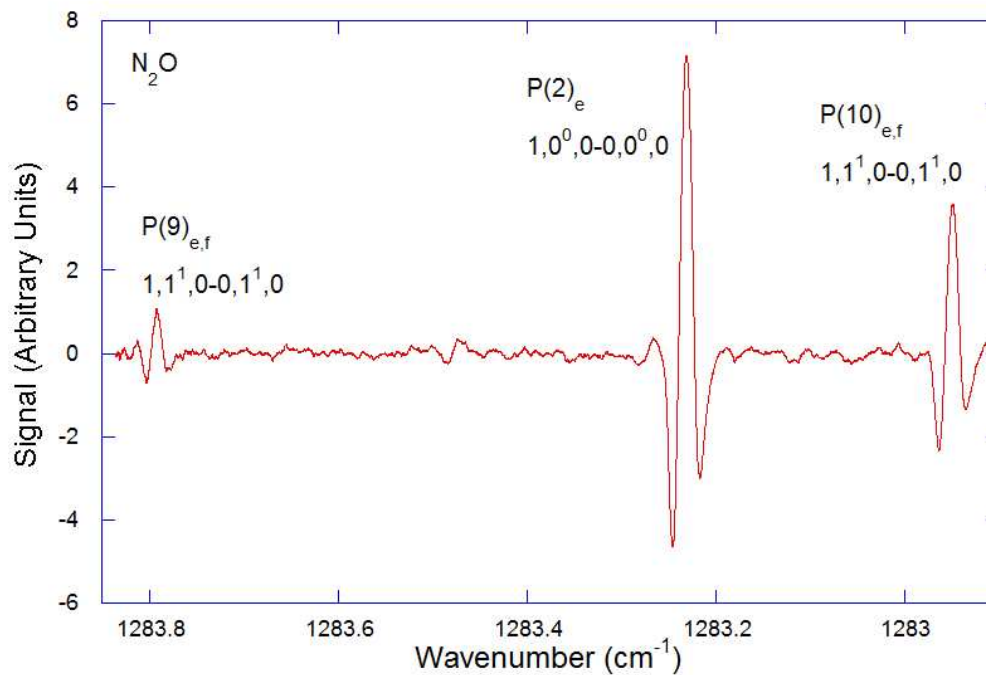


Fig. 5.13: Nitrous Oxide, 3.5Torr reading on pressure gauge, $P(2)_e$ with two unresolved doublets.

Another possibility was that it was water vapour being detected but this seemed unlikely as when water is detected it is usually seen even with the cell is empty as it is normally detectable as the laser travels around the optical table prior to entering the cell.

In figure 5.14 a sample of roof air had water vapour added and then N_2O added in an attempt to identify the lines (a) and (b). As the water vapour was added these features did appear to increase in intensity but as two other features became visible between (a) and (b) water was ruled out. Next a small amount of N_2O was added to the cell and it became instantly apparent that the unknown species was not the N_2O it was hoped to be, the only other possible species it could be was methane. Experiments with methane in the cell had been performed previously and there was a chance that some methane had been out-gassing from the cell walls.

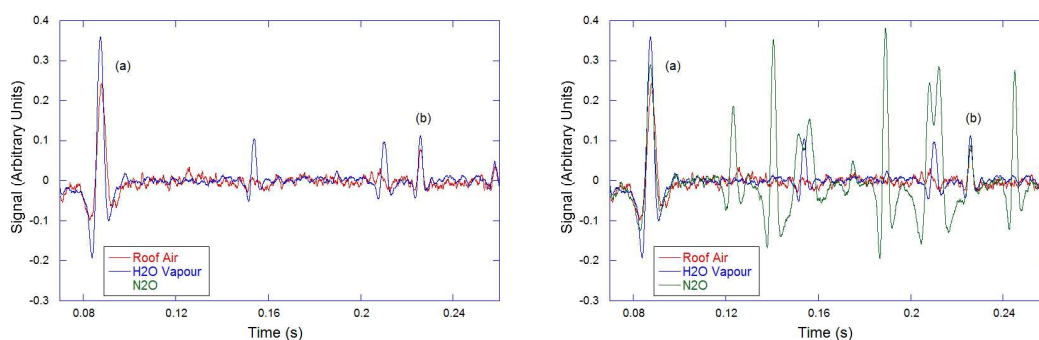


Fig. 5.14: Atmospheric air sampled from roof of John Anderson Bld, left with H₂O vapour added, right N₂O added.

To aid in clearing this air was allowed to flow through the cell for a period of time and then followed by a period of zero-air, dry nitrogen and oxygen pre-mixed to simulate air, flow through the cell and finally the cell pumped out for several hours. Etalon fringes recorded during the zero-air flowing through the cell shows the increasing laser power as the current ramp is applied, see figure 5.15.

This flushing the cell with atmosphere and then the zero-air had the desired effect of ensuring the cell was clear of any species that may cause a misidentification. After performing more tests with atmospheric samples it was determined that the laser was unable to detect N₂O occurring in the atmosphere. The region the laser scans over is near the band centre, the room temperature gas gives rise to lines with low J-values to be weaker than those mid branch. This is graphically shown by plotting the ν_1 data from the HITRAN on the web [71] resource (figure 5.16).

The gas being detected was actually Methane, the P(4)_{a1} line. The concentration of CH₄ in the atmosphere is ten times that of N₂O. Even though CH₄ also has low J-value lines in the laser scan region the greater abundance makes it easier to detect. The identification was confirmed by adding 0.5 Torr from lecture bottle of pure gas and have the line increase in intensity as well as weak lines becoming visible. When re-tuning the laser to have the CH₄ line at the end of the scan an unknown feature appeared. When the pressure flowing through the cell was increased from 50 Torr to 200 Torr the CH₄ line broadened and lost most of its definition but the other feature did not change.

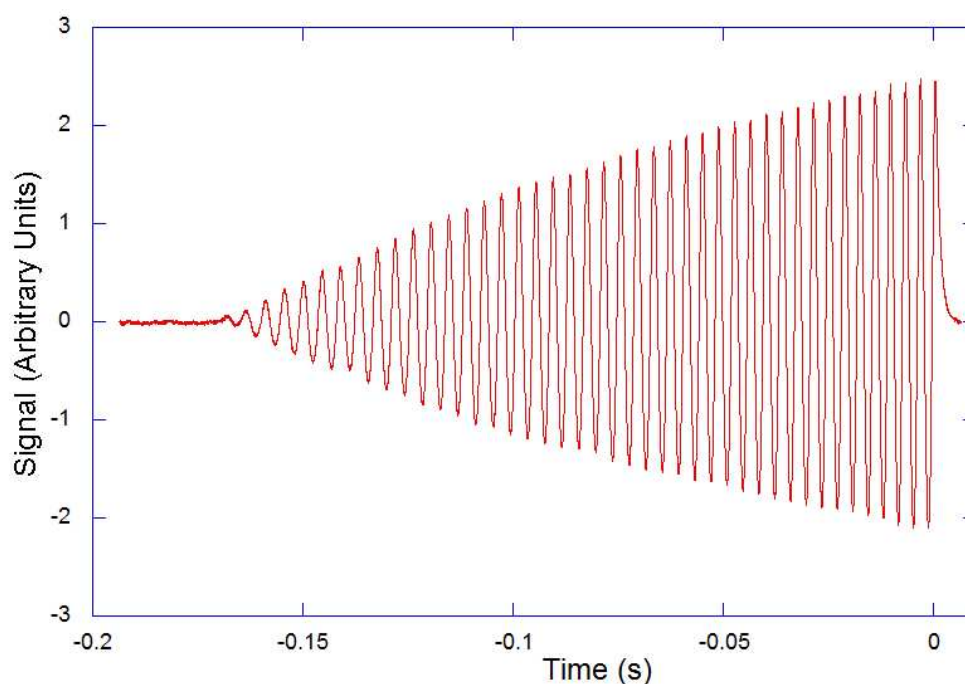


Fig. 5.15: Etalon fringe pattern as zero-air at 50 Torr flows through cell.

It was surmised that it was the laser turn-on spike that was being detected, see figure 5.17.

Although we were unable to detect N_2O in the atmosphere with the laser operating in the region available due to the inability to cool the device below the dew point of water the detection of CH_4 in atmospheric abundances reveals that there is potential for it to detect N_2O if the laser is heated to $+50^\circ\text{C}$. This would change the wavenumber scan to cover the P(5) and P(6) lines but the heat extraction would need alterations done to ensure the device does not overheat.

Cascade Technologies required the equipment returned for a short period in order to try out another laser device for a customer on return to the lab Robert noticed that the output power was not as he was expecting. The next day the device would not lase with the current source giving an error message and cutting off, on examining the connections in the head it looked as if they were not making contact properly.

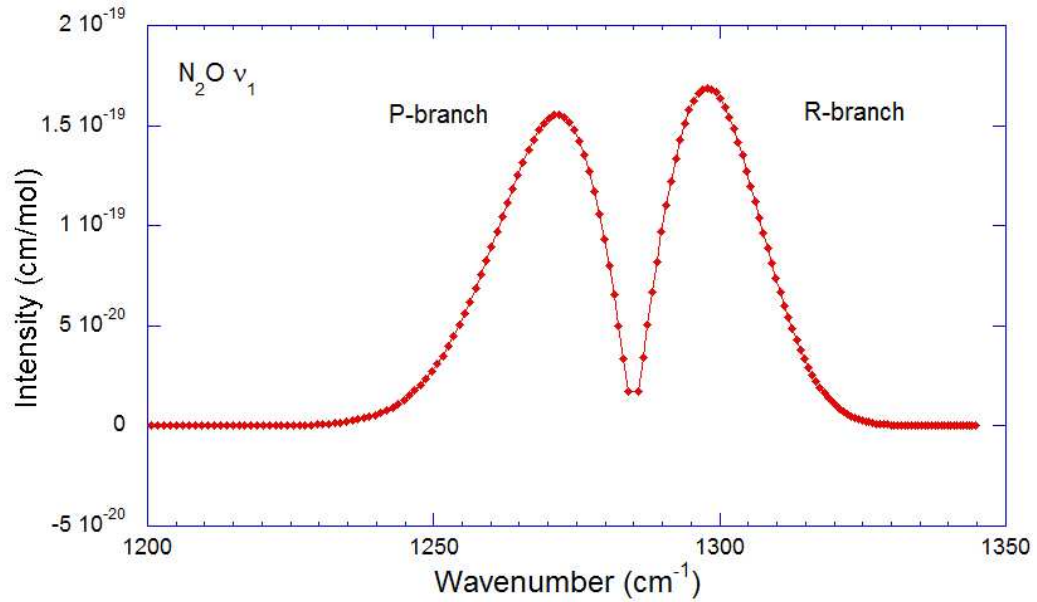


Fig. 5.16: HITRAN on the web data of ν_1 band.

Once fixed the current source no longer gave the error message but the device still would not lase. Cascade Technologies had the device tested as it was thought that the wire connections supplying electrical power to the device required re bonding, unfortunately this was not the case and the device had failed.

All figures showing signals from the oscilloscope with a negative time going to zero and then into positive is purely a consequence of the settings on the oscilloscope i.e. where the zero on the screen was positioned.

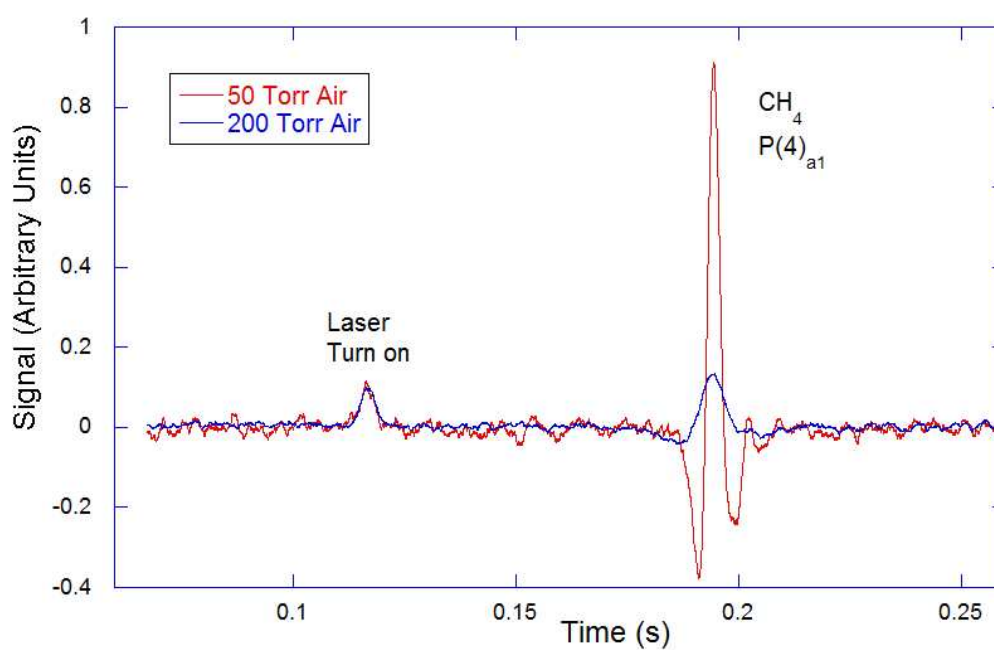


Fig. 5.17: Air flow through the cell with pressures of 50 Torr and 200 Torr.

5.4 Conclusion

The use of a DFB-CW QC laser in an absorption spectrometer shows promise as the ability to tune the laser via current modulation would require a smaller package than a cavity tuned laser. The wavelength the device operated at was slightly problematic as it was hoped to measure nitrous oxide at atmospheric abundance, a device operating at a wavelength closer to the pulsed QC laser owned by the group would be a better choice as it scans over $J=11$ to $J=13$ within the ν_1 P-branch. The use of the lock-in amplifier and slow ramp with added fast modulation in conjunction with the long path cell permitted detection of weak features.

This ability to detect weak features is clearly visible in Figure 5.17 where atmospheric concentrations of CH_4 (≈ 170 ppm) have been detected in a sample of air flowing through the Herriott Cell at a steady pressure of 50 Torr. This pressure in the cell is half the pressure currently used by the commercially available spectrometers manufactured by Cascade Technologies. With the pressure of the gas flowing through the cell it reduces the dwell time of gases within the cell. This would work in conjunction with the narrow line-width of the laser to give improved detection limits, however the slower scan rate of the laser could counteract any gain in performance the reduced pressure would give.

6. CONCLUSIONS AND FUTURE WORK

As a replacement for lead salt and CO/CO₂ lasers as a light source for mid-infrared absorption spectroscopy quantum cascade lasers have proven to be an excellent choice. They are a useful tool in the detection of trace amounts of atmospheric pollutants due to not requiring LN₂ to cool the device. This reduces the size of the spectrometers as well as requiring less maintenance. Although there is associated nonlinear effects when the laser frequency is swept rapidly it has been shown that the addition of buffer gases can reduce these effects, carbon dioxide being very efficient in damping the rapid passage signal.

As a device for measuring the combustion products of diesel powered vehicles the 4C-PQCLAS has been proven to be a feasible alternative to current machines used during MOT emission tests. The spectrometer can give accurate concentrations of via the software installed on the control laptop. Currently these are NO, N₂O, NO₂ and CO₂ with concentrations given in real time. Other gases, such as H₂O, CO and CH₄ (other hydrocarbons also absorb in the 8 μ m region and these can also be detected) can be detected with concentrations calculable through post analysis of the spectra. The software is designed to focus on a single absorption feature, so it would be possible to change the gas a specific laser gives concentration records of. However accurate calibration would be required prior to a comparison experiment against machines presently used for emission testing.

The analysis of the ¹⁵NH₃ spectra, although still in the early stages, has already identified some spectral features not previously mentioned in data available, i.e the HITRAN database. With further analysis the identification of lines in the 6.15 μ m region will increase, thus helping to increase knowledge of the isotopologue.

The dimerization of certain molecules, in this case nitrogen dioxide, can result in unreliable concentration measurements of the monomer when the dimer absorption lies in a different region to the monomer. In general infrared absorption spectrometers are fitted with lasers that have a wavelength covering the strong absorption bands. In the case of NO_2 the ν_1 band centered at 1300 cm^{-1} , with the laser used for NO_2 detection having a wavelength of either $7.46\text{ }\mu\text{m}$ or $6.15\text{ }\mu\text{m}$. The band centre of the dimer at $7.93\text{ }\mu\text{m}$ (1260 cm^{-1}) is far enough away that it is not detected by current methods.

Even with the pump-probe experiments at Oxford University not giving the results hoped for, the results from the White cell experiments (when compared to the repeated experiments at Strathclyde University) do give cause for debate. It may have been the case that the cell was causing a standing wave to form. Although the hyperfine components were not visible it looks as if the absorption by the Λ -doublets combined with the rapid frequency sweep of the laser was resulting in chirp-rate related interference between the absorption features. When the pressure of NO , within the White cell, was greater than the capacitance manometer was capable of reading weak features became visible, see figure 4.21. As they did not show any of the rapid passage effects they had the appearance of self broadened doublets. These weak doublets were also visible when the collisional experiments were repeated using the Herriott cell in the Strathclyde lab, see figure 4.32. This confirms these doublets are real but with only the strongest already identified in the HITRAN database it is likely that the middle doublet is the $^{15}\text{N}^{18}\text{O}$ isotope and the weakest to be $^{14}\text{N}^{17}\text{O}$ or a hot band transition. Confirmation of this identification would require a sample of pure $^{15}\text{N}^{18}\text{O}$.

During the initial stages of its development it has been shown that a current modulated DFB-CW QCL can be used for the detection of methane in atmospheric abundance. The method of driving the laser removed the nonlinear optical effects seen with pulsed QC lasers allowing the use of a lock-in amplifier to give a second harmonic spectra and permitted the use of an AC coupled detector.

Although other methods for gas detection and identification give greater accuracy and detection limits, for example gas chromatography and mass spectrometry, the size of these devices can limit their use. Manufacturers are now producing absorption spectrometers in packages similar in size to a briefcase. A spectrometer utilizing QCLs can also give faster response times over other methods due to the reduced purge time of the absorption cell used, most operate at a pressure of 100 Torr whereas mass spectrometers require a stronger vacuum due to the high energy electron beam used to ionize the sample.

The electron beam used for mass spectroscopy can also cause certain molecules to disassociate (or fragment). When this is likely to occur the method of Ion-Mobility Spectroscopy can be used. In this method a radioactive source is used to ionize the gas. The ionized gas is then sorted by size and shape as they pass through a 'drift gas' in an external electric field. This method is often combined with mass spectrometers or gas chromatographs. With the required radioactive source, or the more common corona discharge needed to ionize the gas, extra shielding of the electronic components make this type of spectrometer unsuitable for anything other than laboratory based experiments. When taking into consideration size and response time QCL based spectrometers are now a useful tool for molecular gas analysis both in the field and in the lab.

Future Work

The group received new pulsed lasers as part of the collaboration with Cascade Technologies, characterization of these is required prior to use. After this is done the 10 μm laser will be used with both old and new power supplies to give an indication of the effect of the smoothed current of the new supply by observing the ν_2 symmetric parallel band of ammonia. This would be a good comparison with the work done using the 6.15 μm laser.

The 10 μm laser will also be put to use in further testing of the gas flame in the lab of Dr Iain Burns to detect unburnt ethylene. Improvement to the experimental method would include the use of the retro-reflector to increase path length through the flame as well as taking reference spectra of the laboratory atmosphere to eliminate ambient species.

An opportunity to take 4C-PQCLAS onto the Facility for Airborne Atmospheric Measurements (FAAM) modified BAE 146-301 jet aircraft was indefinitely postponed after the eruption of the Icelandic Eyjafjallajökull volcano in 2010. The possibility of another chance to perform high altitude measurements has arisen with the aid of Prof. Mathew Evans at the Chemistry Department of York University. Cascade Technologies have expressed an interest in supplying a new portable spectrometer, they originally supplied the 4C-PQCLAS (a CT2400), for the measurements.

Further chances of collaboration work with Rolls Royce look likely to make measurements of combustion products from a annular combustion rig. The exhaust gases from this rig are at a pressure half of a standard jet engine exhaust.

BIBLIOGRAPHY

- [1] R.K. Pachauri and A Reisinger. *Climate Change 2007: Synthesis Report*. IPCC, 2008.
- [2] K.M. Walter, J.P. Chanton, F.S. Chapin III, E.A.G. Schuur, and S.A. Zimov. Methane production and bubble emissions from arctic lakes: Isotopic implications for source pathways and ages. *Journal of Geographical Research*, 113, 2008.
- [3] D.M. Lawrence, A.G. Slater, R.A. Tomas, M.M. Holland, and C. Deser. Accelerated arctic land warming and permafrost degradation during rapid sea ice loss. *Geophysical Research Letters*, 35, 2008.
- [4] J. Faist, F. Capasso, D.L. Sivco, C. Sirtori, A.L. Hutchinson, and A.Y. Cho. Quantum cascade laser. *Science*, 264(5158):553–556, 1994.
- [5] S. Wright, G. Duxbury, and N. Langford. A compact quantum-cascade laser based spectrometer for monitoring the concentrations of methane and nitrous oxide in the troposphere. *Applied Physics B*, 85(2-3), 2006.
- [6] K.G. Hay, S. Wright, G. Duxbury, and N. Langford. In-flight measurements of ambient methane, nitrous oxide and water using a quantum cascade laser based spectrometer. *Applied Physics B*, 90:329–337, 2008.
- [7] H.R. Barry, L. Corner, G. Hancock, R. Peverall, and G.A.D. Ritchie. Cavity-enhanced absorption spectroscopy of methane at 1.73 μm . *Chemical Physics Letters*, 333(3-4), 2001.
- [8] R. Evertsen, A. Staicu, N. Dam, A. Van Vliet, and J.J. Ter Meulen. Pulsed cavity ring-down spectroscopy of NO and NO₂ in the exhaust of a diesel engine. *Applied Physics B*, 74(4-5), 2002.

-
- [9] J. Mulrooney, C. Clifford, J. Fitzpatrick, and E. Lewis. Detection of carbon dioxide emissions from a diesel engine using a mid-infrared optical fibre based sensor. *Sensors and Actuators A*, 136, 2007.
- [10] J. Manne, O. Sukhorukov, W. Jäger, and J. Tulip. Pulsed quantum cascade laser-based cavity ring-down spectroscopy for ammonia detection in breath. *Applied Optics*, 45(36), 2006.
- [11] B.E. Brumfield, J.T. Stewart, and B.J. McCall. High-resolution spectroscopy of the ν_8 band of methyl bromide using a quantum cascade laser. *Journal of Molecular Spectroscopy*, 266, 2011.
- [12] C. Bauer, A.K. Sharma, U. Willer, J. Burgmeier, W. Braunschweig, B. amd Schade, S. Blaser, L Hvozdar, A. Müller, and G. Holl. Potentials and limits of mid-infrared laser spectroscopy for the detection of explosives. *Applied Physics B*, 92, 2008.
- [13] L. Esaki and R. Tsu. Superlattice and Negative Differential Conductivity in Semiconductors. *IBM Journal of Research and Development*, 14, 1970.
- [14] R.F. Kazarinov and R.A. Suris. Possibility of the amplification of electromagnetic waves in a semiconductor with a superlattice. *Soviet Physics Semiconductors*, 5:707–709, 1971.
- [15] J. Faist, F. Capasso, D.L. Sivco, C. Sirtori, A.L. Hutchinson, and A.Y. Cho. Quantum Cascade Laser. *Science*, 264, 1994.
- [16] H.M. Rosenberg. *The Solid State*. Oxford University Press, third edition, 2006.
- [17] A.Y. Cho and J.R. Arthur. Molecular beam epitaxy. *Progress in Solid State Chemistry*, 10, 1975.
- [18] K. Fujita, S. Furuta, A. Sugiyama, T. Ochiai, A. Ito, T. Dougakiuchi, T. Edamura, and M. Yamanishi. High-performance quantum cascade lasers with wide electroluminescence (600cm^{-1}), operating in continuous-wave above 100°C . *Applied Physics Letters*, 98, 2011.
- [19] R. Maulini, A. Lyakh, A. Tsekoun, R. Go, and C.K.N. Patel. High average power uncooled mid-wave infrared quantum cascade lasers. *Electronics Letters*, 47, 2011.

-
- [20] K. Namjou, S. Cai, E.A. Whittaker, J. Faist, C. Gmachl, F. Capasso, D.L. Sivco, and A.Y. Cho. Sensitive absorption spectroscopy with a room-temperature distributed-feedback quantum-cascade laser. *Opt.Lett.*, 23(3), 1998.
- [21] A.A. Kosterev, F.K. Tittel, C. Gmachl, D.S. Capasso, F. Sivco, A.L. Baillargeon, J.N. Hutchinson, and A.Y. Cho. Trace-gas detection in ambient air with a thermoelectrically cooled, pulsed quantum-cascade distributed feedback laser. *Applied Optics*, 39, 2000.
- [22] E. Normand, M.T. McCulloch, G. Duxbury, and N. Langford. Fast, real-time spectrometer based on a pulsed quantum-cascade laser. *Optics Letters*, 28(1), 2003.
- [23] M.T. McCulloch, E. Normand, N. Langford, and G. Duxbury. Highly sensitive detection of trace gases using the time-resolved frequency downchirp from quantum cascade lasers. *Journal of the Optical Society of America B*, 20(8), 2003.
- [24] R. Bracewell. *The Fourier Transform and Its Applications*. McGraw Hill, New York, 1965.
- [25] B. Grouiez, B. Parvitte, L. Joly, and V. Zeninari. Alternative method for gas detection using pulsed quantum-cascade-laser spectrometers. *Optics Letters*, 34, 2009.
- [26] G. Duxbury, N. Langford, M.T. McCulloch, and S. Wright. Rapid passage induced population transfer and coherences in the 8 micron spectrum of nitrous oxide. *Molecular Physics*, 105, 2007.
- [27] A. Cheesman, J.A. Smith, M.N.R. Ashfold, N. Langford, S. Wright, and G. Duxbury. Application of a Quantum Cascade Laser for Time-Resolved, in Situ Probing of CH₄/H₂ and C₂H₂/H₂ Gas Mixtures during Microwave Plasma Enhanced Chemical Vapor Deposition of Diamond. *Journal of Physical Chemistry A*, 110, 2006.
- [28] G. Duxbury, N. Langford, and K.G. Hay. Delayed rapid passage and transient gain signals generated using a chirped 8 μ m quantum cascade laser. *Journal of Modern Optics*, 55, 2008.

-
- [29] K.G. Hay. *Gas Sensing Using Quantum Cascade Lasers*. PhD thesis, University of Strathclyde, 2010.
- [30] D.R. Herriott and H.J. Schulte. Folded optical delay lines. *Applied Optics*, 4(8), 1965.
- [31] M.T. McCulloch. *Quantum Cascade Laser based Absorption Spectrometer for Trace Gas Molecular Detection and Nonlinear Optics*. PhD thesis, University of Strathclyde, 2005.
- [32] J.U. White. Long Optical Paths of Large Aperture. *Journal of the Optical Society of America*, 32, 1942.
- [33] Vigo Systems. Vigo Systems, PVI-2TE series. http://www.vigo.com.pl/index.php/en/english_menu/products/ir_detectors_comparison_table/lista_aktualna/pvi_2te_series, 2012.
- [34] J. Ma, A. Cheesman, M. Ashford, K. Hay, S. Wright, N. Langford, G. Duxbury, and Y. Mankelevich. Quantum cascade laser investigation of CH₄ and C₂H₂ interconversion in hydrocarbonH₂ gas mixtures during microwave plasma enhanced chemical vapor deposition of diamond. *J. Appl. Phys.*, 106, 2009.
- [35] G Duxbury, K.G. Hay, M.P. Langford, N. Joinson, and J.D. Black. Real-time diagnostic of a jet engine exhaust using an intra-pulse quantum cascade laser spectrometer. *Molecular Physics*, 109, 2011.
- [36] H.J. Bernstein and G. Herzberg. RotationVibration Spectra of Diatomic and Simple Polyatomic Molecules with Long Absorption Paths. 1, The Spectrum of Fluoroform(CHF₃) from 2.4 μ m to 0.7 μ m. *Journal of Chemical Physics*, 16, 1948.
- [37] J.T. Hougen. The Calculation of Rotational Energy Levels and Rotational Line Intensities in Diatomic Molecules. NBS monograph 115, National Bureau of Standards, Washington. DC, 1970.
- [38] G. Duxbury. *Infrared Vibration-Rotation Spectroscopy: From Free Radicals to the Infrared Sky*. John Wiley and Sons, Chichester, 2000.
- [39] M.J. Hollas. *Modern Spectroscopy*. John Wiley & Sons, fourth edition, 2004.

-
- [40] G. Herzberg. *Infrared and Raman Spectra of Polyatomic Molecules*. D. Van Nostrand Company, Inc, New York, 1945.
- [41] P.M. Morse. Diatomic Molecules According to the Wave Mechanics. II. Vibrational Levels. *Physical Review*, 34, 1929.
- [42] G. Duxbury, N. Langford, M.T. McCulloch, and S Wright. Rapid passage induced population transfer and coherences in the 8 micron spectrum of nitrous oxide. *Molecular physics*, 105, 2007.
- [43] E.E. Whiting. An empirical approximation to the Voigt profile. *Journal of Quantitative Spectroscopy and Radiative Transfer*, 8, 1968.
- [44] J.J. Olivero and R.L. Longbothum. Empirical fits to the Voigt line width: A brief review. *Journal of Quantitative Spectroscopy and Radiative Transfer*, 17, 1977.
- [45] R.R. Ernst. Sensitivity enhancement in magnetic resonance. In *Advances in Magnetic Resonance*, volume 2, pages 1–135. Academic Press, 1966.
- [46] A. Abragam. *The Principles of Nuclear Magnetism*. Oxford University Press, Oxford, 1961, 1983.
- [47] M.M. Loy. Observation of population inversion by optical adiabatic rapid passage. *Phys. Rev. Lett.*, 32(15):814–817, 1974.
- [48] K. Totoda, Y. Takahashi, K. Ishikawa, and T. Yabuzaki. Optical free-induction decay of laser-cooled ^{85}Rb . *Physical Review A*, 56, 1997.
- [49] P. Dubé, M.D. Levenson, and J.L. Hall. Free-induction decay in molecular iodine measured with an external-cavity diode laser. *Optics Letters*, 22, 1997.
- [50] R.M. MacFarlane and M. Zhu. Observation of coherent transients by use of current switching of a semiconductor diode laser. *Optics Letters*, 22, 1997.
- [51] F. Bloch. Nuclear Induction. *Physical Review*, 70, 1946.

-
- [52] R.L. Shoemaker. Coherent Transient Infrared Spectroscopy. In J.I. Steinfeld, editor, *Laser and Coherence Spectroscopy*. Plenum, New York, 1978.
- [53] G. Duxbury, J.F. Kelly, T.A. Blake, and N. Langford. Observation of infrared free-induction decay and optical nutation signals from nitrous oxide using a current modulated quantum cascade laser. *Journal of Chemical Physics*, 136, 2012.
- [54] G. Duxbury, J.F. Kelly, T.A. Blake, and N. Langford. The AC Stark effect in nitric oxide induced by rapidly swept continuous wave quantum cascade lasers. *Journal of Chemical Physics*, 136, 2012.
- [55] G. Duxbury, J.F. Kelly, T.A. Blake, and N. Langford. Sub-Doppler spectra of infrared hyperfine transitions of nitric oxide using a pulse modulated quantum cascade laser: Rapid passage, free induction decay, and the AC Stark effect. *Journal of Chemical Physics*, 136, 2012.
- [56] I.I. Rabi. On the Process of Space Quantization. *Physical Review*, 49, 1936.
- [57] H.M. Pickett. The Fitting and Prediction of Vibrational-Rotational Spectra with Spin Interactions. *Journal of Molecular Spectroscopy*, 148:371–377, 1991.
- [58] H. Pickett. <http://spec.jpl.nasa.gov/ftp/pub/calpgm/>.
- [59] M. Hepp, R. Georges, M. Herman, J.-M. Flaud, and W.J. Lafferty. Striking anharmonic resonances in N₂O₄: supersonic jet fourier transform spectra at 13.3, 7.9, 5.7 and 3.2 μm . *Journal of Molecular Structure*, 517-518:171–180, 2000.
- [60] Z. Kisiel. <http://www.ifpan.edu.pl/kisiel/asym/pickett/crib.htm#spcat>, 2010.
- [61] M.T. McCulloch, N. Langford, and G. Duxbury. Real-time trace level detection of carbon dioxide and ethylene in car exhaust gases. *Applied Optics*, 44, 2005.
- [62] Glasgow City Council. It's time for a breather. www.glasgow.gov.uk/en/Residents/Environment/Pollution/Air/Itstimetocleartheair.htm, 2011.

-
- [63] R.S.M. Chrystie, I.S. Burns, J. Hult, and C.F. Kaminski. High-repetition-rate combustion thermometry with two line atomic fluorescence excited by diode lasers. *Optics Letters*, 34, 2009.
- [64] I.S. Burns, N. Lamourreux, C.F. Kaminski, J. Hult, and P. Desgroux. Diode laser atomic fluorescence temperature measurements in low-pressure flames. *Applied Physics B-Lasers and Optics*, 93, 2008.
- [65] L.S. Rothman *et al.* The HITRAN 2004 molecular spectroscopic database. *Journal of Quantitative Spectroscopy and Radiative Transfer*, 96, 2005.
- [66] J. Ma, A. Cheesman, M.N.R. Ashford, K.G. Hay, S. Wright, N. Langford, G. Duxbury, and Y.A. Mankelevich. Quantum cascade laser investigations of CH₄ and C₂H₂ interconversion in hydrocarbon/H₂ gas mixtures during microwave plasma enhanced chemical vapour deposition of diamond. *Journal of Applied Physics*, 106, 2009.
- [67] P.M. Chu, F.R. Guenther, G.C. Rhoderick, and W.J. Lafferty. NIST Chemistry Webbook. webbook.nist.gov/chemistry/, 2011.
- [68] L.S. Rothman *et al.* HITEMP the high-temperature molecular spectroscopic database. *Journal of Quantitative Spectroscopy and Radiative Transfer*, 111, 2010.
- [69] Y. Kabbadj, M. Herman, G. Di Lonardo, L. Fusina, and J.W.C. Johns. The bending energy levels of C₂H₂. *Journal of Molecular Spectroscopy*, 150, 1991.
- [70] M. Herman, T.R. Huet, Y. Kabbadj, and J. Vander Auwera. l-type resonances in C₂H₂. *Molecular Physics*, 72(1), 1991.
- [71] L. Rothman and S. Tashkun. HITRAN on the web. <http://hitran.iao.ru/>, 2011.
- [72] G. Hancock, G. Ritchie, R. Walker, and D. Weidmann. Application of midinfrared quantum cascade laser to spectroscopy. *Optical Engineering*, 49, 2010.
- [73] G. Herzberg. l-type Doubling of Linear Polyatomic Molecules. *Reviews of Modern Physics*, 14, 1942.

-
- [74] I.I. Zasavitskii, M.A. Kerimkulov, A.I. Nadezhdinskii, V.N. Ochkin, S.Yu. Savinov, M.V. Spisdonov, and A.P. Shotov. Coherent nonstationary effects during rapid recording of an absorption spectrum. *Optics and Spectroscopy.(USSR)*, 65, 1988.
- [75] G. Duxbury, N. Langford, M.T. McCulloch, and S. Wright. Quantum cascade semiconductor infrared and far-infrared lasers: from trace gas detection to non-linear optics. *Chem.Soc.Rev.*, 34:921–934, 2005.
- [76] A.G. Maki and J.S. Wells. NIST Wavenumber Calibration Tables. <http://www.nist.gov/pml/data/wavenum/spectra.cfm>, 2010.
- [77] N. Bloembergen, E.M. Purcell, and R.V. Pound. Relaxation Effects in Nuclear Magnetic Resonance Absorption. *Physical Review*, 73, 1948.
- [78] E.L. Hahn. Nuclear Induction Due to Free Larmor Precession. *Physical Review*, 77, 1950.
- [79] G. Duxbury, N. Langford, and K. Hay. Delayed rapid passage and transient gain signals generated using a chirped $8\mu\text{m}$ quantum cascade laser. *Journal of Modern Optics*, 55, 2008.
- [80] A. Goldman and R. D. Blatherwick. On the variation of infrared absorption spectra with gas pressure and cell length. *Journal of Chemical Education*, 57(5):392, 1980.
- [81] G. Hancock, J.P. Van Helden, G.A.D Ritchie, and R.J Walker. Direct and wavelength modulation spectroscopy using a cw external cavity quantum cascade laser. *Applied Physics Letters*, 94, 2009.
- [82] N. Tasinato, K.G. Hay, N. Langford, G. Duxbury, and D. Wilson. Time dependant measurements of nitrous oxide and carbon dioxide collisional relaxation processes by a frequency down-chirped quantum cascade laser: Rapid passage signals and the time dependence of collisional processes. *J.Chem.Phys.*, 132(1), 2010.
- [83] R.A. Toth. Line positions and strengths of CO_2 in the $1200\text{-}1430\text{ cm}^{-1}$ region. *Applied Optics*, 24, 1985.
- [84] H. Lefebvre Brion and R.W. Field. *Perturbations in the Spectra of Diatomic Molecules*. Academic Press, Inc, 1986.

-
- [85] G.C. Toon, C.B. Farmer, and R.H. Norton. Detection of stratospheric N_2O_5 by infrared remote sounding. *Nature*, 319:570–571, 1986.
- [86] April D. Hennis, C. Scott Highnerger, and Serge Schreiner. Formation and Dimerization of NO_2 A General Chemistry Experiment. *Journal of Chemical Education*, 74:1340, 1997.
- [87] H. A. Bent. Dimers of Nitrogen Dioxide. II. Structure and Bonding. *Inorganic Chemistry*, 2:747–752, 1963.
- [88] F. Mélen, F. Pokorni, and M. Herman. Vibrational band analysis of N_2O_4 . *Chemical Physics Letters*, 194, 1992.
- [89] D. Hurtmans, M. Herman, and J. Vander Auwere. Integrated band intensities in N_2O_4 in the infrared range. *Journal of Quantitative Spectroscopy and Radiative Transfer*, 50, 1993.
- [90] D. Luckhaus and M. Quack. High-resolution FTIR spectra of NO_2 and N_2O_4 in supersonic jet expansions and their rovibrational analysis. *Chemical Physics Letters*, 199, 1992.
- [91] A. Kovács, K.B. Borisenko, and G. Pongor. An application of the DFT-based scaled quantum mechanical force field method to a weakly bonded system: N_2O_4 . *Chemical Physics Letters*, 280, 1997.
- [92] Y. Elyoussoufi, M. Herman, J. Liévin, and I. Kleiner. Ab initio and experimental investigation of the vibrational energy pattern in N_2O_4 : the mid and near infrared ranges. *Spectrochimica Acta Part A*, 53, 1997.
- [93] C. Dyer and P.J. Hendra. Raman spectroscopy of $\text{NO}_2/\text{N}_2\text{O}_4$ in the gas phase using near-infrared excitation. *Chemical Physics Letters*, 233:461–465, 1995.
- [94] R. Georges, M. Bach, and M. Herman. High resolution FTIR spectroscopy using a slit jet: sampling the overtone spectrum of $^{12}\text{C}_2\text{H}_4$. *Molecular Physics*, 90:381–388, 1997.
- [95] A.J. Vosper. Dissociation of Dinitrogen Tetroxide in the Gas Phase. *Journal of the Chemical Society A*, A325, 1970.

-
- [96] W.F. Giauque and J.D. Kemp. The Entropies of Nitrogen Tetroxide and Nitrogen Dioxide. The Heat Capacity from 15K to the Boiling Point. The Heat of Vaporization and Vapor Pressure. The Equilibria $\text{N}_2\text{O}_4=2\text{NO}_2=2\text{NO}+\text{O}_2$. *Journal of Chemical Physics*, 6, 1938.
- [97] G. Duxbury, N. Langford, K. Hay, and N. Tasinato. Quantum cascade laser spectroscopy: diagnostics to non-linear optics. *Journal of Modern Optics*, 56, 2009.
- [98] M. Šimečková, D. Jacquemart, L.S. Rothman, R.R. Gamache, and A. Goldman. Einstein A-coefficients and statistical weights for molecular absorption transitions in the *hitran* database. *Journal of Quantitative Spectroscopy & Radiative Transfer*, 98, 2006.
- [99] G. Di Lonardo, L Fusina, and A. Trombetti. The ν_2 , $2\nu_2$, $3\nu_2$, ν_4 , and $\nu_2 + \nu_4$ Bands on $^{15}\text{NH}_3$. *Journal of Molecular Spectroscopy*, 92, 1982.
- [100] C. Cottaz, I. Kleiner, G. Tarrago, L.R. Brown, J.S. Margolis, R.L. Poynter, H.M. Pickett, T. Fouchet, P. Drossart, and E. Lellouch. Line Positions and Intensities in the $2\nu_2/\nu_4$ Vibrational System of $^{14}\text{NH}_3$ near 5-7 μm . *Journal of Molecular Spectroscopy*, 203, 2000.
- [101] V. De Preter and K. Verbeke. Evaluation of the necessity of induction for lactose-[N-15, N-15]- ureide to study the colonic ammonia metabolism. *Scandinavian Journal of Gastroenterology*, 41, 2006.
- [102] W.M. Litchman, M. Alei, and A.E. Florin. ^{15}N NMR Chemical Shifts in $^{15}\text{ND}_3$, $^{15}\text{ND}_2\text{H}$, $^{15}\text{NDH}_2$, and $^{15}\text{NH}_3$. *Journal of Chemical Physics*, 50, 1969.
- [103] V.L Kasyutich, R.K.R. Ibrahim, and P.A. Martin. Stability of widely tunable, continuous wave external cavity quantum cascade laser for absorption spectroscopy. *Infrared Physics and Technology*, 53, 2010.
- [104] T. Maier, H. Schneider, H.C. Liu, M. Walther, and P. Koidl. Two photon QWIPs for quadratic detection of weak mid-infrared laser pulses. *Infrared Physics and Technology*, 47, 2005.